# Harvesting Insights from Advanced Microscope Acquisitions: Techniques and Applications

Thesis by
Mingshu Liang

In Partial Fulfillment of the Requirements for the
degree of
Doctor of Philosophy


CALIFORNIA INSTITUTE OF TECHNOLOGY
Pasadena, California

2025
Defended October 18, 2024

Mingshu Liang
ORCID: 0000-0001-7748-7652

# ACKNOWLEDGEMENTS

As I complete this phase of my academic journey, I'm thankful for all the people who've had my back and pointed me in the right direction during my PhD. This thesis wouldn't have come together without their steady support, patience, and expertise.

First and foremost, I would like to express my sincere gratitude to my advisor, Prof. Changhuei Yang. Under his guidance, I learned to become a researcher by making informed decisions, conducting rigorous experiments, and critically evaluating every aspect of my work. His high standards for research and manuscript quality have consistently motivated me to think more deeply and strive for excellence. I appreciate his openness to discussion and willingness to help in solving problems, both academic and non-academic, which provided support throughout my PhD journey. It is through his mentorship that I have gained profound insights into the nature of research and the academic world.

I would also like to express my gratitude to my committee members, Prof. Lihong Wang, Prof. Katherine (Katie) L. Bouman, and Prof. Alireza Marandi, for their valuable insights on my research and their support during my defense. I am also thankful for the knowledge they imparted through their courses. Prof. Bouman's course deepened my understanding of computational cameras, while Prof. Wang's course enhanced my grasp of light scattering in biological tissue, both of which greatly contributed to my research.

I would also like to express my appreciation to my lab members for fostering such a warm and light lab atmosphere. I want to thank Dr. Jian Xu for familiarizing me with everything about the lab in the beginning, teaching me experimental skills, and continuing to offer support even after his graduation. I am also grateful to Dr. Cheng Shen for his insightful discussions and research guidance during my initial stages. My thanks extend to the rest of the lab members—Dr. Baptiste Blochet, Dr. Michelle Cua, Dr. Ruizhi Cao, Dr. Oumeng Zhang, Dr. Simon Mahler, Haowen Zhou, Max (Yu Xi) Huang, Siyuan Yin, Steven (Siyu) Lin, Zhenyu Dong, Josh (Shi) Zhao, and Ninghe (Neo) Liu—for their helpful conversations. I especially appreciate all the fun we've had during lunch chats, parties, cake celebrations, Rubik's cube races, table tennis games, and other memorable lab activities. I would like to thank my collaborators: Prof. Cory Bernadt, Prof. Richard Cote, Dr. Maciej Meglicki, Dr. Sergi Junyent Espinosa, Dr. Estefania Sanchez Vasquez, Dr. Adiyant Lamba,

Dr. Benjamin Laccetti, Dr. Monica Goss, and Dr. Shawn Cao for actively providing samples, engaging in project discussions, and collaboratively preparing manuscripts with me. Without their support, I would not be graduating today.

Many thanks to all my friends outside the Biophotonics Lab who supported me and brought joy to my PhD journey: Yibing Wei, Lin Ma, Jinrui Hou, Zhiling Zhou, Yang Liu, Yushu Pan, Ziyun Zhang, Siming Sun, Shuyun Yuan, Yueyang Pan, Ruifang Guan, Zhijia Guo, Jingna Sun, Hongming Lin, Jiahui Hou, Youtian Wang, and Xintong Cai.

I would like to thank my family members for their unconditional support. I want to especially thank my dad for his love for our family and for me, even during difficult times. He communicates with me openly, always providing support and reassurance. His presence brings me peace when facing challenges, and he gives me the courage to pursue my goals, knowing he will always be by my side.

Completing my PhD journey has not been easy; it has involved challenges, difficulties, triumphs, and happiness. I am grateful for all the experiences, lessons, and relationships I've gained along the way. While this thesis marks the end of my doctoral studies, the memories I've created will continue to thrive, becoming one of the most unforgettable periods of my life.

# ABSTRACT

Since their inception, microscopes have evolved significantly, becoming essential tools across various fields, from pathology diagnosis to biological studies. Morphological information that cannot be otherwise observed has always been regarded as the primary data a microscope could deliver. Yet microscopy data embodies further valuable information worth exploring. This thesis demonstrates extracting three types of information beyond morphology by modifying microscope systems, incorporating physical models, and applying image processing: 1) depth information, 2) object size information, and 3) object developmental information.

The first part of the thesis describes an all-in-focus technique based on Fourier Ptychographic Microscopy (FPM) for depth information extraction. It synthesizes an all-in-focus image and depth map from an FPM-reconstructed multi-focal image stack. This technique benefits thyroid fine needle aspiration samples, relieving pathologists from the need to constantly adjust focal planes, enabling convenient data transfer, and potentially aiding machine learning tasks on cytology specimens.

The second part of the thesis focuses on a non-destructive subvisible particle (SbVPs) analyzer for estimating size and concentrations of SbVPs in drug products. This analyzer aims to estimate the size and concentrations of SbVPs within a drug product while keeping the sample intact. Incorporating a light-sheet microscope with custom housings to compensate for container-induced astigmatism, it uses side-scattered light as a size indicator based on Mie scattering theory. Its functionality is demonstrated on polystyrene beads and biological drug products. Additionally, a new metric named the strip density is discovered from the same microscope images, which could serve as a more precise and robust size indicator beyond scattering light intensity. This new size indicator is used to train a particle detection neural network, verifying its effectiveness through good performance.

For the final part, we focus on an embryo sex classification project, aiming to extract subtle developmental differences between male and female embryos from early development videos taken by Embryoscope. A combined convolutional and recurrent neural network structure is employed. While the prediction accuracy reaches 61%, which is not high, the deep learning model outperforms both human and random predictions, demonstrating its ability to acquire embryo developmental information from the Embryoscope videos to some extent.

# PUBLISHED CONTENT AND CONTRIBUTIONS

[1] Mingshu Liang et al. “Non-Destructive analysis of subvisible particles with Mie-scattering-based light sheet technology: System development.” In: *Journal of Pharmaceutical Sciences* 113.9 (2024), pp. 2817–2825.
M.L. conceived the project idea, conducted the experiments, developed the algorithms, and wrote the manuscript.

[2] Siyuan Yin et al. “Can deep neural networks work with amplitude and phase input of defocused images?” In: *Optics Express* 32.14 (2024), pp. 25036–25045.
M.L. contributed to the discussion of ideas, assisted in designing the experiment, and participated in improving the manuscript.

[3] Haowen Zhou et al. “Fourier ptychographic microscopy image stack reconstruction using implicit neural representations.” In: *Optica* 10.12 (2023), pp. 1679–1687.
M.L. prepared part of the data and participated in improving the manuscript.

[4] Simon Mahler et al. “Assessing depth sensitivity in laser interferometry speckle visibility spectroscopy (iSVS) through source-to-detector distance variation and cerebral blood flow monitoring in humans and rabbits.” In: *Biomedical Optics Express* 14.9 (2023), pp. 4964–4978.
M.L. participated in discussions and assisted with manuscript improvements.

[5] Haowen Zhou et al. “Analysis of postreconstruction digital refocusing in Fourier ptychographic microscopy.” In: *Optical Engineering* 61.7 (2022), pp. 073102–073102.
M.L. contributed to the discussion of ideas, assisted in designing the experiment, and participated in improving the manuscript.

[6] Mingshu Liang and Changhuei Yang. “Implementation of free-space Fourier Ptychography with near maximum system numerical aperture.” In: *Optics Express* 30.12 (2022), pp. 20321–20332.
M.L. conceived the project idea, conducted the experiments, developed the algorithms, and wrote the manuscript.

[7] Mingshu Liang et al. “All-in-focus fine needle aspiration biopsy imaging based on Fourier ptychographic microscopy.” In: *Journal of Pathology Informatics* 13 (2022), p. 100119.
M.L. conceived the project idea, conducted the experiments, developed the algorithms, and wrote the manuscript.

[8] Cheng Shen et al. “Non-iterative complex wave-field reconstruction based on Kramers–Kronig relations”. In: *Photonics Research* 9.6 (2021), pp. 1003–1012.
M.L. participated in discussions and assisted with manuscript improvements.

# TABLE OF CONTENTS

# LIST OF ILLUSTRATIONS

# LIST OF TABLES

*Chapter 1*

# INTRODUCTION

Modern optical microscopes have opened a brand-new miniature world for biology and medicine. Since their appearance in the 17th century, they have allowed scientists to discover micro-organs and, for the first time, define the basic unit that makes up living organisms: the "cell." Optical microscopes have continued to evolve, enabling countless discoveries along the way. Phase contrast microscopy and differential interference contrast microscopy have made transparent samples visible, fluorescent microscopy has enabled imaging of specific components such as cell substructures and proteins, and super-resolution microscopy has broken the diffraction resolution limit, enabling single-molecule imaging.

Morphological information has always been the primary data extracted from microscope acquisitions. For instance, such information provides clues for pathologists to make diagnoses and offers insights that lead to novel biological discoveries. However, additional information beyond morphology can also be extracted from microscope acquisitions by modifying microscope structures and through post-data processing. This additional information can further enhance acquired images, broaden the application scope of microscopy, and bring new insights to biological research.

This chapter introduces the basic concepts essential to microscope systems and the downstream information extraction discussed in subsequent chapters. It covers the physics of light itself, Fourier interpretation of optical systems, image formation, typical microscope structures, scattering, and basic machine learning concepts. With these concepts established, three examples of extracting additional information from microscope acquisitions will be discussed in the following chapters.

## 1.1 Maxwell's equations

Maxwell's equations [1] describe the wave-like electric and magnetic fields of light. This set of equations consists of four electromagnetism laws: Gauss's law, Gauss's law for magnetism, Faraday's law, and Ampere's law. The partial differential form of the Maxwell equations can be written as:

$$\begin{aligned} \nabla \cdot E &= \frac{\rho}{\epsilon_0} \\ \nabla \cdot B &= 0 \\ \nabla \times E &= -\frac{\partial B}{\partial t} \\ \nabla \times B &= \mu_0 (J + \epsilon_0 \frac{\partial E}{\partial t}) \end{aligned} \tag{1.1}$$

where $E$ is the electric field, $B$ is the magnetic field, $\rho$ is the charge density, $J$ is the current density, $\epsilon_0$ is the vacuum permittivity, and $\mu_0$ is the vacuum permeability.

Under free space conditions, both charge density and current density are zero:

$$\begin{aligned} \rho &= 0 \\ J &= 0. \end{aligned} \tag{1.2}$$

To find the solutions for Maxwell's equations, we first make use of the curl of curl property, which is written as:

$$\nabla \times (\nabla \times E) = \nabla(\nabla \cdot E) - \nabla^2 E. \tag{1.3}$$

Then the Faraday's law can be written as:

$$\nabla^2 E = \frac{n^2}{c^2} \frac{\partial^2 E}{\partial t^2} \tag{1.4}$$

where n is the refractive index (RI) of the medium:

$$n = \sqrt{\frac{\epsilon}{\epsilon_0}} \tag{1.5}$$

and $c$ is the speed of light in vacuum:

$$c = \frac{1}{\sqrt{\mu_0 \epsilon_0}}. \tag{1.6}$$

Similarly, the magnetic field satisfies the same equation. Without loss of generality, the electric field is discussed in the following chapters and sections. It is possible to summarize the behavior of the components of $E$ and $H$ by a single scalar wave equation:

$$\nabla^2 u(\mathbf{r}, t) = \frac{n^2}{c^2} \frac{\partial^2 u(\mathbf{r}, t)}{\partial t^2} \tag{1.7}$$

here $u(\mathbf{r}, t)$ represents any scalar field components with dependence on spatial position $\mathbf{r}$ and time $t$.

For a monochromatic wave, the scalar could be written as:

$$u(\mathbf{r}, t) = A(\mathbf{r}) \exp(i\omega t). \tag{1.8}$$

Plugging eq.1.8 into the scalar wave equation eq.1.7, the Helmholtz equation can be obtained:

$$(\nabla^2 + k^2)A(\mathbf{r}) = 0 \tag{1.9}$$

where $k$ is the wave number, expressed as:

$$k = \omega \frac{n}{c} = \frac{2\pi}{\lambda}. \tag{1.10}$$

Solving the Helmholtz equation, the plane wave solution can be obtained:

$$E(\mathbf{r}, t) = E_0 \exp\left(i(\omega t - \mathbf{k} \cdot \mathbf{r})\right) \tag{1.11}$$

where $\mathbf{k}$ is the wave factor whose modulus $|\mathbf{k}|$ equals the wave number $k$.

## 1.2 Two-dimensional Fourier transform

The Fourier transform [1] of a function $g$ of two independent variables $x$ and $y$ is defined by:

$$\mathcal{F}\{g\} = \iint_{-\infty}^{\infty} g(x, y) \exp[-i2\pi(f_X x + f_Y y)]\, dx\, dy. \tag{1.12}$$

Similarlay, the inverse Fourier transform of a fuinction $G(F_X, F_Y)$ is defiened by:

$$\mathcal{F}^{-1}\{G\} = \iint_{-\infty}^{\infty} G(f_X, f_Y) \exp[i2\pi(f_X x + f_Y y)]\, df_X\, df_Y. \tag{1.13}$$

The two-dimension Fourier can be interpreted as a decomposition of the function $g$ into a linear combination of elementary functions with the format of $exp[i2\pi(f_X x + f_Y y)]$, indicating such elementary functions are with spatial frequency of $(f_X, f_Y)$.

## 1.3 Light propagation

The Huygens-Fresnel principle [1] provides a model to describe and predict the propagation of light. The principle states that every point on a wavefront serves as a point source and emanates secondary wavelets. The sum of these secondary wavelets forms a new wavefront. A wave propagation scheme is illustrated in Fig.1.1.

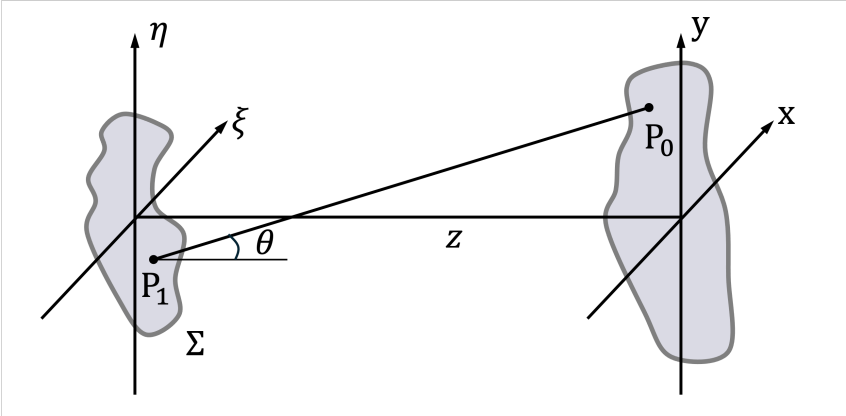


Figure 1.1: Wave propagation geometry.

Given the propagation scenario of Fig.1.1, the Huygens-Fresnel principle can be written as:

$$U(x,y) = \frac{z}{i\lambda}\iint_{\Sigma} U(\xi,\eta)\frac{\exp(ikr_{01})}{r_{01}}\,d\xi\,d\eta \tag{1.14}$$

where $r_{01}$ is the distance between $P_0$ and $P_1$ defined as:

$$r_{01} = \sqrt{z^2 + (x-\xi)^2 + (y-\eta)^2}. \tag{1.15}$$

Applying the Fresnel approximation to eq.1.15, we have:

$$r_{01} \approx z[1 + \frac{1}{2}(\frac{x-\xi}{z})^2 + (\frac{y-\eta}{z})^2]. \tag{1.16}$$

The resulting expression of the wave propagation then becomes:

$$U(x,y) = \frac{e^{ikz}}{i\lambda z}\iint_{-\infty}^{\infty} U(\xi,\eta)\exp\{i\frac{k}{2z}[(x-\xi)^2 + (y-\eta)^2]\}d\xi\,d\eta. \tag{1.17}$$

The Fresnel propagation expression eq.1.17 can be interpreted as the field $U(\xi,\eta)$ convolved with a kernel with the form of:

$$h(x,y) = \frac{e^{ikz}}{i\lambda z}\exp[\frac{ik}{2z}(x^2+y^2)]. \tag{1.18}$$

Applying Fourier transform to both side of eq.1.17 together with the convolution theorem, we have the Fourier expression of the Fresnel propagation equation:

$$\mathcal{F}\{U(x,y)\} = \mathcal{F}\{U(\xi,\eta)\}\cdot H(f_X, f_Y) \tag{1.19}$$

where the Fourier transform of the Fresnel kernel is written as:

$$\begin{aligned} H(f_X, f_Y) &= \mathcal{F}\{\frac{e^{ikz}}{i\lambda z}\exp[\frac{ik}{2z}(x^2+y^2)]\} \\ &= e^{ikz}\exp[-i\pi\lambda z(f_X^2 + f_Y^2)]. \end{aligned} \tag{1.20}$$

## 1.4 Fourier transforming properties of lenses and 4-f system

A lens is an optical device made of transparent material that can focus or disperse light through refraction. A common lenses are spherical lenses, with two surfaces parts of the sphere surfaces. Both the radius and the sign of the curvature of both surfaces of a lens determine the behavior of a lens. A biconvex or convex lens makes collimated light converge to a spot, as illustrated in Fig.1.2. For a thin lens situation, the distance between the spot and the lens is defined as the focus length $f$.

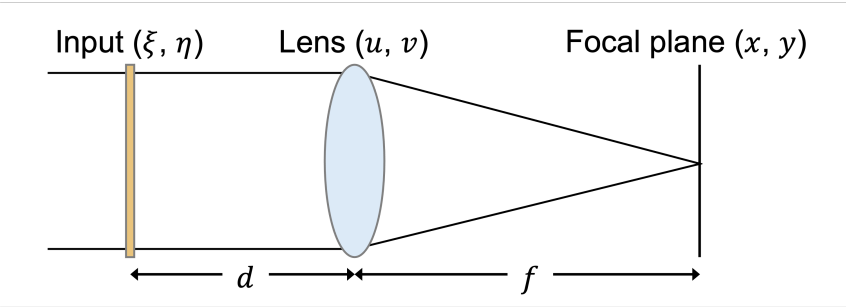


Figure 1.2: Light passes through a lens.

The behavior of a lens can also be interpreted from wave optics perspective. A lens adds phase delay to the incident wave. Combining the geometry of a lens and the paraxial approximation [1], the phase transformation of a thin lens is written as:

$$t_l(u, v) = \exp[-i\frac{k}{2f}(u^2 + v^2)] \tag{1.21}$$

where $k$ is the wave number of the incident light, and $f$ is the focal length of the lens.

For the situation illustrated in Fig.1.2, a monochromatic plane wave of amplitude $A$ is assumed to be uniformly and normally incident on the input plane with transmission coefficient $t_A(\xi, \eta)$, in which case the field distribution at the input plane is:

$$U_o = A \cdot t_A(\xi, \eta). \tag{1.22}$$

The wave propagation process can be decomposed into three steps: 1) light propagates for a distance of $d$ from the input plane to the lens, 2) the lens applies a phase delay to the wave, and 3) the wave exits the lens and propagates for a distance of $f$ to the focal plane. Considering all the propagation as Fresnel propagation and neglecting the finite lens aperture, the final field distribution on the focal plane can be written as:

$$U_f(u,v) = A\exp[i\frac{k}{2f}(1-\frac{d}{f})(u^2+v^2)] \times \iint_{-\infty}^{\infty} t_A(\xi,\eta)\exp[-i\frac{2\pi}{\lambda f}(\xi u+\eta v)]d\xi\, d\eta. \tag{1.23}$$

From eq.1.23, we can find that for the special case where $d = f$, in other words, when the input plane is right at the front focal plane of the lens, the behavior of the lens becomes an exact Fourier transform.

Based on the Fourier properties of a lens, a coherent 4-f type imaging system in free space can be designed whose scheme is shown in Fig.1.3. The two lenses are placed at the exact distance such that the back focal plane of the first lens is exactly the front focal plane of the second lens. During imaging, the sample is placed at the front focal plane of the first lens, and the image is formed at the back focal plane of the second lens. The spatial domain is transformed to the spatial frequency domain by the first lens, and then the spatial frequency domain is transformed back to the spatial domain by the second lens. By setting $f_2$ far larger than $f_1$, a microscope with high magnification can be achieved, where the first lens is named the objective lens and the second lens is named the tube lens.

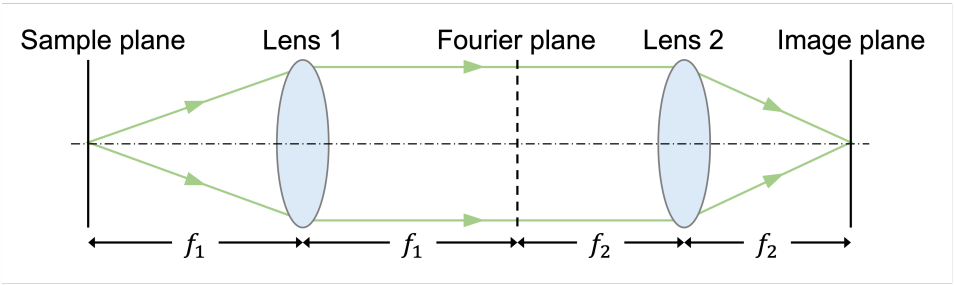


Figure 1.3: A typical 4-f system, where the back focal plane of the first lens is exactly the front focal plane of the second lens.

From the 4-f system, it is obvious that only the spatial frequency components that can pass through the pupil plane can contribute to the final image, indicating that the 4-f system with a limited aperture is a low-pass filter in the spatial frequency domain. From a system perspective, the 4-f system is linear in complex amplitude, and its amplitude transfer function (object space) determined in the frequency domain is just the pupil function, which is a circular function for the most common case with

a circular lens:

$$H(f_X, f_Y) = circ(\frac{\sqrt{f_X^2 + f_Y^2}}{\lambda \sin\theta}) \tag{1.24}$$

where $w$ is the radius of the pupil size, and $\theta$ is half of the maximum angle of the cone of light that can enter the optical system, as illustrated in Fig.1.4. The cutoff frequency can be then written as:

$$f_c = \frac{\sin\theta}{\lambda}. \tag{1.25}$$

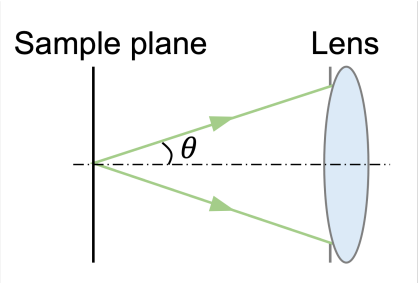


Figure 1.4: Numerical aperture geometry, assuming the aperture limits the maximum cone of light passing through the lens.

From the transfer function of the coherent 4-f system, the concept of numerical aperture (NA), which is widely used in microscopy research, can be connected to the Fourier analysis of the 4-f system. The NA represents the maximum spatial frequency component that an optical system can receive, defined as:

$$NA = n \cdot \sin\theta. \tag{1.26}$$

The NA indicates the resolving power of the microscope. For a coherent imaging situation, the resolution of the microscope is:

$$res(coherent) = \frac{\lambda}{NA}. \tag{1.27}$$

For systems in free space, the refractive index $n$ is 1. Applying the approximation of $\sin\theta \approx \theta$, the resolution of a coherent microscope is the reciprocal of the cutoff frequency derived from eq.1.25. The NA and the frequency analysis of a coherent 4-f system converge.

Coherent imaging systems are linear in complex amplitude, while incoherent systems are linear in intensity (the modulus squared of amplitude). Incoherent systems use

the optical transfer function (OTF) rather than the amplitude transfer function. The OTF, being the auto-correlation of the pupil function based on the auto-correlation property of the Fourier transform, gives incoherent systems a cutoff frequency twice that of coherent systems with the same pupil size. Consequently, incoherent systems achieve twice the resolution of coherent systems:

$$res(incoherent) = \frac{\lambda}{2NA}. \tag{1.28}$$

## 1.5 Mie scattering

Scattering is a type of light-particle interaction. Many phenomena are caused by light scattering, such as the blue color of the sky, the red sky at sunset, and the white or gray color of clouds. Maxwell's equations are the fundamental theory describing the behavior of light during the scattering process. The exact solution for a particle with an arbitrary shape can be difficult to solve, but for simpler cases, such as scattering by a homogeneous sphere, the exact solution has been well studied by Gustav Mie, and these solutions have since been referred to as Mie scattering theory [2].

The exact solution to Maxwell's equations is not unique and depends on the specific conditions of each situation. In the case of scattering by a homogeneous sphere, the conditions applied to Maxwell's equations are:

- The boundary conditions at the interface between the sphere and the surrounding medium.
- The solution is bounded at the origin.
- The asymptotic field at infinity corresponds to a diverging spherical wave in the scattering case.

The detailed mathematical expressions for the Mie scattering solution will be discussed in Chapter III. Here, we highlight two key parameters in a scattering scenario that influence the scattering field distribution and intensity. The first is the relative refractive index $m$, defined as the ratio of the refractive index of the sphere $n_p$ to that of the surrounding medium $n_m$:

$$m = \frac{n_p}{n_m}. \tag{1.29}$$

A larger $m$ indicates a greater refractive index difference between the particle and the surrounding medium, which typically results in more noticeable scattering. To

illustrate the role of the relative RI $m$, consider the extreme case where the particle and the medium have the same RI ($m = 1$). In this scenario, the entire system becomes homogeneous, and as a result, light scattering no longer occurs.

The second important parameter is the size parameter $x$, defined as:

$$x = \frac{2\pi r}{\lambda} \tag{1.30}$$

where $r$ is the radius of the scattering sphere and $\lambda$ is the wavelength of the incident light. The size parameter determines both the intensity and the distribution of scattered light. For particles with sizes comparable to the wavelength, scattering tends to be more uniform in all directions. However, for particles much larger than the wavelength, forward scattering becomes dominant.

## 1.6 Deep learning for computer vision

Machine learning (ML) [3–6] is a field focused on developing statistical algorithms capable of learning patterns from data, generalizing to unseen data, and performing tasks without explicit instructions. Depending on the type of information available to the system, ML can be divided into various paradigms, including supervised learning, unsupervised learning, and reinforcement learning.

Supervised learning [7, 8] is one of the most widely used paradigms in machine learning. As the name suggests, the system is trained with labeled data, where both the input and the corresponding output are provided. The goal of training is to discover the rule that maps the inputs to the outputs. The typical process of supervised learning includes several steps: 1) determining the type of training examples, 2) gathering the dataset, 3) defining the input representation, 4) selecting the learning algorithm, 5) training the model, and 6) evaluating the model's performance.

Neural networks [9, 10] are a type of learning algorithm that inspired by the structure of biological neurons in the brain, with artificial neurons arranged in layers and connected across them. During training, the network adjusts these connections through backpropagation [10], so it can generate the expected output given an input. As research in neural networks advanced and computational hardware improved, deep neural networks (DNNs) became increasingly common. The term "deep" refers to the many layers in the network, which can range from hundreds to thousands. These layers allow DNNs to recognize complex inputs and have made them highly effective in fields like image recognition [11–16] and natural language processing [17–19].

In computer vision, common deep learning tasks include image classification and object detection, both of which are illustrated in Fig.1.5. Image classification involves the DNN identifying the class of an object in an image (e.g., recognizing a cat), while object detection requires the DNN to locate and identify all instances of certain objects (such as humans, buildings, or cars) within an image. Significant progress has been made in these areas, from the creation of large datasets like ImageNet [20] and COCO [21] to the development of powerful architectures such as ResNet [13], EfficientNet [22], and Faster-RCNN [23].

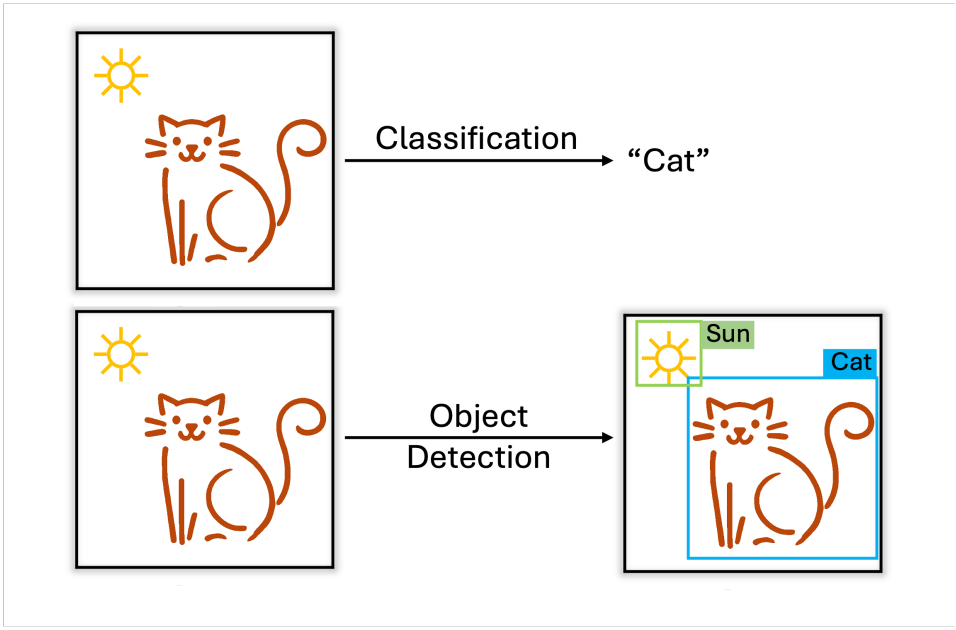


Figure 1.5: Image classification and object detection.

## 1.7 Thesis outline

This thesis presents methods for extracting three types of information beyond morphology by enhancing microscope systems, integrating physical models, and applying advanced image processing techniques. These include: 1) depth information, 2) object size information, and 3) developmental information of objects.

Chapter 2 introduces a method to extract depth information using an all-in-focus imaging technique based on Fourier Ptychographic Microscopy (FPM). By reconstructing a multi-focal image stack, this method generates both an all-in-focus image and a corresponding depth map. This approach is useful for thyroid fine needle aspiration samples, as it minimizes the need for pathologists to constantly adjust the focal plane, benefits data transfer, and could also support machine learning applications

in cytology.

Chapter 3 and 4 focus on a non-destructive subvisible particle (SbVP) analyzer for estimating the size and concentration of SbVPs in drug products. This analyzer aims to estimate the size and concentration of SbVPs within a drug product while keeping the sample intact. Incorporating a light-sheet microscope with custom housings to compensate for container-induced astigmatism, it uses Mie scattering theory to estimate the size of the particles. Its functionality is demonstrated on polystyrene beads and biological drug products. Additionally, a new metric named the number of fringes is discovered from the same microscope images, which could serve as a more precise and robust size indicator beyond scattering light intensity. This new size indicator is used to train a particle detection neural network, verifying its effectiveness through its performance.

Chapter 5 is about an embryo sex classification project, aiming to extract subtle developmental differences between male and female embryos from early development videos taken by an Embryoscope. A combined convolutional and recurrent neural network structure is employed. While the prediction accuracy reaches 61%, which is not high, the deep learning model outperforms both human and random predictions, demonstrating its ability to extract embryo developmental information from the Embryoscope videos to some extent.

## References


[1] Joseph W. Goodman. "Introduction to Fourier optics. 3rd." In: *Roberts and Company Publishers* (2005).

[2] Craig F. Bohren and Donald R. Huffman. *Absorption and scattering of light by small particles*. John Wiley & Sons, 2008.

[3] Trevor Hastie et al. *The elements of statistical learning: data mining, inference, and prediction.* Vol. 2. Springer, 2009.

[4] Kevin P. Murphy. *Machine learning: A probabilistic perspective.* MIT press, 2012.

[5] Leslie G. Valiant. "A theory of the learnable." In: *Communications of the ACM* 27.11 (1984), pp. 1134–1142.

[6] Michael I. Jordan and Tom M. Mitchell. "Machine learning: Trends, perspectives, and prospects." In: *Science* 349.6245 (2015), pp. 255–260.

[7] Pádraig Cunningham, Matthieu Cord, and Sarah Jane Delany. "Supervised learning." In: *Machine learning techniques for multimedia: Case studies on organization and retrieval*. Springer, 2008, pp. 21–49.

[8] Trevor Hastie et al. "Overview of supervised learning." In: *The elements of statistical learning: Data mining, inference, and prediction* (2009), pp. 9–41.

[9] Kevin Gurney. *An introduction to neural networks.* CRC Press, 2018.

[10] Robert Hecht-Nielsen. "Theory of the backpropagation neural network." In: *Neural Networks for Perception*. Elsevier, 1992, pp. 65–93.

[11] Md Zahangir Alom et al. "The history began from alexnet: A comprehensive survey on deep learning approaches." In: *arXiv preprint arXiv:1803.01164* (2018).

[12] Dan Ciregan, Ueli Meier, and Jürgen Schmidhuber. "Multi-column deep neural networks for image classification." In: *2012 IEEE Conference on Computer Vision and Pattern Recognition*. IEEE. 2012, pp. 3642–3649.

[13] Kaiming He et al. *Deep residual learning for image recognition.* 2015. arXiv: 1512.03385 [cs.CV]. URL: https://arxiv.org/abs/1512.03385.

[14] Chetan L. Srinidhi, Ozan Ciga, and Anne L. Martel. "Deep neural network models for computational histopathology: A survey." In: *Medical Image Analysis* 67 (2021), p. 101813.

[15] Brahim Ait Skourt, Abdelhamid El Hassani, and Aicha Majda. "Lung CT image segmentation using deep neural networks." In: *Procedia Computer Science* 127 (2018), pp. 109–113.

[16] Jurgen Schmidhuber. "Multi-column deep neural networks for image classification." In: *Proceedings of the 2012 IEEE Conference on Computer Vision and Pattern Recognition (CVPR)*. 2012, pp. 3642–3649.

[17] Li Deng, Geoffrey Hinton, and Brian Kingsbury. "New types of deep neural network learning for speech recognition and related applications: An overview." In: *2013 IEEE International Conference on Acoustics, Speech and Signal processing*. IEEE. 2013, pp. 8599–8603.

[18] Xiaodong Liu et al. "Multi-task deep neural networks for natural language understanding". In: *arXiv preprint arXiv:1901.11504* (2019).

[19] Ronan Collobert and Jason Weston. "A unified architecture for natural language processing: Deep neural networks with multitask learning." In: *Proceedings of the 25th international conference on Machine learning*. 2008, pp. 160–167.

[20] Jia Deng et al. "Imagenet: A large-scale hierarchical image database." In: *2009 IEEE Conference on Computer Vision and Pattern Recognition*. IEEE. 2009, pp. 248–255.

[21] Tsung-Yi Lin et al. *Microsoft COCO: Common objects in context.* 2015. arXiv: 1405.0312 [cs.CV]. URL: https://arxiv.org/abs/1405.0312.

[22] Mingxing Tan. "Efficientnet: Rethinking model scaling for convolutional neural networks." In: *arXiv preprint arXiv:1905.11946* (2019).

[23] Shaoqing Ren et al. *Faster R-CNN: Towards real-time object detection with region proposal networks.* 2016. arXiv: 1506.01497 [cs.CV]. URL: https://arxiv.org/abs/1506.01497.

*Chapter 2*

# ALL-IN-FOCUS FOURIER PTYCHOGRAPHIC MICROSCOPY FOR FINE NEEDLE ASPIRATION BIOPSY

Cytologic preparations consist of preparations of whole cells where cells commonly cluster and aggregate. As such, they are generally much thicker than histologic slides, resulting in large patches of defocus when examined under the microscope, requiring pathologists to continually manipulate the focal plane, complicating the task of accurately assessing the entire cellular aggregate and thus in making a diagnosis. Further, it is extremely difficult to acquire useful uniformly in-focus digital images of cytology preparations for applications such as remote diagnostic evaluations and artificial intelligence models. In this chapter we report a unique imaging method that can acquire cytologic images efficiently and computationally render highly compact all-in-focus digital images based on Fourier ptychographic microscope (FPM). First FPM is introduced and its maximum achievable numerical aperture and ability to extend depth of field is analyzed and experimental verified. Then the procedure of synthesizing all-in-focus images are elaborated. Finally, we report all-in-focus FPM results of thyroid fine needle aspiration (FNA) cytology samples, demonstrating our method's ability to overcome the height variance caused by cell aggregation, and rendering images at high resolution and that are all-in-focus.

## 2.1 Introduction of FPM

Fourier Ptychographic Microscopy (FPM) [1, 2] is a computational microscopy method that adapts and combines the key concepts of synthetic aperture and phase retrieval to allow the user to synthesize a series of low resolution microscopy images into a high resolution microscopy image. The input set of low resolution images are acquired through a standard microscopy where the illumination light is varied in its illumination angle for each of the raw images. In the angular spectrum space, the information of the raw images overlaps with each other. By exploiting the information redundancy in the overlap regions, we can then apply phase retrieval methods [1, 3–7] to reconstruct the missing phase information and allow us to apply synthetic aperture concept to correctly stitch the disparate raw data in the angular spectrum space into a contiguous wide spanning and accurate angular spectrum representation of the original microscopy sample. When transformed

back into the spatial domain, the resulting image has improved resolution and the original field-of-view. By this means, FPM enables the user to generate images with superior resolution than what the native numerical aperture (NA) of the microscope is supposed to be able to provide. As a reference point, the original FPM paper [1] showed that an objective of NA 0.08 when used in an FPM format was able to generate images with resolution comparable to that achieved by an objective of NA 0.5 for a standard microscope.

In addition to improving resolution, the FPM's computational microscopy algorithmic approach allows the user to correct inherent physical system aberrations by nesting the aberration correction functions in its algorithm. This ability enabled a shift in standard microscopy design paradigm—prior to FPM's invention, it was generally assumed that the correction of aberration needs to be done in the physical world by building physical microscopes with as little aberrations as possible. FPM showed that an intrinsically imperfect microscope can still be used generate optically 'perfect' (aberration-free) images by mathematically correcting aberrations in the computational image processing [7]. This substantial advantage was leveraged in parallel microscopy implementations, where very compact but highly aberrative microscope arrays can be used to perform high-quality parallel imaging by using FPM to correct aberration computationally [8].

A corollary consequence of this computation aberration correction ability is that the FPM method can also be applied to digitally refocus its rendered images as desired. This digital refocusing ability can substantially extend the effective depth-of-field of the microscope by several factors beyond its native depth-of-field as dictated by the NA of the objective. In the original FPM paper, the DOF of a 2x objective (0.08NA) was extended from ~80 $\mu$m to ~300 $\mu$m [1].

### 2.2 Analysis of NA upper limit, resolution and depth of field of FPM

According to the Fourier frequency model of FPM, the final range that the sample spectrum can cover, given sufficient redundancy among the sub-apertures, is determined by both the size of the objective lens pass band and the location of the sub-apertures, which is governed by the maximum oblique illumination angle. Therefore, the synthetic NA of FPM, denoted as $NA_{syn}$, is expressed as eq.2.1:

$$NA_{syn} = NA_{obj} + NA_{illu} \tag{2.1}$$

where $NA_{obj}$ is the NA claimed by objective lens and $NA_{illu}$ is the maximum illumination NA (the largest illumination angle).

As a result, a question remains to be addressed: What is the maximum numerical aperture (NA) that a free-space FPM system can achieve? Before discussing the all-in-focus method applied to FPM, we first aim to explore the basic properties of FPM, including its NA limitations. Here, we report our findings on combining some of the previously reported methods to implement an FPM system with a NAsyn of 1.9 – close to the theoretical upper limit of 2. Our experiment is aimed at studying whether FPM is able to perform well at this high NAsyn limit, and whether any non-obvious complications need to be addressed to achieve optimal performance. To accomplish this task, we implemented a high-NA system with an objective of NA = 0.95 and an LED quasi-dome with illumination NA = 0.95. On the processing side, we adapted and combined illumination correction circular edge detection (CED) [9] and simulated annealing (SA) algorithm [10, 11] within the algorithm to generate high quality FPM reconstruction. Our high-NA FPM implementation has a sparrow-limit based, full pitch resolution 266 nm with 465 nm incident light when measured on a Siemens star target. The related work, the experiment set-up, the resolution comparison with a standard high-NA microscope, and comparison images taken of biological samples will be elaborated.The measured depth-of-field performance (DOF) of this high NA FPM system are additionaly reported as well.

**Related work exploring NA upper limit of FPM**

The twin advantages of resolution improvement and extended DOF associated with the FPM method have been extensively studied over the past decade [7–17]. Of particular interest within the community is the improvement in resolution which is directly determined by the synthetic NA of FPM.As such, there are two ways to improve the resolution of FPM: increase $NA_{obj}$ or increase $NA_{illu}$. Under free space condition, both $NA_{obj}$ and $NA_{illu}$ have a theoretical upper limit of 1, resulting in $NA_{syn}$ having a theoretical upper limit of 2. In prior research, there have been numerous efforts aimed at increasing the synthetic NA towards this maximum limit: flat LED array (0.75 NA) with a moderately high NA objective (0.75 NA) [18], hemispherical LED condenser (0.95 NA) with a low NA objective (0.1 NA) [16] and planner LED condenser (0.93 NA for dry, 1.2 NA for oil immersion) with a moderate low NA objective (0.4 NA) [11]. The respective synthetic NA attained by these prior works are, respectively, 1.5, 1.05, 1.33 (dry) and 1.6 (oil immersion).

**Experimentally implementing FPM with near maximum system NA**

**Experimental set up**

Fig.2.1(a) shows the schematic of the high-NA FPM set up. We implemented an inverted transmission FPM system for this experiment. An LED quasi-dome with illumination NA of 0.98 [19, 20] was mounted ~50 mm above the focal plane of a 50x/0.95 objective (Olympus MPLAPON50X), resulting a 0.53 mm-diameter field of view. A CCD camera (Hamamatsu C11440-42U30, 6.5 $\mu$m x 6.5 $\mu$m) served as our imaging camera. During the data acquisition process, we illuminated the sample with 39 LEDs on the dome successively to generate the raw data, resulting in an effective illumination NA of 0.95 and a total synthetic NA of 1.9. The center wavelengths of the full-color LED were 621 nm (red), 525 nm (green), and 465 nm (blue), and the average power of the red, green and blue LEDs were 1.6 mW, 3.5 mW and 3.4 mW, respectively. With the large range of illumination angle involved, the collected images have a large span of intensities. To accommodate the large dynamic range, we adopted two procedures to avoid camera saturation. First, the camera exposure times were set separately, for low NA ($\geq$ 0.75) illumination to be 0.3 s and for high NA (>0.75) illumination to be 5 s. Second, for each high NA illumination, 3 images were taken and then averaged as the final raw data. The total acquisition time for the entire sequence of raw images at one color channel added up to about 12 mins.

The image processing procedure is summarized in Fig.2.1(b). We performed illumination angle calibration prior to image reconstruction. We used one raw data set for this procedure (described in Section 2B). This procedure accurately determines the illumination angle associated with each LED and provides us with an accurate determination of the Fourier frequency shifts in Fourier domain. We then employed embedded pupil function recovery (EPRY)[7] reconstruction in a FPM iteration loop to correct for residual aberrations and output a high-NA FPM image. In our experiments, illumination correction was only performed once after the system has been set up. Subsequent FPM rendering all share the same calibrated illumination data.

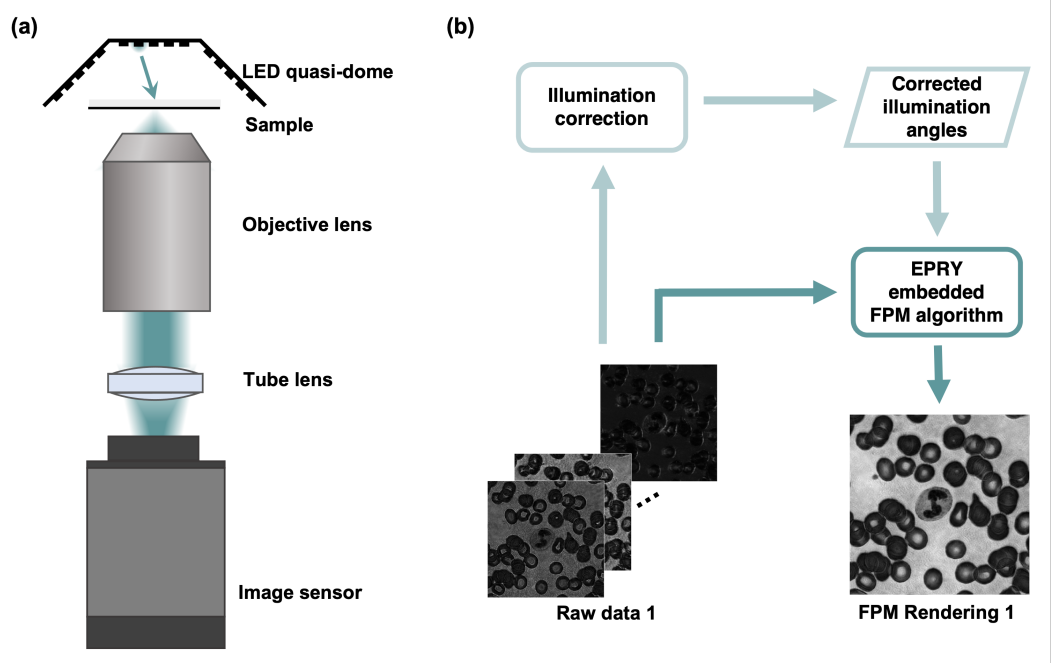


Figure 2.1: Experimental set up and general process. (a) Schematic of experimental set up. (b) Experiment procedures: One group of raw data was used for illumination correction first. Calibrated illumination angles were then used for FPM rendering.

### Illumination correction

Accurate determination of illumination angle and corresponding Fourier frequency shift induced by each oblique illuminating LED is essential for high quality FPM reconstruction. Unlike flat LED array, whose simple geometry makes it straightforward to calculate Fourier frequency shifts, the LED quasi-dome has complicated LED distribution, hindering direct and accurate calculation of Fourier frequency shifts. With only rough values of the Fourier frequency shifts, FPM reconstruction would be inaccurate, and the resulting images would appear blurry and distorted, as showed in Fig.2.2(c1). To perform successful illumination correction, we first performed pre-iteration coarse position correction, followed by iterative fine intensity and position correction (see Fig.2.2(a-b)).

We used circular edge detection (CED) [9] as our coarse position correction method (see Fig.2.2(a)). As the maximum illumination NA matched the objective NA in our experiment, all raw images were bright field images. As showed in Fig.2.2(a), the Fourier spectrum of a bright field image contains two obvious centrosymmetric circles, for which CED has been showed in prior works [9] to be effective for coarse position correction. By jointly considering the first and second derivation of the

Gaussian filtered spectrum [9], both of which indicate the circle edge, CED can estimate the position of the circle center. Fig.2.2(c1-c2) shows the FPM image improvement in a Siemens star image when CED was used for coarse position correction. However, we also note that while Fig.2.2(c2) (CED corrected) is visibly sharper over Fig.2.2(c1) (no correction), there are still significant spoke distortions (marked by yellow arrows) that indicate a need for further improvement.

For finer corrections, we next performed iterative fine intensity and position correction to further improve the FPM reconstruction quality. The fine correction was based on simulated annealing (SA) algorithm [10] and was embedded within the embedded pupil function recovery (EPRY) [7] FPM reconstruction process. Fig.2.2(e) is a schematic of the workflow. Within one iteration, for each raw image, intensity correction was first performed prior to the execution of the SA algorithm. The SA algorithm then performed fine correction of the Fourier frequency shift (see Fig.2.2(b)). The FPM algorithm then rendered an FPM image complete with phase information. Using this rendered FPM data set and Fourier frequency shift values used by the SA algorithm, we then generated a set of estimated oblique illumination images that correspond to the original set of oblique illumination raw images. If we have the correct Fourier frequency shift values, these two sets should match each other exactly. As such we can use the mean square error of the image differences for these two sets as a predictor of whether the correct Fourier frequency shifts have been achieved. We continued to run this nested workflow until this mean square error was minimized. For our setup, the final corrected illumination map is showed in Fig.2.2(d). A corrected Siemens star image rendered through this process is shown in Fig.2.2(c3). Compared to the prior two images, we can clearly see that it has the sharpest appearance and the least distortions.

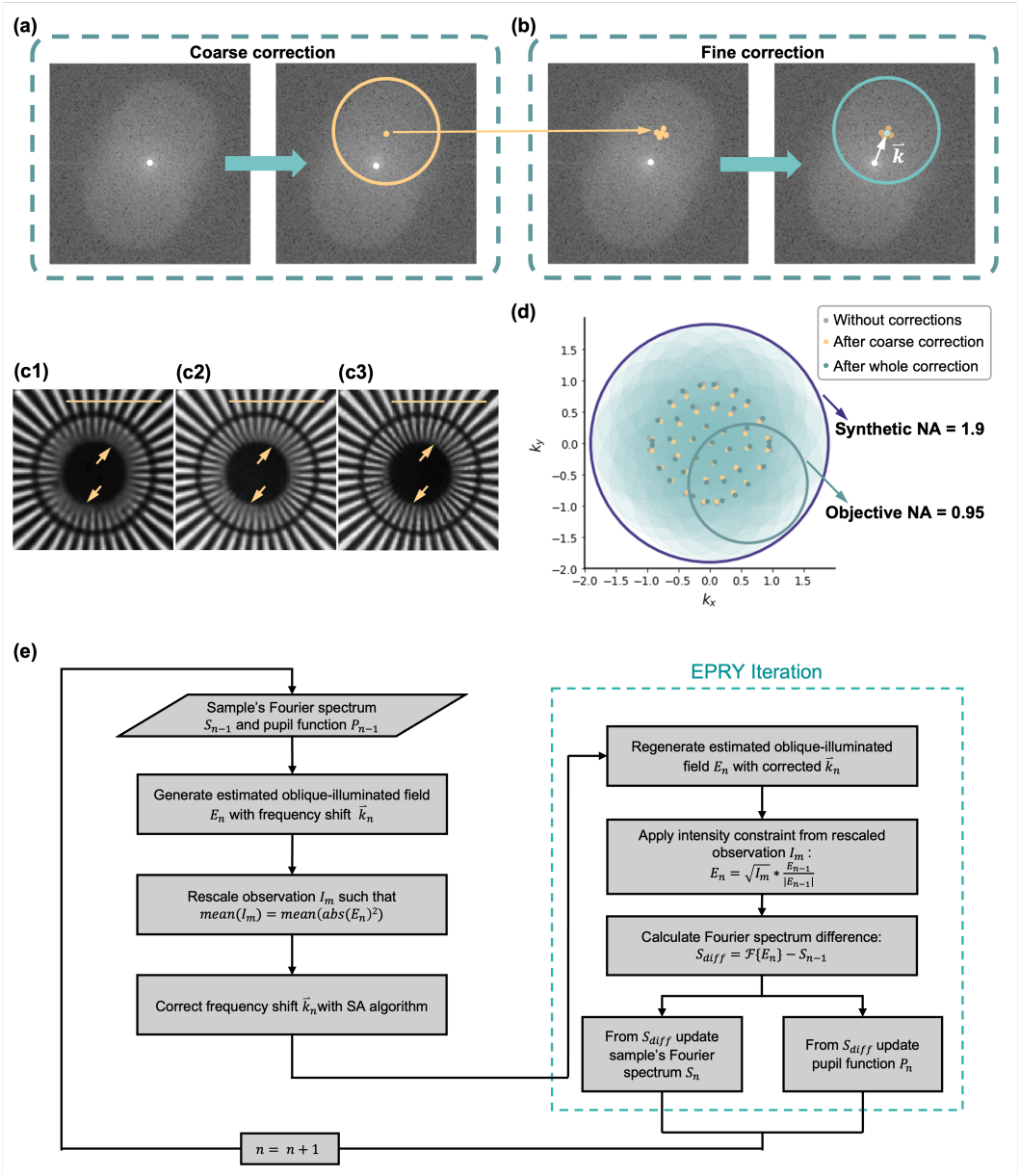


Figure 2.2: Illumination correction scheme. (a) Schematic of coarse correction algorithm: CED found the circle edge in Fourier spectrum and then determined the circle center. (b) Schematic of fine correction: SA algorithm generated offset sets and selected the one that resulted in minimum mean square error. (c) FPM reconstruction results with different extend illumination correction (scale bar: 5 $\mu$m): (c1) No correction. (c2) Only coarse correction. (c3) Coarse and fine correction. (d) Illumination scheme after whole correction. Objective NA: 0.95. Synthetic NA: 1.9. Points: illumination angles in Fourier space (grey: angles without corrections, yellow: angles after coarse correction only, green: angles after whole correction). (e) Flowchart of fine illumination correction algorithm.

**Results of near maximum NA FPM and system property analysis**

**Resolution assessment and pupil correction**

We assess the resolution performance of the high-NA FPM system and compare it with a standard transmission (incoherent) microscope imaging under 0.95 NA brightfield illumination. We selected these two system for comparison because they share the same pass band in Fourier frequency domain [21]. A Siemens star (Ready Optics, 2017_Pair) target was imaged under blue light (465 nm) with the imaging strategy described in Section 2A to experimentally determine the resolution. The Sparrow-limit criteria was adopted here and resolution was defined as the smallest periodicity at which all spokes are observable (full-pitch resolution) [22–24]. This assessment is less prone to resolution mis-reporting and can be applied to compare resolution performance of different microscopy methods [23]. The Siemens star target can be used to examine a large range of spatial frequencies along all directions and verify the degree of isotropy of the imaging system. As such, it can prevent the latent risk of reporting higher Fourier frequency that can only be resolved along specific directions. Such risk would be an issue for targets such as USAF target [11, 16] and two-slit target [16], as those targets generally allow resolution characterization in only 2 directions. Siemens star target is also helpful in revealing aberrations, as the spokes will appear distorted or blurry when imaged by an aberrated imaging system. We performed simulation to find reliable resolution expressions for both systems with Siemens star as a target. For completeness, the specific process and results are reported in Supplementary document.

According to our simulation, a high-NA FPM system has a theoretical resolution (Sparrow-limit) determined by:

$$Res_{hnFPM} = \frac{\lambda}{NA_{syn}} = 245nm. \tag{2.2}$$

With the same generalized simulation, we also found that the theoretical resolution (Sparrow-limit) of the standard transmission microscope is given by:

$$Res_{tr} = 0.57 \times \frac{\lambda}{2 \times NA_{obj}} = 278nm \tag{2.3}$$

where $\lambda$ is the incident wavelength.

Our imaging experiment with both the high-NA FPM and the standard transmission microscope yielded Siemens-star target images that are shown in Fig.2.3(a1) and (b1). We additionally show the normalized intensity plots along the smallest

circles where all spokes are resolvable for high NA FPM (green circles) and standard transmission microscope (blue circles) are included as well (Fig.2.3(a2-3) and Fig.2.3(b2-3)). Fig.2.3(a2) shows that spoke periodicity of 266 nm is just resolvable by our high NA FPM system, and thereby establishing its resolution to be 266 nm, which is 9% deviated from the theoretical resolution prediction. Fig.2.3(b3) shows that that spoke periodicity of 318 nm is just resolvable by the standard transmission system, and thereby establishing its resolution to be 318 nm, which is 15% deviated from the theoretical resolution prediction.

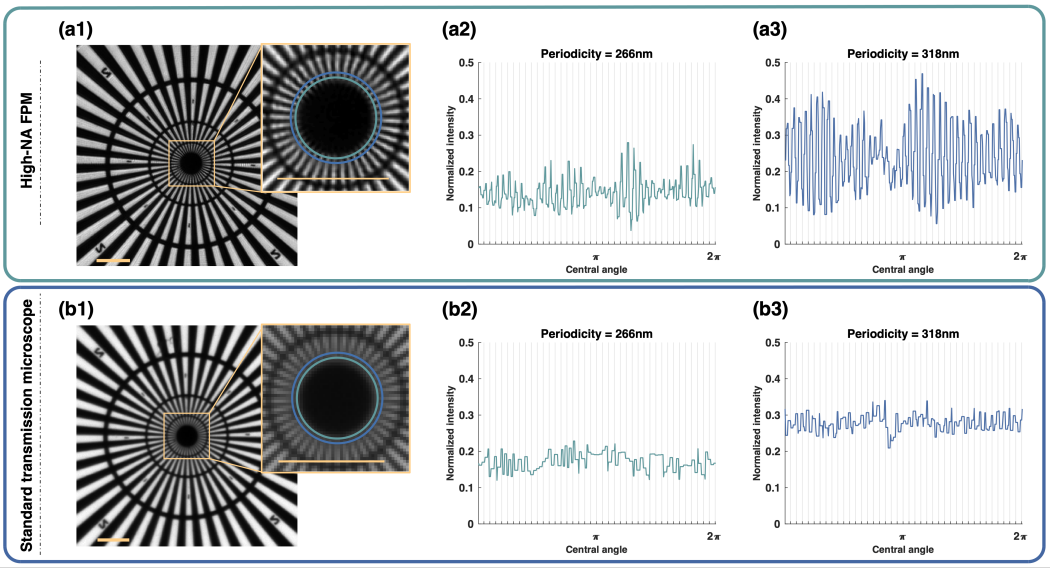


Figure 2.3: Siemens star imaging and resolution quantification. (a) Siemens star imaged by high-NA FPM (a1) and intensity plots along green (a2) and blue (a3) rings. (b) Siemens star imaged by standard transmission microscope (b1) and intensity plots along green (b2) and blue (b3) rings. Scale bar: 5 $\mu$m.

The fact that high NA FPM outperformed standard transmission microscope in resolution can be attributed to 3 aspects.

First, we note that the contrast of the inner Siemens star spokes is notably higher for the high NA FPM systems compared to the standard transmission microscope (see Fig.2.3(a1) and Fig.2.3(b1)). This is because the high NA FPM benefits from coherent imaging where high Fourier frequency components are less attenuated than that in incoherent imaging.

Second, the high NA FPM system also benefits from EPRY's ability to correct residual aberration in conventional objectives—an ability missing from standard transmission microscopy, which has been previously reported in literature [7].

Third, intensity correction was adopted when high NA FPM was performed, compensating the inhomogeneity of different illumination angles and reducing weak-illumination-induced high Fourier frequency attenuation. To show that the impact of such corrections is significant for high NA FPM, we ran a comparison experiment where we did not compensate for the inhomogeneity. Fig.2.3(a) and Fig.2.4(a) shows the FPM image with and without compensation, respectively. The resolution achieved in the uncompensated processing is 294 nm—11% poorer than for the compensated processing. We further note that this issue is particularly acute for high NA FPM systems, as low NA FPM systems do not have to illuminate the sample at large grazing angles.

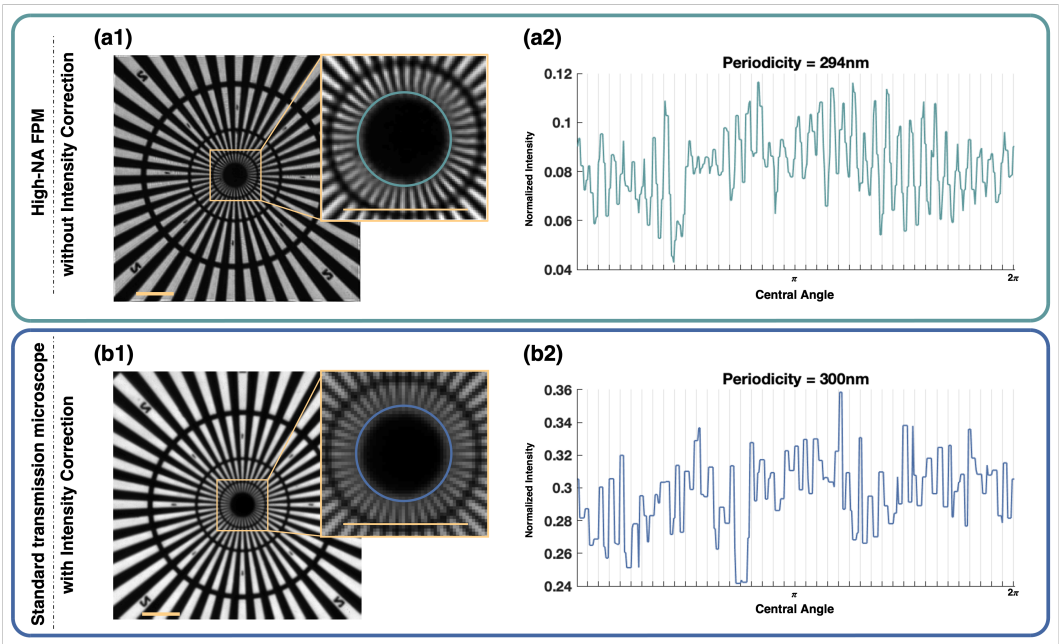


Figure 2.4: Experiments demonstrating the existence of illumination inhomogeneity. (a) High NA FPM image of Siemens star without intensity correction (a1) and intensity plots along minimum resolvable ring (a2). (b) Standard transmission microscope image of Siemens star with intensity correction (b1) and intensity plots along minimum resolvable ring (b2). Scale bar: 5 $\mu$m.

In principle, this type of intensity correction can also be performed for standard transmission microscopy. The illumination source would have to be designed such that the illumination intensity is carefully scaled based on the illumination angle. In a standard Kohler illumination scheme, a well-designed attenuation mask inserted at the right Fourier plane may be able to accomplish this at the cost of significant net attenuation. For our current study, we can derive the results for an equivalent inten-

sity correction for standard transmission microscope was performed by summing up the illumination-corrected (with method described in section 2B) raw data together to generating a standard transmission microscope image. Intensity corrected results of standard transmission microscope are demonstrated in Fig.2.4(b). The resulting resolution of standard transmission microscope was improved from 318 nm (15% deviation from simulation) to 300 nm (8% deviation from simulation). This clearly demonstrates the utility of illumination inhomogeneity compensation for both high NA FPM and high NA standard transmission microscopy.

**Imaging biology samples**

We performed color high-NA FPM imaging and color standard transmission microscope imaging on both a blood smear and a bone marrow smear (Precision for Medicine) We repeated the imaging procedure in Section 2.2 for each color channel and then synthesized RGB color channels together as color images. Fig.2.5 shows comparison images of the blood smear sample for the high-NA FPM system and the standard transmission microscope. In addition to the intensity images, the high-NA FPM system is also able to generate phase images (Fig.2.5(d) and (h)) and provide an objective aberration characterization in the form of the pupil wavefront for different regions of interest (ROIs) (Fig.2.5(e) and (i)) via the EPRY algorithm [7]. All reported phase images were acquired with blue light (465 nm) illumination. Consistent with our experimental findings in Section 2.2, the high-NA FPM reveals more detailed structures in the sample (indicated by arrows in Fig.2.5(b2), (c2), (f2) and (g2)).

For completeness, the imaging results of a bone marrow smear sample are reported in the Supplementary document. The results showed similar advantages for the high-NA FPM system.

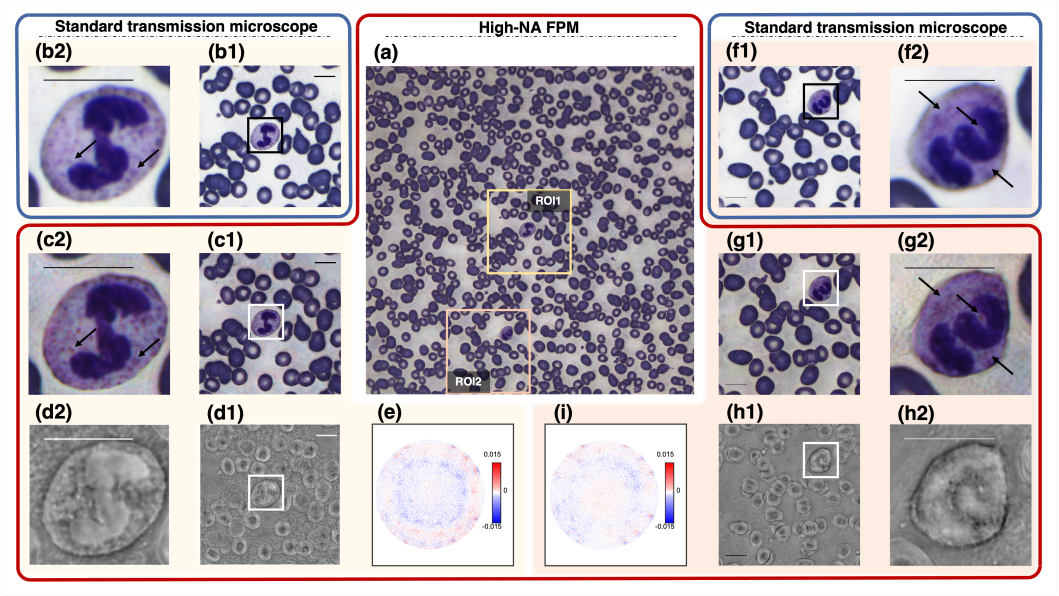


Figure 2.5: Blood sample imaging by high-NA FPM and standard transmission microscope. (a) Whole-frame color high-NA FPM blood smear image. (b) Color image of region of interest (ROI) 1 from standard transmission microscope. (c) Color image of ROI 1 from high-NA FPM. (d) Phase image reconstructed from blue channel of ROI 1. (e) Pupil aberration at ROI 1 reconstructed by EPRY algorithm from blue channel. (f) Color image of ROI 2 from standard transmission microscope. (g) Color image of ROI 2 from high-NA FPM. (h) Phase image reconstructed from blue channel of ROI 2. (i) Pupil aberration at ROI 2 reconstructed by EPRY algorithm from blue channel. Scale bar: 10 $\mu$m.

### Depth of field measurement

We examined the depth of field (DoF) of both the high-NA FPM and standard transmission microscope experimentally. A Siemens star displaced at controlled distances (defocus distances) from the objective lens focal plane was imaged by both high-NA FPM and standard transmission microscope with blue light (465 nm). 3-axis motorized stages (Thorlabs MLS203-1 for XY directions and Thorlabs MZS500-E for Z direction) were adopted to control defocus distances precisely. Digital refocusing [1, 7, 15] with light field initialization [25] was performed in high-NA FPM experiments. Resolutions under different defocus distances were determined with the same method as reported in Section 2.2. We varied the defocus distances from 0 $\mu$m to 5 $\mu$m, with 0.5 $\mu$m spacing. For both modalities, we calculated resolution deviations at each defocus distance from their corresponding in-focus resolution and interpolated by using piecewise cubic Hermite interpolating polynomial (PCHIP) [26, 27] method. Both measurement points and interpolated

curves are demonstrated in Fig.2.6(a). For completeness, the exact resolution values, images of Siemens star under different defocus distances taken by both image systems and corresponding resolution plots are included in the Supplementary document.

The DoF of NA-matched standard transmission microscope, denoted as $Dof_{tr}$, is given by

$$Dof_{tr} = \frac{\lambda \cdot n}{NA_{obj}^2} + \frac{n}{M \cdot NA_{obj}} \cdot e = 0.65\mu m \tag{2.4}$$

where $n$ is the refractive index, $M$ is the magnification of objective lens and $e$ is the camera pixel size. Then the half DoF of high-NA FPM, denoted as $Dof_{FPM}$, was estimated by finding the defocus distance where high-NA FPM's resolution deviation equals that of standard transmission microscope under half $Dof_{tr}$. Interpolated resolution deviation curves indicated defocusing half $Dof_{tr}$ lead to 8.2% resolution deterioration for standard transmission microscope. To accumulate the same amount of deterioration, the high-NA FPM system would have to be defocused by 1.8 $\mu$m. Thus, the DoF of our high-NA FPM setup was 3.6 $\mu$m (double of 1.8 $\mu$m) or 5.5 times longer than that of the standard transmission microscope.

It is also worth mentioning that, compared to standard transmission microscope, high-NA FPM achieved better resolution at every defocus distance, and has a more gradual resolution deterioration. This observation further supports the idea that high-NA FPM has better DoF properties, with not only extended DoF, but also less resolution deterioration when the defocus is high.

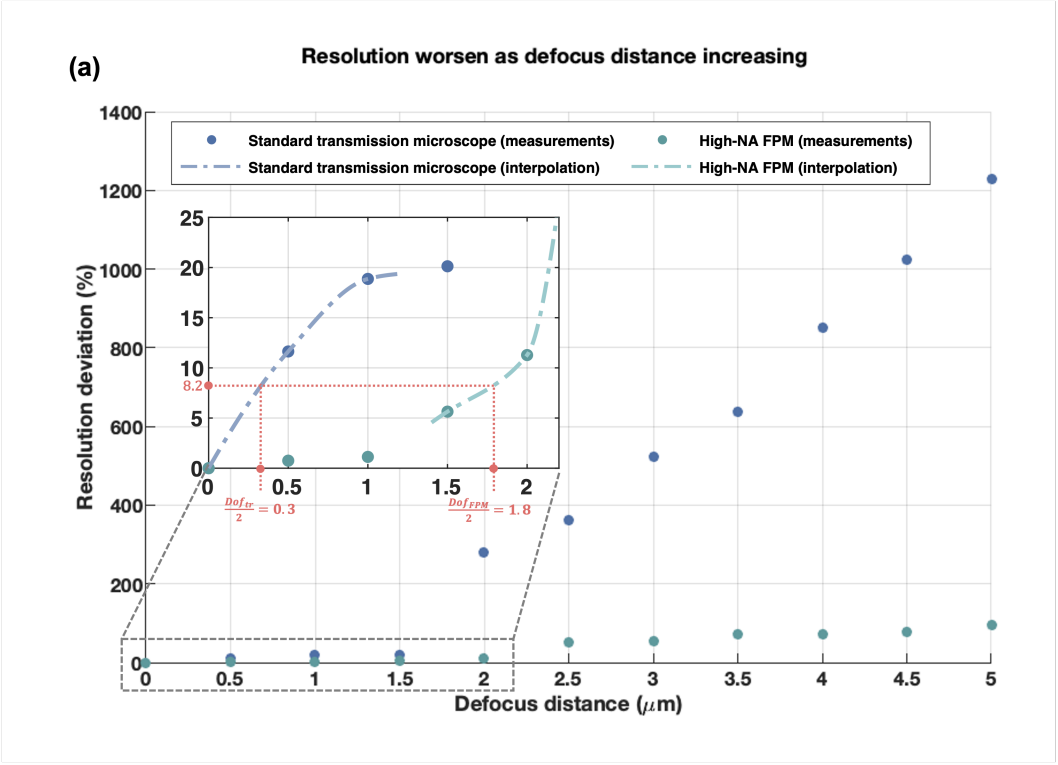


Figure 2.6: Resolution deviation as defocus distance increasing and DoF determination. (a) Relative deviation from in-focus resolution as defocus distance increased. Blue: standard transmission microscope. Green: high-NA FPM. Points: experiment measurements. Dash lines: PCHIP interpolated curves. The insert shows enlarged curves with defocus distance ranging from 0 $\mu$m to 2 $\mu$m and determination of high-NA FPM's DoF.

### High NA FPM system property analysis

The high-NA FPM system combined both close-to-limit high-NA (0.95) objective lens and close-to-limit high-NA (0.95) illumination. A synthetic NA of 1.9 was achieved, resulting in 266 nm full-pitch resolution (Sparrow-criterion) with 465 nm illumination. The DOF of the high-NA FPM was 3.6 $\mu$m, 5.5 times larger than that of a standard transmission microscope.

FPM takes advantage of oblique-illuminated data and is thus able to perform imaging at a NA higher than that claimed by the objective lens. However, as FPM is a coherent imaging method, this does not necessarily mean that its resolution would be substantially higher than that of a standard transmission microscope operating with the same objective. From Fourier optics' perspective, the pass band in Fourier frequency domain of coherent imaging is half that of incoherent imaging under

the same system NA (synthetic NA for FPM and objective lens NA for incoherent microscope). Therefore, to achieve the same pass band in Fourier frequency domain, the synthetic NA of FPM must be twice as large as the objective lens NA. This means that the illumination NA must match the objective lens NA. When the illumination NA exceeds the objective NA, FPM can outperform standard transmission microscope in resolution as FPM's synthetic NA is now more than double the objective's NA. This ability was demonstrated in the original FPM paper where an FPM system operating with a NA = 0.08 objective was able to render images comparable in resolution to images acquired in a standard transmission microscope with an objective of NA = 0.5.

In our current experiment, exceeding the objective's NA is not feasible as the objective's NA is already close to unity. Nevertheless, when we operate our FPM with the illumination NA matched to the objective's NA, we can still observe an observable resolution improvement compared to a standard transmission microscope operating with the same objective (as reported in Section 3A). These results are consistent with previous research reporting that FPM outperforms standard transmission microscope with comparable NAs [18] in resolution tests. In prior studies, the better FPM performance was attributed to the coherent imaging nature of FPM and FPM's ability to correct aberrations. For high synthetic NA, we found that the relative ease by which FPM setup can tailor and achieve illumination intensity homogeneity also contribute to FPM's ability to achieve better resolution than the standard transmission microscope. While standard transmission microscopy can only tailor illumination intensity at the hardware level, the FPM can actually correct for intensity heterogeneity during computation—by rescaling the data accordingly.

In conclusion, the study demonstrates that the experimental implementation of a high synthetic NA FPM can achieve resolution that is close to the theoretical predicted limit. In combination with the substantially longer effective depth of field (5.5 times longer) than a comparable standard transmission microscope, our study indicates that a well-designed and well-implemented high synthetic NA FPM can be a viable replacement for standard transmission microscope for high NA applications.

### 2.3 Background of fine needle aspiration and sample volumetric properties

Fine needle aspiration (FNA) biopsy is a safe, minimally invasive and widely used procedure to obtain diagnostic cytologic material from multiple organs, including the thyroid gland, breast, lung and pancreas [28–32]. In this procedure, the abnormal

tissue is sampled by a thin needle, expressed onto a glass slide, stained and then observed through a microscope. The collected sample generally contains clusters and aggregates of whole cells, the patterns of which often contain useful diagnostic information. Unlike histologic sections that are cut very thinly and generally have a uniform thickness across a slide, the aggregates of whole cells in an FNA vary in thickness. When viewed under a microscope, the cells are often distributed across multiple different focal planes requiring the pathologist to continually manipulate the focus to maintain a clear image. Importantly, it is extremely difficult to acquire useful digital images of cytologic preparations such as FNAs that are needed for remote diagnosis. Finally, cytology preparations have been very challenging to study with machine learning techniques, as out of focus areas render large areas unusable for analysis. Acquiring cytology images in which all planes can be seen in focus requires complex, time consuming and expensive scanning capabilities due to the fact that a cytology preparation can only be fully imaged by capturing images over multiple focal planes to constitute a volumetric image data set (z stack).

It would be advantageous if an FNA sample could be captured in a 2D image in which each of the non overlapping cells is optically in focus – an all in focus image. The 2D plane of interest is no longer flat but is a heterogenous plane that intersects each cell at its focal plane (Fig.2.7). Such an all in focus image is data efficient, as it is a 2D image information dataset and not a 3D volumetric dataset. Such an all in focus image is also highly suited to a pathologist's workflow, as a pathologist would be able see the vast majority of cells in focus without having to scroll through a z stack of scanned images. To be clear, such a 2D rendering would not work well for overlapping cells. Image information about overlapping cells can only be capitulated in a 3D volumetric image. Our proposed 2D strategy can work with FNA samples, because the majority of the cells are generally separated from each other by extensive fibrin clots formed during the procedures or simply by the cytoplasmic mass associated with the cells themselves.

To generate an all in focus image, we need to collect the phase and amplitude of the 2D wavefront emerging from the sample as this complete optical wavefront dataset will allow us to digitally refocus the image flexibly at different spatial points. FPM [1, 7, 33–35] provides the requisite capability to collect such 2D wavefront data. By applying a metric based digital refocusing to the FPM data, we can in turn render an all in focus image. We report all in focus FPM results of thyroid fine needle aspiration (FNA) cytology samples, demonstrating our method's ability to overcome

the height variance of 30 $\mu$m across the slide, as a result of cell aggregation, and rendering images at high resolution and that are all in focus.

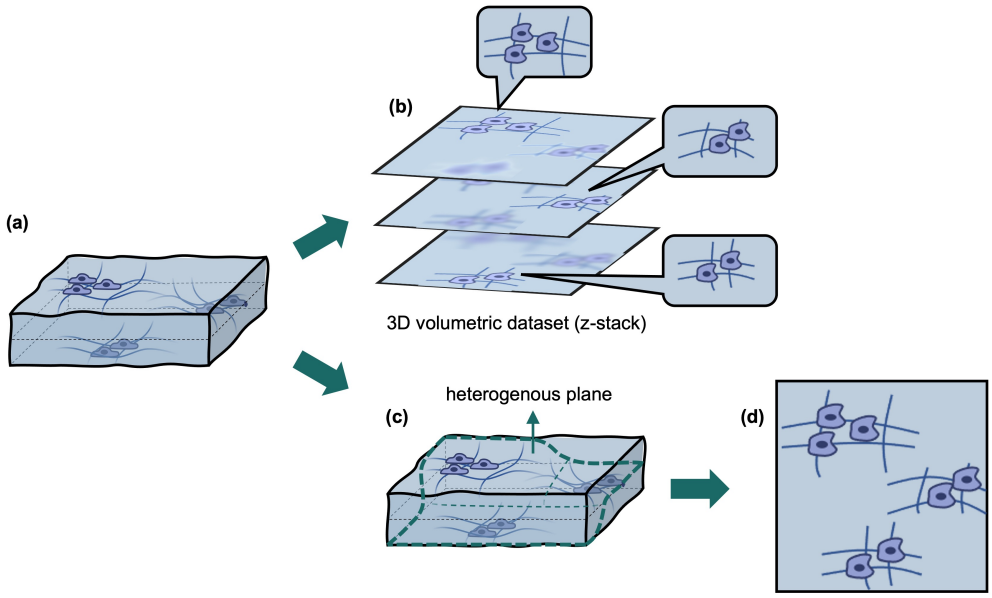


Figure 2.7: Methods to describe a FNA sample. (a) FNA sample with cells at different planes. (b) 3D volumetric dataset. Each z-stack image has some cells in focus while other cells out of focus (c) Heterogeneous plane which intersects with each cell. (d) All non-overlapping cells are in focus in this heterogeneous plane.

## 2.4 Experimental setup and all-in-focus processing workflow

### Experimental setup

Fig.2.8 shows the general process by which we accomplish all in focus FPM imaging. First, the uneven sample is imaged with our FPM system to collect a set of raw data. The data is then processed with the FPM algorithm to generate a stack of images at different focal planes (refocus stack). We then move a small window (vignette) across the image and select the corresponding image segment from the refocus stack that is in the sharpest focus. This selection process is repeated across the entire image and the selected segments are then fused to synthesize an all in focus image.

We implemented a transmission FPM system for this experiment. A CCD camera (ON Semi KAI 29050, 5.5 $\mu$m pixel size) served as our imaging camera. An Adafruit LED array (product ID: 607) was mounted *sim* 66 mm below the focal plane of a 20x/0.40 objective (Plan N, Olympus), resulting in a 1.1 mm diameter field of view. The spacing between adjacent LEDs was 4 mm. During the data acquisition

process, we sequentially illuminated the sample with individual LEDs of the array. Depending on the position of the lit LED, the illumination on the sample would have a specific illumination incidence angle. The transmission light was then collected through the objective and a raw image frame was recorded by the camera. In optical information terms, the collected data contains a sample angular spectrum segment. By collecting raw image frames for each LED in a 15x15 subsection of the LED array, we effectively gather image data that collectively correspond to an effective illumination NA of 0.4 and a total synthetic NA of 0.8. The central wavelengths of the full color LED were 632.3 nm (red), 516.2 nm (green), and 471.2 nm (blue). Average power of red, green and blue LEDs were 1.7 mW, 2.1 mW and 1.6 mW, respectively. Exposure time was set to be 0.5 s for each raw image acquisition. Total acquisition time for one color channel was 9 mins.

The data was then processed with the FPM algorithm. Broadly speaking, the algorithm combines synthetic aperture concept and phase retrieval concept to compute the expected optical wavefront at a chosen plane on the sample. The redundancy in raw image data (partially shared angular spectrum information) allows the FPM algorithm to recover phase information from the raw data that are purely intensity measurements, and subsequently, to generate the complex valued optical wavefront associated with the sample [1, 7, 34].

From a user's perspective, the operation of both raw image acquisition and FPM image processing are straightforward. The raw image acquisition procedure of our all-in-focus FPM set up is the same as that of a traditional transmission microscope: loading sample, finding the region of interest (ROI) and adjusting the focal plane. The raw images under different illumination angles will be captured automatically by the computer. Only a few inputs are required from the user to generate an optimal all-in-focus image: the exact raw images to be processed, the z-scanning range and the z-scanning step size. With these parameters, the user will then get the all-in-focus image by a single click.

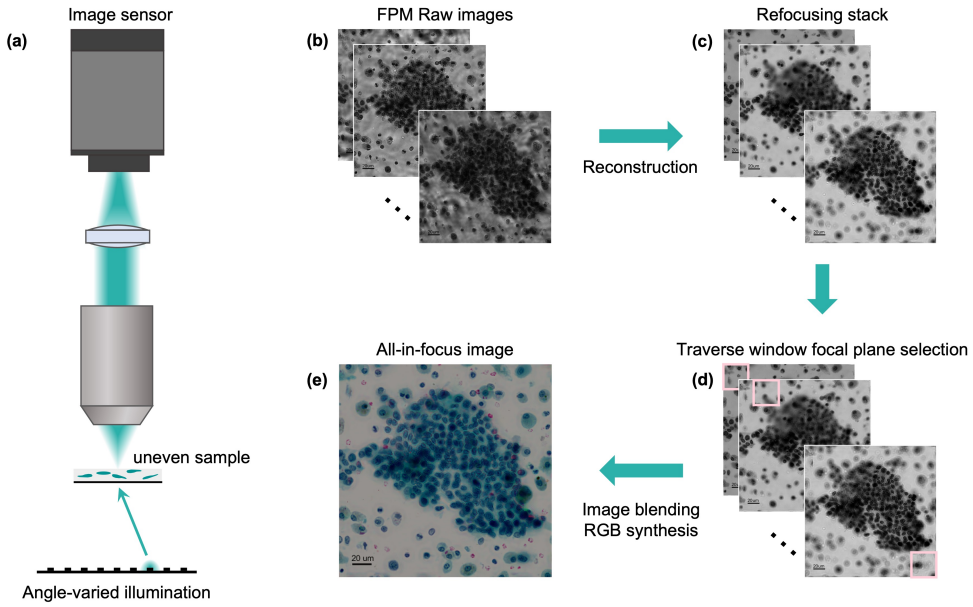


Figure 2.8: General process of all-in-focus FPM. (a) Schematic of FPM set up. (b) Raw data of FPM. (c) Refocusing stack reconstructed from raw data. (d) Focal plane selection for each part. (e) Synthesized all-in-focus color FPM image.

### Digital refocusing by FPM

We accomplished digital refocusing in this experiment by introducing a refocus phase factor to the embedded pupil function recovery (EPRY) algorithm [1, 7] – the component of the FPM algorithm that evaluates the imaging systems pupil function. The refocus phase factor, equivalent to defocus aberration, is given by:

$$exp(\phi_r(z_r)) = exp(i\sqrt{k^2 - u^2 - v^2} \cdot z_r), u^2 + v^2 < k_{max}^2 \tag{2.5}$$

where $z_r$ is refocus distance, "$k = 2\pi/\lambda$" is the wavenumber of the illumination light in vacuum, u, v are 2D coordinates in Fourier domain, and $k_{max} = NA \cdot k$" is the cut off frequency of the objective lens. The flowchart of a single refocusing iteration in a subregion of the sample's Fourier domain is showed in Fig.2.9a. To calculate the image at the plane with distance $-z_r$ from the focal plane, we computationally refocused the sample spectrum acquired by distance $z_r$, which is equivalent to optically propagating the target plane to the true focal plane. We do so by performing the EPRY iteration according to our intensity observation at the focal plane. Finally, we refocused the sample Fourier spectrum by distance $-z_r$, which is equivalent to the optical propagation back to the target defocus plane, and update the sample Fourier spectrum accordingly. In each iteration a reconstruction

error was calculated by getting the summation of each pixel's square error between reconstruction intensity and captured intensity. Adaptive step size strategy was adopted in our algorithm. Step sizes for both spectrum updating and pupil updating began at 0.1 and reduced by one half once the reconstruction error change was less than 5%. We terminated the iteration when the step sizes were less than 0.01.

We used both a USAF target slide (Fig.2.9 b and c) and a thyroid FNA biopsy sample slide (Fig.2.9 d and e) to demonstrate and verify the FPM's digital refocusing ability. A USAF target slide 30 $\mu$m below focal plane illuminated with blue LEDs (471.2 nm) was imaged by our FPM system. The reconstruction results at the original focal plane (Fig.2.9 b) and the exact USAF slide plane (30 $\mu$m below the original focal plane) (Fig.2.9 c) demonstrate the accuracy of FPM refocusing ability.

Then we digitally refocused the FPM data from a thyroid FNA biopsy sample. RGB channels were reconstructed and then synthesized to form color images. Two focal planes, the original focal plane (Fig.2.9 d) and 15 $\mu$m below the original focal plane (Fig.2.9 e) were reconstructed. From the resulting images, we can clearly see that the cells in the sample reside in multiple focal planes—neither of the focal planes in Fig.2.9 d and Fig.2.9 e was able to place all the cells in focus simultaneously.

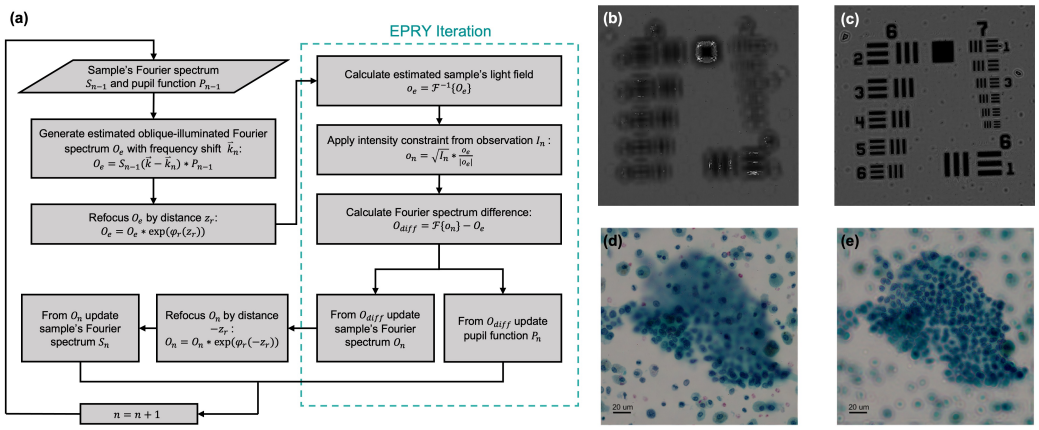


Figure 2.9: Digital refocusing ability of FPM. (a) Flowchart of FPM EPRY digital refocusing. (b) Reconstruction of USAF target at original focal plane. (c) Reconstruction of USAF target at 30 $\mu$m below the original focal plane. (d) Reconstruction of the sample at the original focal plane. (e) Reconstruction of the sample at 15 $\mu$m below the original focal plane.

**Focus Evaluation Metric**

To select image segments that are in focus, so that we can synthesis all in focus images, we next utilized normalized variance (NV) [36, 37] as a focus evaluation metric to select the sharpest image segments from a refocused image stack. As an image contrast based function, normalized variance is less sensitive to both noise and changes in brightness. Normalized variance of a selected part of image, denoted as NV, is given by:

$$NV = \frac{1}{W \cdot H \cdot \mu} \sum Wx = 1 \sum Hy = 1 (I(x, y) - \mu)^2 \tag{2.6}$$

where $W$ and $H$ are the width and height (unit: pixel) of the image, $I(x, y)$ is the value of each pixel in the image and $\mu$ is the mean value of all pixels.

We examined the effectiveness of NV in selecting the correct focal plane for biological samples (Fig.2.10 a and b). A sample was placed at the objective's focal plane and imaged with green illumination (516.2 nm). Refocus stack ranging from 20 to 10 $\mu$m was created by FPM digital refocusing. Given the uneven nature of the thyroid sample, only a 13.75x13.75 $\mu$m2 (100 px x 100 px) region which can be regard as a flat layer was cropped. The NV curve with respect to refocusing distance is plotted in Fig.2.10 a. Corresponding images, respectively, at 5, 2.5, 0, 2.5, 5, 7.5 $\mu$m away from NV peak plane are showed in Fig.2.10 b. The sharpest image appears at the NV peak plane (Fig.2.10 b3). As image plane shifts away from the NV peak plane, the image becomes progressively more blurred and NV value drops correspondingly.

Then we generated depth maps of the sample by applying NV function to all RGB refocusing FPM stacks of the thyroid sample. The refocus range is from 20 $\mu$m to 10 $\mu$m. Results are showed in Fig.2.10 c and d. The depth map quantitively shows the height variance at different part of the sample. Fig.2.10 d is the exact defocus depth at dash lined position denoted in Fig.2.10 c, representing RGB channels, respectively. The height variance in RGB channels track each other and the residual variations can be attributed to the chromatic aberration of the objective. By separately selecting the correct focal plane for each channel, we can then synthesize a chromatic aberration free image.

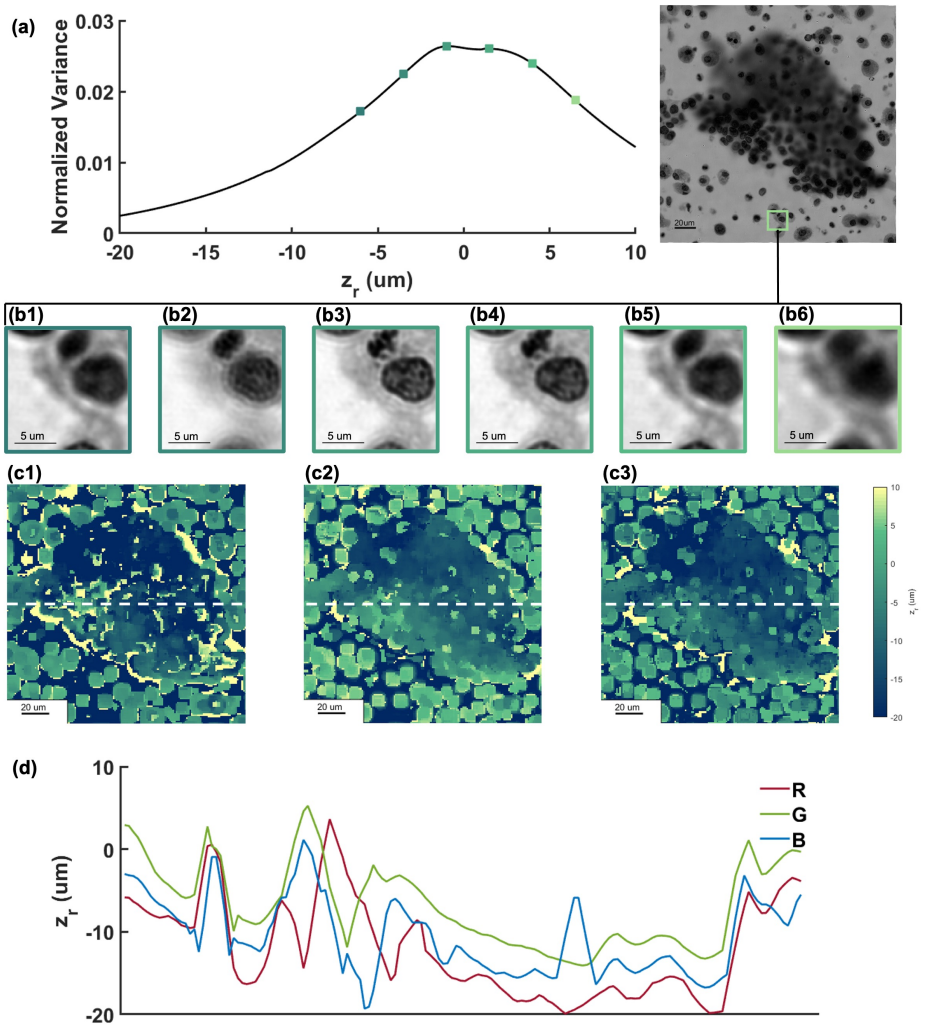


Figure 2.10: Normal variance as a focus evaluation metric. (a) NV curve of a small region of a sample. (b) Corresponding images at selected points in (a) (-5, -2.5, 0, 2.5, 5, 7.5·$\mu$m away from NV peak plane, NV peak value at b3). Scale bar: 5·$\mu$m. (c) Depth maps of a sample. c1. Red channel. c2. Green channel. c3. Blue channel. (d) RGB depth profiles at dash-lined position in (c).

### Synthesizing an all in focus image

Fig.2.11 summarizes the synthesis process. We shift a vignette across the entire image. At each location, the algorithm calculates the NV of the image within the vignette and selects the frame with the maximum NV as the in focus image segment to be used. To reduce seam and mosaic, we set the traverse step size to be smaller

than the vignette side length, resulting in neighbouring segments overlapping each other. At each location, the average across the segments is used as our final all in focus output. In our experiment, the vignette size was 100 x 100 px2 and traverse step size is 1/10 of the vignette side length. Color images are generated by repeating this process for the red, green and blue channels.

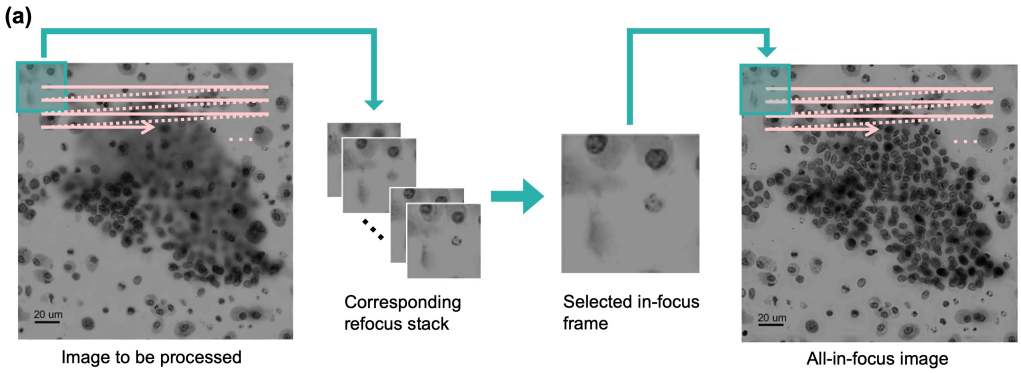


Figure 2.11: Synthesizing an all-in-focus image. (a) Synthesis procedure. Green channel images are demonstrated. A vignette is shifted across the entire image. In focus segment at each location was selected by applying the normal variance function. All segments were then fused together to render an all-in-focus image.

## 2.5 Results and evaluation of the reported all-in-focus method

Fig.2.12 shows the comparison of an image from a single focal plane (Fig.2.12 a) compared to an FPM all in focus image (Fig.2.12 b) on a diagnostic cell cluster in an FNA cytology preparation from a thyroid nodule. As described more fully in the figure legend, it can be easily seen that the FPM all in focus image allows for the precise morphologic evaluation of effectively all the cells in this diagnostic cluster, despite the thickness (and thus multiple focal planes) of the cluster.

We note that this all in focus FPM method only works for cells that do not overlap with other cells. In locations where cells overlap, the algorithm will still attempt to tune the effective focal plane. This will generally put a single cell in focus, but there is no guarantee it will converge correctly.

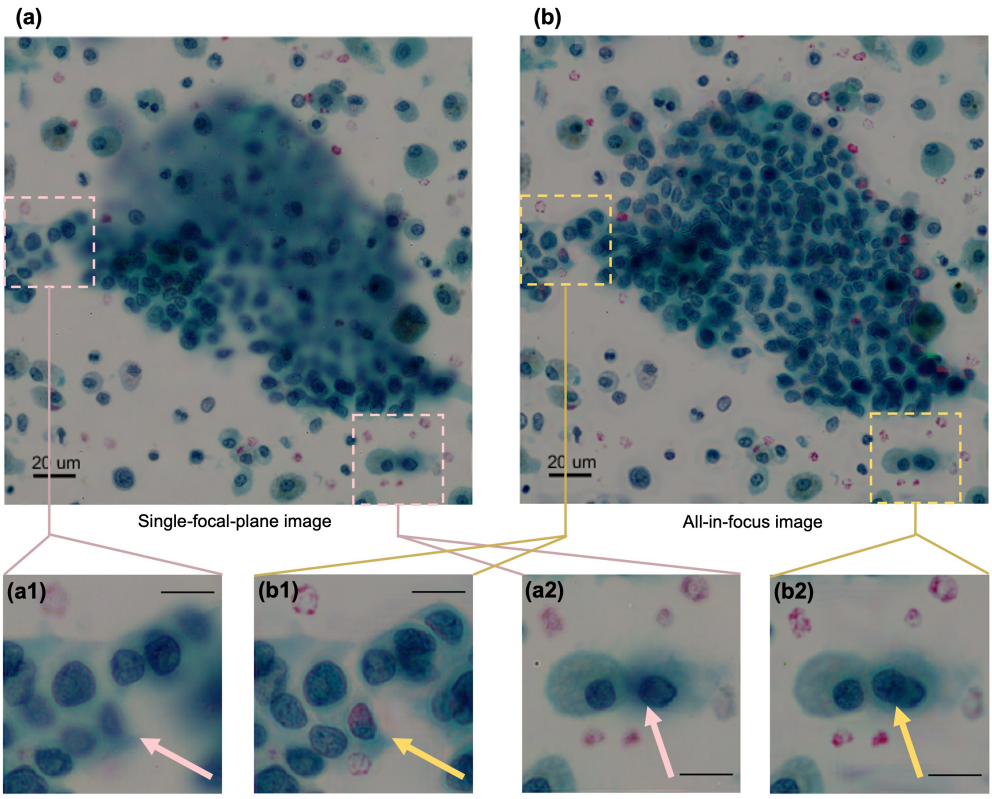


Figure 2.12: Comparison between a single plane of focus image with an all-in-focus FPM image. (a) Single-focal-plane color image reconstructed from FPM. Note the large areas of out of focus image in the diagnostic cluster that results from the thickness of the preparation (b) All-in-focus color image reconstructed from FPM. Note that all non-overlapping cells in the diagnostic cluster can be seen in sharp focus, despite the thickness of the preparation. (a1,2) Corresponding details boxed out from single-focal-plane image (a). Note the out of focus cell in a1 (yellow arrow). In a2, the pink arrow points to an apparently in focus cell. Scale bar: 20·$\mu$m (b1,2) Corresponding details boxed out from all-in-focus image (b). Note that the out of focus cells in a1 can now be seen in sharp focus, with a diagnostic cell nucleus now clearly seen (yellow arrow, b1). In b2, note that the apparently in focus cell seen in a2 can now be seen to actually represent 2 cells (yellow arrow, b2). Scale bar: 20 $\mu$m.

A Papanicolaou-stained thyroid FNA biopsy slide was then separately scanned using the FPM system and an Aperio system AT2 digital pathology scanner to compare the performance of each imaging modality.

The Aperio scanner was equipped with an objective lens with NA of 0.75. In order to match the resolution between the Aperio scanner and our FPM system, we

switched our FPM objective to a 0.75 NA objective and adjusted the illumination array to provide a maximum of 0.75 NA illumination. This larger NA illumination was achieved by setting the distance between the LED array and the objective focal plane to ~25 mm. The number of raw FPM images acquired here is 49. The FPM's resolution dependency on NA differs from that of standard microscopy, the design choices described here were made to ensure that we had comparable resolution for the two systems. Interested readers are invited to read the Supplementary Information document for more information. Results of one ROI is presented in the following section. Additional five results were provided in the Supplementary document.

The acquired images from both the FPM system (Fig.2.13 a, c and e) and the Aperio (Fig.2.13 b and d) are presented. Cells that are in focus (Fig.2.13 d1 and d2) and out of focus (Fig.2.13 d3, d4 and d5) in the Aperio image are simultaneously in focus in the FPM image (Fig.2.13 e). Comparatively, we can also observe that the nuclear details are much clearer with the all in focus FPM images (Fig.2.13 e) when compared to the images from the Aperio scanner (Fig.2.13 d). Not only are more cells in focus for the all in focus images, the amount of cellular details is also greater. The sharper image quality of the FPM images compared to the Aperio images seems at odds with the fact that both systems were set up to have the same NA. This mismatch has also been previously observed in other high resolution FPM experiments [18] as well, and is attributable to the fact that residual presence of aberrations in commercial microscope objectives tend to degrade their achievable resolution and prevent these objectives from attaining NA limited resolutions. In FPM imaging systems, these residual aberrations are readily corrected through the use of the component EPRY sub routine in the FPM algorithm that is able to determine and correct pupil aberrations computationally [1, 7, 33]. For completeness, we characterized the observed resolution for both systems and reported our findings in the Supplementary Information document.

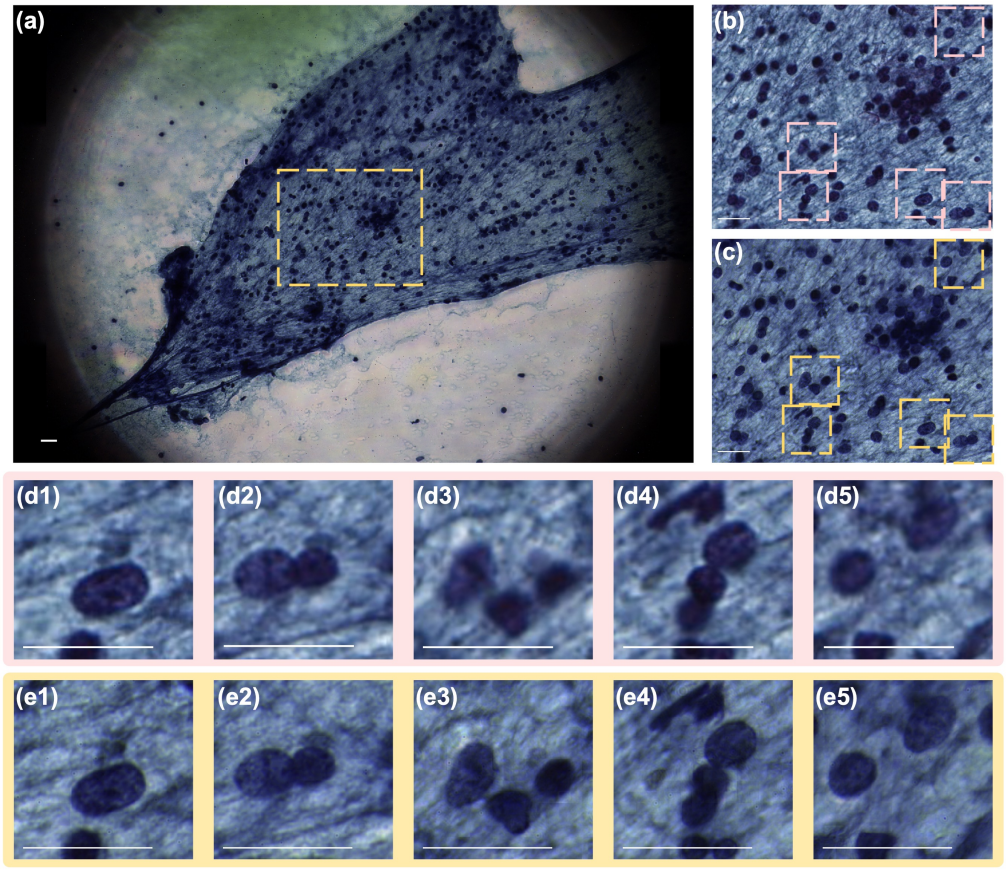


Figure 2.13: Comparison between all-in-focus FPM and Aperio scanner. (a) All-in-focus, whole FoV, color FPM image of a thyroid FNA biopsy sample. (b) Aperio scanner result of the boxed-out region in (a). (c) FPM result of the boxed-out region in (a). (d) Corresponding details boxed-out from Aperio result (b). (e) Corresponding details boxed-out from FPM result (c). Scale bar: 20·$\mu$m. Yellow annotated figures: all-in-focus FPM results. Pink annotated figures: Aperio scanner results.

## 2.6 Advantages of the all-in-focus FPM and potential further applications

We developed a method that enables all in focus FPM imaging of FNA biopsy slides. The all in focus imaging ability is realized by incorporating digital refocusing and focus evaluation into the original FPM image rendering process. In addition to inheriting original FPM's advantage of wide field and high resolution, all in focus FPM further frees user from the constraints of shallow depth of field in high NA high resolution microscopy. For color imaging, RGB channels are first processed individually and then synthesized to form an RGB all in focus image. Chromatic aberration associated defocus can thus be corrected through this procedure.

From a pathology perspective, the all in focus image is able to bring the vast majority of the cells on a slide into focus without sacrificing cellular detail. Cytopathologists use multiple different components of cellular detail to aid in making a diagnosis. These include the amount and the character of the cytoplasm, the contours of the nuclear membrane, the texture of the chromatin and the presence or the absence of nucleoli among others. For successful evaluation of a slide, all of these different components need to be in focus and well visualized. As Fig.2.12 illustrates, an all in focus image brings the vast majority of cells into focus when compared to a single focal plane image. The cellular and the nuclear detail is clearly appreciable in nearly all cells of the all in focus image compared to the single focal plane image where some cells remain blurred and cannot be evaluated. The superiority of the all in focus can also be appreciated in Fig.2.13, comparing images acquired by conventional scanning (Aperio) vs. the FPM imaging system. Once again, not only are almost all of the cells in focus, but they are in focus at high power, preserving diagnostic architectural, cellular and nuclear details. The all in focus images are both more efficient in that more cells can be visualized without the need to focus or scan through multiple focal planes and they provide greater cellular detail which the pathologist needs to make diagnoses.

In principle, our all in focus algorithm can also be applied to conventionally acquired z stack images from a standard scanner. However, there are several distinct advantages associated with using FPM data. First, FPM can acquire the requisite raw data to cover the same effective z range without requiring the use of any mechanical actuation along the z axis—thereby significantly simplifying the scan system. Second, commercial z stack images are discretized along the z axis as determined by the z step size, while FPM is free from such conceptual limitations. For a commercial scanner, the finer the z step size, the longer the scan duration will be and the larger the final data size will be. This trade off necessarily constrains all z stack imaging processes in commercial scanners. Interestingly, such trade off does not exist for FPM. As long as the FPM is able to collect a raw image data set that allows the 2D wavefront to be accurately determined, that data can be used to virtually generate z stack images with arbitrarily fine z step size. From an information viewpoint, the relative efficiency of the FPM raw data set versus the conventional scanner z stack image set is attributable to the fact that there is simply a lot of redundancies within adjacent commercial z stack images.

The all in focus FPM final image is a 2D dataset. In contrast, the conventional

scanner z stack is intrinsically 3D in nature. This means that the all in focus FPM data set is compact in comparison. The compact data size of all in focus FPM images is a broadly useful advantage. In remote digital pathology applications, the smaller and more efficient data file size will greatly facilitate ease of data transmission. The comparatively smaller data file size also makes it easier to feed data into machine learning systems where the number of input nodes is always finite and limited.

The use of FPM to digitally refocus microscope slide images has previously been reported for a number of different applications [1, 15, 38, 39]. Results in neuronal cells [15] demonstrated that FPM images can be digitally refocused over a range of at least $\pm 100$ $\mu$m with a synthetic NA of 0.42. In addition to light field refocusing, a new multi slice refocusing algorithm was also proposed and 100 $\mu$m thick with 10 $\mu$m step spirogyra algae stack was reconstructed with a synthetic NA of 0.66 [25]. However, much of these prior works dealt with adjusting the global focus of the images, and thus cannot be directly applied to address the issue of heterogenous focal planes associated with FNA samples. To date, all in focus FPM imaging has only been developed and applied to blood smears [39]. In that work, the segmentation based method relied on prior knowledge of the morphology of both blood cells and plasmodium parasite, which limits its application and is not a good fit with FNA samples. Our work shows that FPM can be used to create all in focus images of aggregates of cells on an FNA slide without restrictive assumptions or known priors.

Slides from FNA specimens were chosen for this project because of the inherent challenges they present by their need to capture multiple focal planes. However, it should be noted that histologic sections are never completely flat, and high power imaging and image acquisition often results in large patchy out of focus areas. Therefore, FPM is likely to have applications in remote diagnosis and image analysis applications for slides prepared from surgical pathology specimens (biopsies and resections) as well.

Looking to the future, we note that the set up reported here was not optimized for high throughput pathology slides scanning. We expect that a high throughput whole slide all in focus FPM is achievable by using higher power light sources, a high speed and high pixel count camera, and other physical improvements to the system. Such a method can potentially facilitate better and faster pathology analysis of FNA biopsy samples.

It is also worth noting that the FPM system may have even more general applications. When scanned at high power, even “flat” thin sections in histologic slides show

significant focal plane variation, hindering rapid imaging, and creating significant pitfalls for using these images in advanced applications, such as deep learning/AI, where out of focus areas are believed to be a major impediment to AI/deep learning on these preparations [40]. The all in focus FPM method may be an ideal solution to this problem. Machine learning methods generally outright reject out of focus areas from consideration, and this can lead to significantly reduced analysis coverage and accuracy. As this all in focus FPM method can ensure that the entire image is in focus, and therefore, it has the potential to greatly improve the performance of cell segmentation and recognition machine learning methods. In computer vision field, all in focus FPM images can also provide sharp edges which can greatly facilitate edge detection based segmentation methods. Broadly speaking, the rendering of all in focus pathology images has the high potential to solve a key challenge associated with machine learning based digital pathology analysis – the challenge that out of focus image segments are ill suited for machine learning processing.

## 2.7 Appendix

### Resolution quantification for simulated high-NA FPM and standard transmission microscope

We simulated Siemens star images from both high-NA FPM and standard transmission microscope. Parameters used in simulation were the same as experimental set-up, with objective lens NA of 0.95, maximum illumination of 0.95, objective lens magnification of 50x and camera pixel size of 6.5 $\mu$m x 6.5 $\mu$m.

We simulated high-NA FPM modality by first generating raw data from simulated coherent imaging and then performing reconstruction with the FPM rendering algorithm used in the experiments. For each oblique-illuminated raw data, the object field was directly Fourier transformed to get the Fourier spectrum and then applied to spatial-shifted coherent transfer function (CTF) with objective NA of 0.95. The shift vector was determined by the illumination angle. Then an inverse Fourier transform was performed to convert the Fourier spectrum back to the image field. The final image was generated by modulus squaring the image field and then sampling by the camera sensor array. The FPM rendering from simulated raw data is shown in Fig. S1(a1).

For standard transmission microscope, which is an incoherent imaging modality, the object field was modulus squared and Fourier transformed to generate the Fourier spectrum of the object intensity. Then the optical transfer function (OTF) with

objective NA of 0.95 was applied to the object intensity Fourier spectrum. The final image was generated by inverse Fourier transforming the modulated frequency spectrum followed by sampling with the camera sensor array, which was showed in Fig.2.14(b1). We adopted Sparrow's criterion and full pitch resolution when claiming resolution for both systems. Under such criterion the resolution is defined as the minimum periodicity where every spoke of the Siemens target can be resolved. From simulation the simulated resolution of high-NA FPM and standard transmission microscope are separately 245 nm and 278 nm. Simulated Siemens star images from both systems and intensity plot along minimum circles are shown in Fig.2.14(a2) and Fig.2.14(b2).

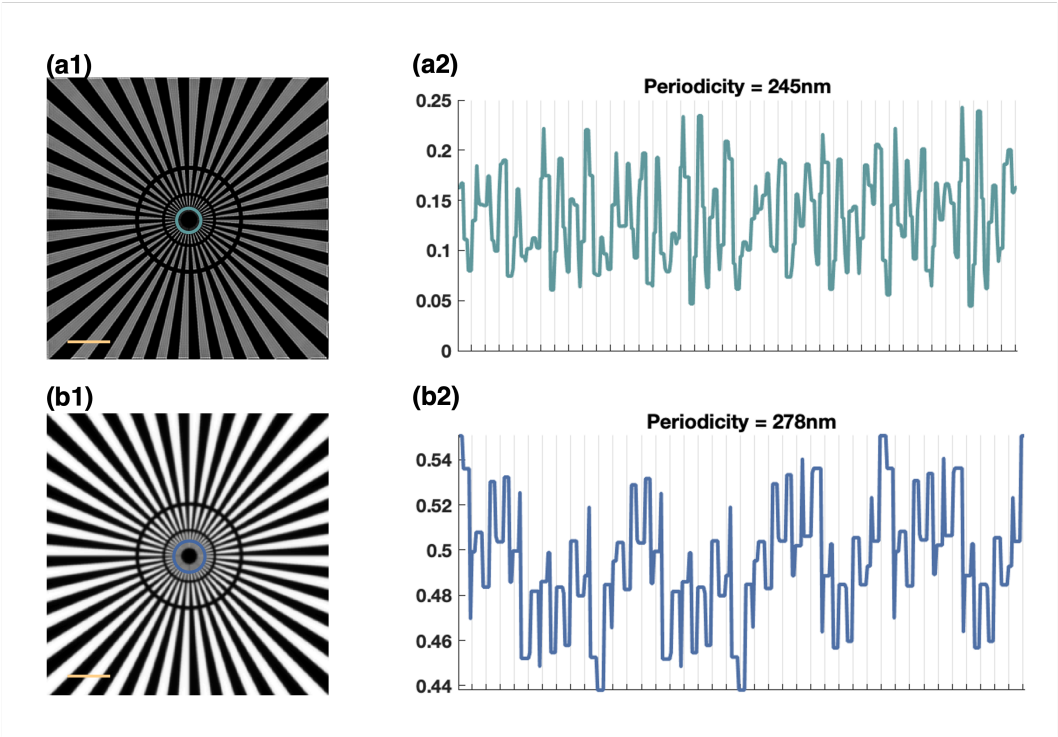


Figure 2.14: Simulated Siemens star imaging and resolution quantification. (a) Siemens star imaged by simulated high-NA FPM (a1) and intensity plots along the minimum resolvable circle (a2). (b) Siemens star imaged by simulated standard transmission microscope (b1) and intensity plots along the minimum resolvable circle (b2). Scale bar: 5 $\mu$m.

**Imaging results of bone marrow smear sample**

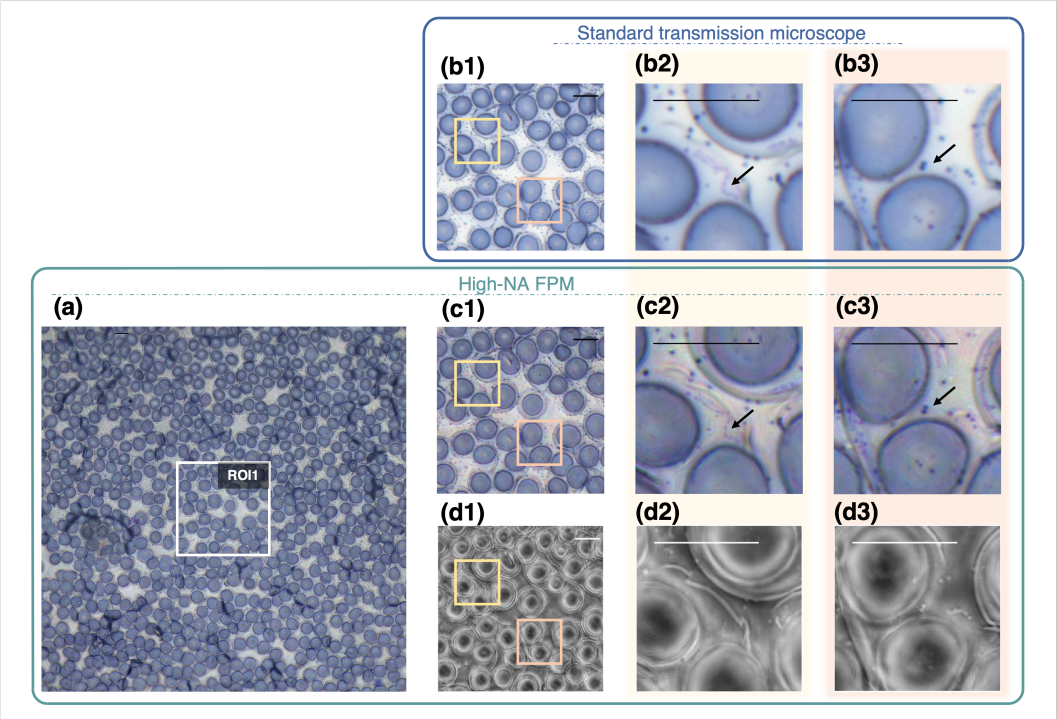


Figure 2.15: Bone marrow sample imaging by high-NA FPM and standard transmission microscope. (a) Whole-frame color high-NA FPM bone marrow smear image. (b) Color image and enlarged details of the region of interest (ROI) 1 from standard transmission microscope. (c) Color image and enlarged details of the ROI 1 from high-NA FPM. (d) Phase image reconstructed from blue channel and enlarged details of ROI 1. Scale bar: 10 $\mu$m.

**Resolution quantification for high-NA FPM and standard transmission microscope under defocus condition**

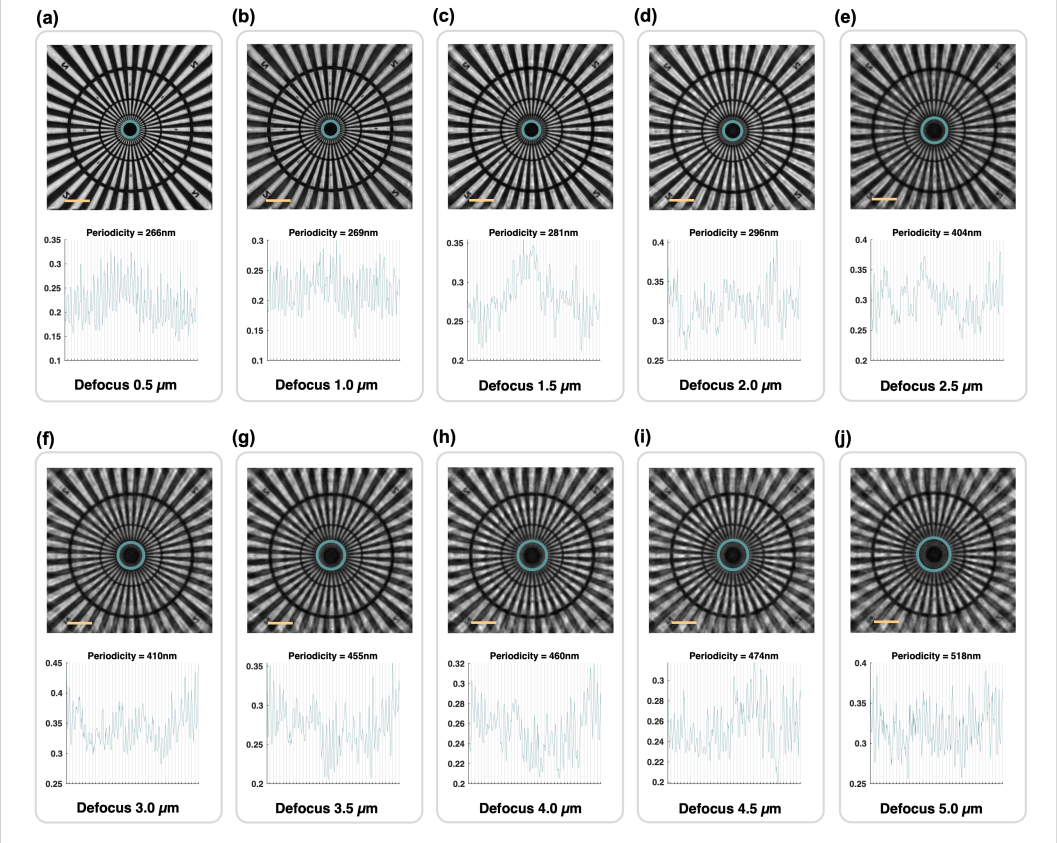


Figure 2.16: Resolution quantification for high-NA FPM under defocus condition. Both high-NA FPM with digital refocusing images and intensity plots along the minimum resolvable circle are provided. Scale bar: 5 $\mu$m.

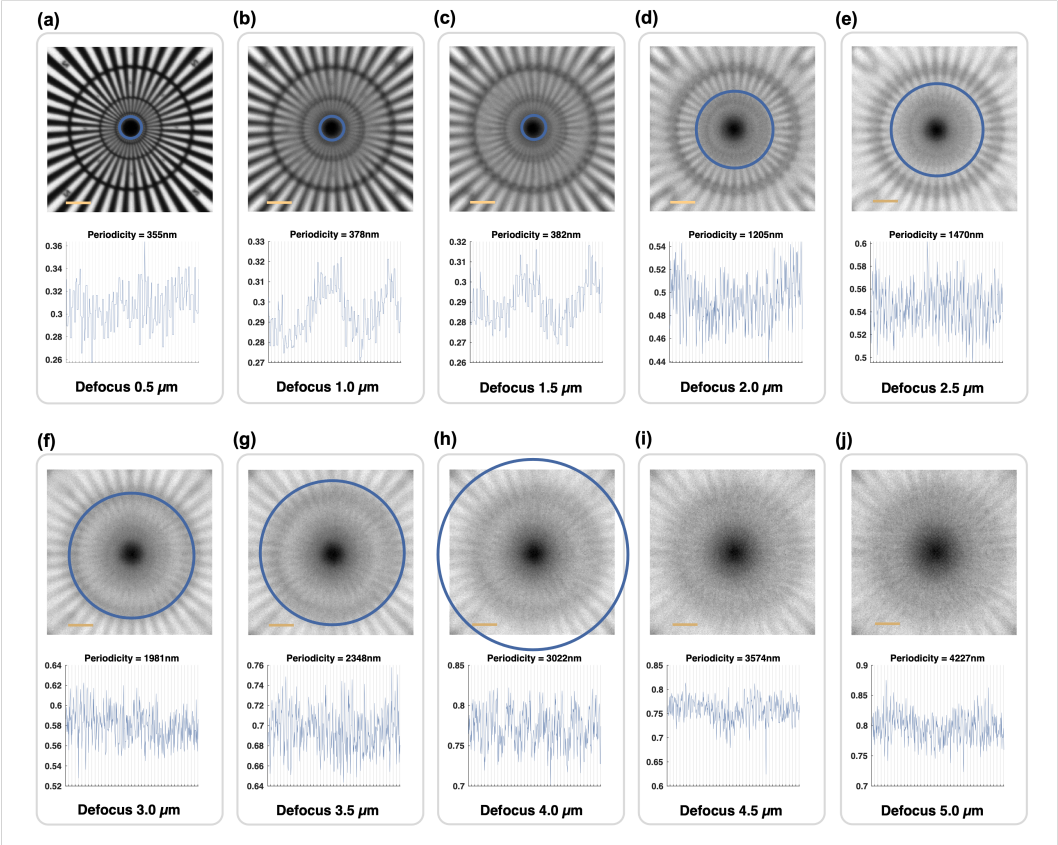


Figure 2.17: Resolution quantification for standard transmission microscope under defocus condition. Both standard transmission microscope images and intensity plots the along minimum resolvable circle are provided. Minimum resolvable rings became so large that they fall out of demonstrated Siemens star images when defocused for 4.5 $\mu$m (i) and 5 $\mu$m (j). Scale bar: 5 $\mu$m.

**FPM illumination scheme for pupil size matching between FPM and Aperio scanner**

The Aperio scanner is an incoherent imaging system. For our experiments, we configured the scanner to perform imaging with a 0.75 NA objective under Kohler illumination. The FPM is a coherent imaging system. From Fourier optics' perspective, the pupil diameter of an incoherent imaging system is twice as much as that of a coherent imaging system under the same numerical aperture. The pupil diameter determines the cutoff spatial frequency of an imaging system and thus have an influence on the resolution of the system. For our comparison experiments, we would like to compare the performance of the two systems with the same pupil size, which is equivalent to the same cutoff spatial frequency. As such, to match Aperio's scanner theoretical resolution, we need to adjust the FPM system's synthetic NA, so

that it is equal to 2x0.75 NA, resulting in 1.5 NA. We accomplished this by using a 0.75 NA objective in the FPM system and an illumination geometry that provides an illumination NA of 0.75.

The information coverage in Fourier space is showed in Fig.2.18(a). Each yellow spot denotes the angular position of a single LED in the illumination array. The blue circle circumscribes the information associated with the raw image data collected with the LED whose position is denoted by the yellow spot in the center of the blue circle. The diameter of this circle is directly proportional to the objective's NA. The red circle circumscribes the total information associated with the complete set of raw data. In this figure, it can be interpreted as the sum of all the blue circles for all the LEDs. The diameter of this circle is directly proportional to the system's synthetic NA. In our experiments, we used 49 LEDs for illumination. By choosing the LED angular position appropriately, we can achieve an effective system's synthetic NA of 1.5. We used a USAF target as a resolution claimer in our experiment. A simulation was performed to determine the theoretical resolution values for both Aperio scanner and all in focus FPM, where no aberrations appeared. For Aperio scanner, the object field was modulus squared and Fourier transformed to generate the frequency spectrum of the object intensity. Then the optical transfer function (OTF) was applied to the object intensity frequency spectrum. The final image was generated by inverse Fourier transforming the modulated frequency spectrum and then sampling by image sensor array. For FPM, the object field was directly Fourier transformed to get the frequency spectrum of the object field. The coherent transfer function (CTF) was applied to the object field frequency spectrum. Then an inverse Fourier transform was performed to convert the frequency spectrum back to image field. The final image was generated by modulus squaring the image field and then sampling by image sensor array. We adopted Sparrow's criterion and full pitch resolution when claiming resolution for both systems. Under such criterion the resolution was defined as the minimum distance between two bars where every bar of the USAF target can be resolved. From simulation the theoretical resolution of the Aperio scanner and our FPM system are separately 344 nm and 288 nm. Simulated images under such conditions for both systems are demonstrated on Fig.2.18(b) and (c).

Then a USAF target was imaged to examine the actual resolution of both systems. The USAF was illuminated under green illumination (516.2nm). From the simulation above, FPM system should be able to recognize Group 11 element 5. The

imaging results are showed in Fig.2.18(d). Group 11 element 4 was able to be recognized but Group 11 element 5 was not, indicating the full pitch resolution to be a value between 308 nm and 345 nm. In our experiment we chose to underestimate rather than overestimating the resolution of both systems, thus the resolution of FPM was 345 nm, 1 element (20%) deviated from simulation value of 288nm.

The resolution of Aperio scanner was also examined and the green channel results were reported here for comparison, which is showed in Fig.2.18(e). According to the simulation above, Group 11 element 4 should be resolved by Aperio scanner. However, only group 10 element 4 was fully resolved. This indicates that the full pitch resolution of Aperio scanner was 690nm, 1 whole group deviating from the simulation value of 344 nm.

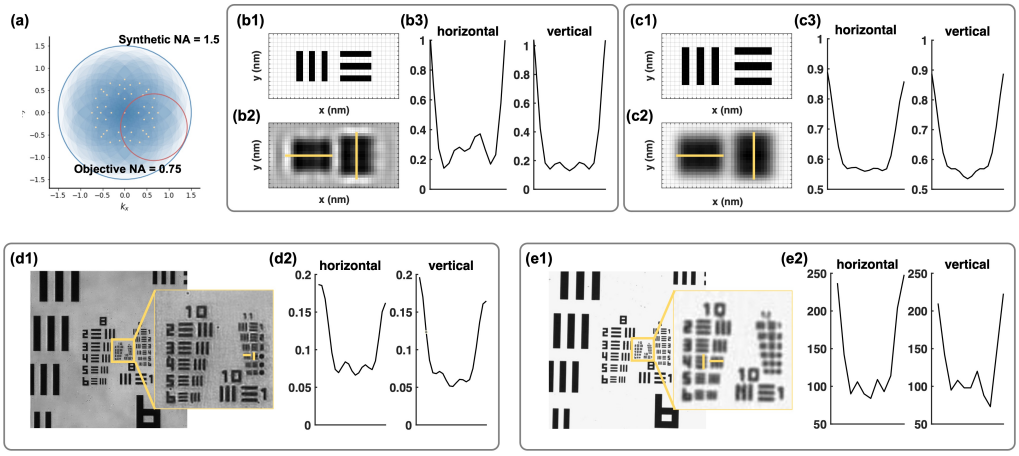


Figure 2.18: Matching FPM pupil size with Aperio scanner. (a) Illumination scheme. Objective NA: 0.75. Synthetic NA: 1.5. Yellow points: illumination angles in Fourier space. (b) USAF target simulating result of FPM system. (b1) Minimum USAF structure that can be resolved by FPM (b2) Simulated FPM imaging of (b1). (b3) Line scan profiles from yellow lines in (b2). Grid size: 100 nm. (c) USAF target simulating result of Aperio scanner. (c1) Minimum USAF structure that can be resolved by Aperio scanner. (c2) Simulated Aperio scanner imaging of (c1). (c3) Line scan profiles from yellow lines in (c2). Grid size: 100 nm. (d) USAF target result from FPM. (d1) Image and enlarged details of USAF target imaged by FPM. (d2) Line scan profiles from yellow lines in (d1). (e) USAF target result from Aperio scanner. (e1) Image and enlarged details of USAF target imaged by Aperio scanner. (e2) Line scan profiles from yellow lines in (e1).

**Supplementary all-in-focus FPM results (20x objective)**

Two additional all-in-focus FPM images of Papanicolaou stained thyroid FNA biopsy slides were provided together with images from the Aperio scanner as comparison (Fig.2.19-Fig.2.20).

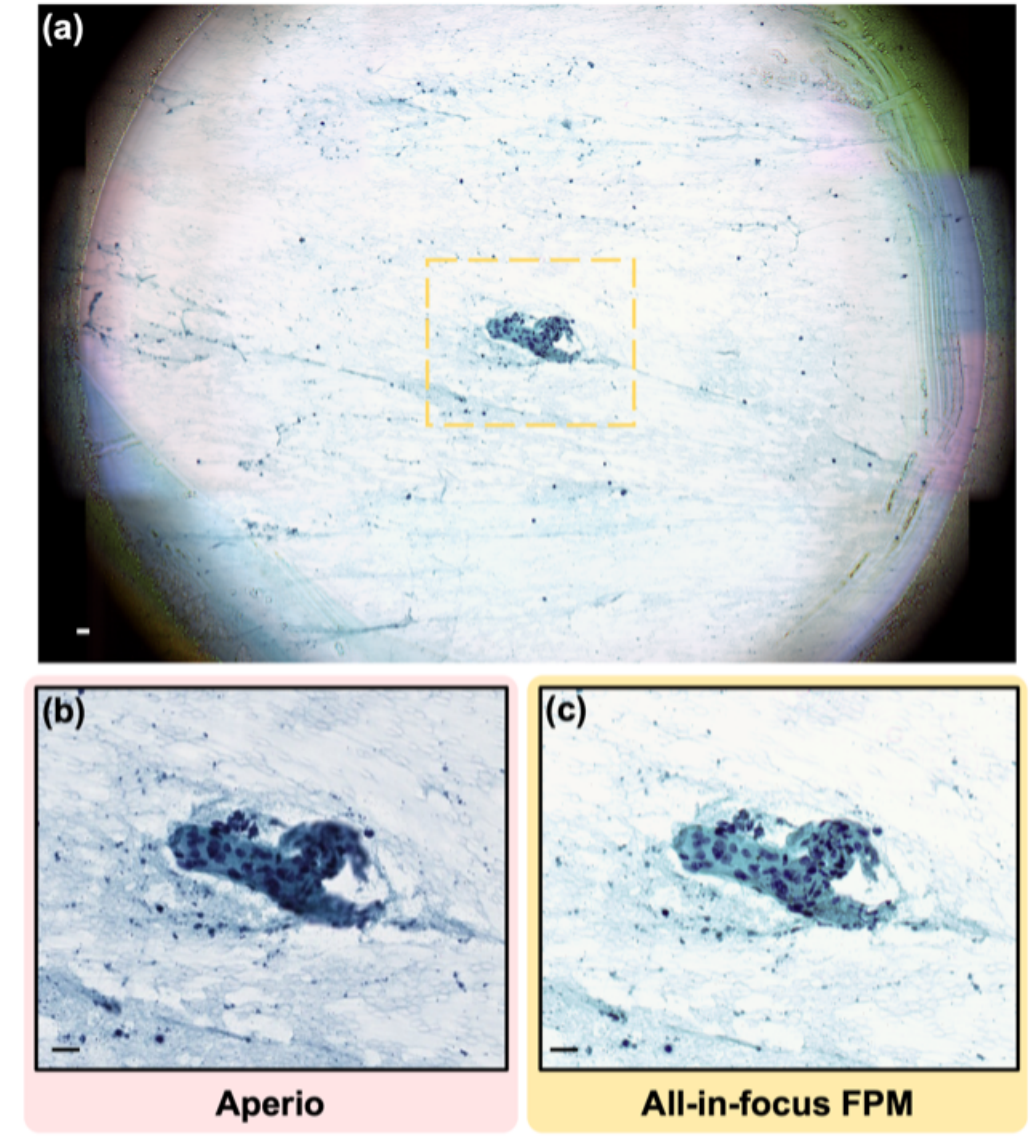


Figure 2.19: Additional Comparison between all in focus FPM and Aperio scanner under 20x (0.4NA) objective (I). (a) All in focus, whole FoV, color FPM image of a thyroid FNA biopsy sample. (b) Aperio scanner result of the boxed out region in (a). (c) FPM result of the boxed out region in (a). Scale bar: 20 $\mu$m. Yellow annotated figures: all in focus FPM results. Pink annotated figures: Aperio scanner results.

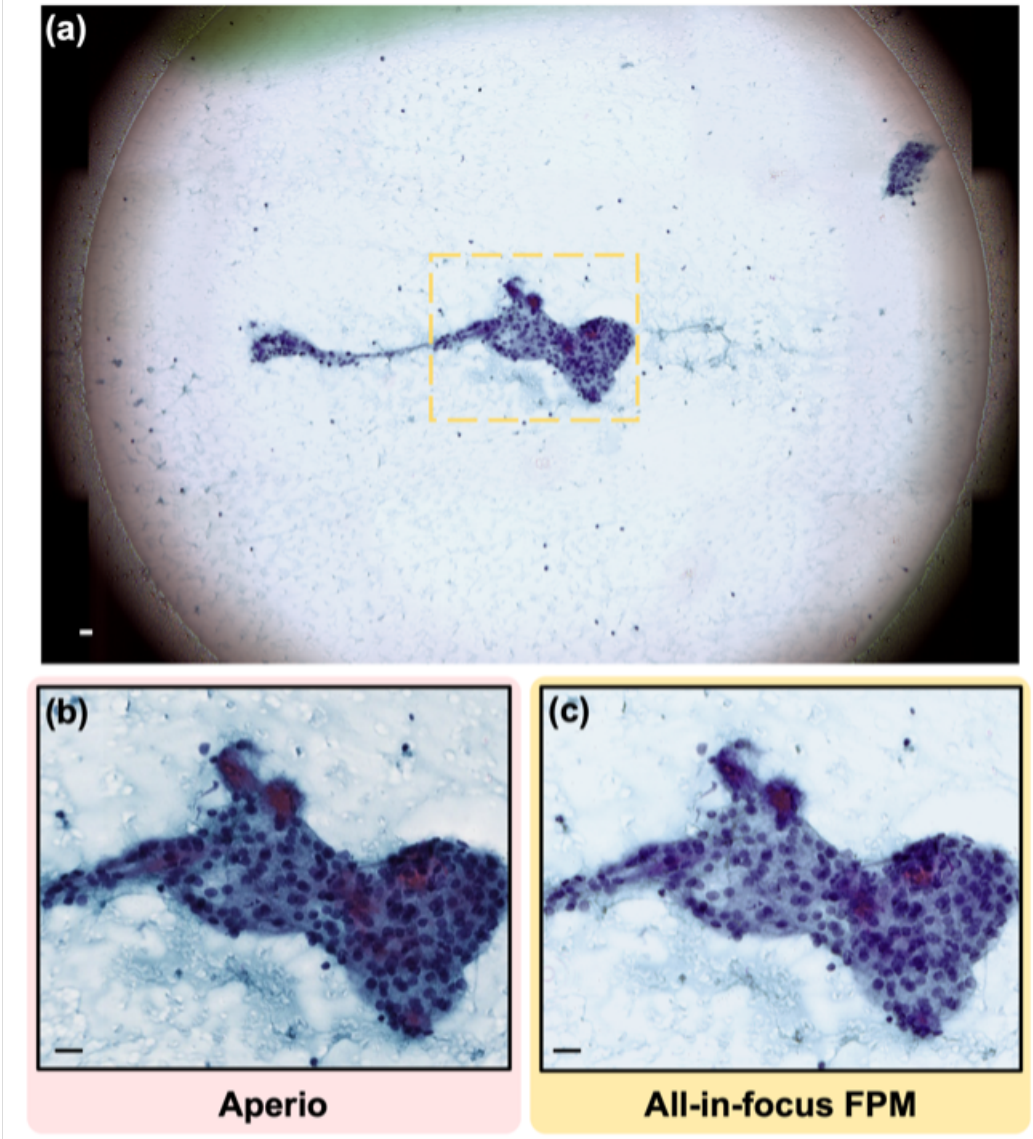


Figure 2.20: Additional Comparison between all in focus FPM and Aperio scanner under 20x (0.4NA) objective (II). (a) All in focus, whole FoV, color FPM image of a thyroid FNA biopsy sample. (b) Aperio scanner result of the boxed out region in (a). (c) FPM result of the boxed out region in (a). Scale bar: 20 $\mu$m. Yellow annotated figures: all in focus FPM results. Pink annotated figures: Aperio scanner results.

**Supplementary all-in-focus FPM results (40x objective)**

Three additional all-in-focus FPM images of Papanicolaou stained thyroid FNA biopsy slides were provided together with images from the Aperio scanner as comparison (Fig.2.21-Fig.2.23).

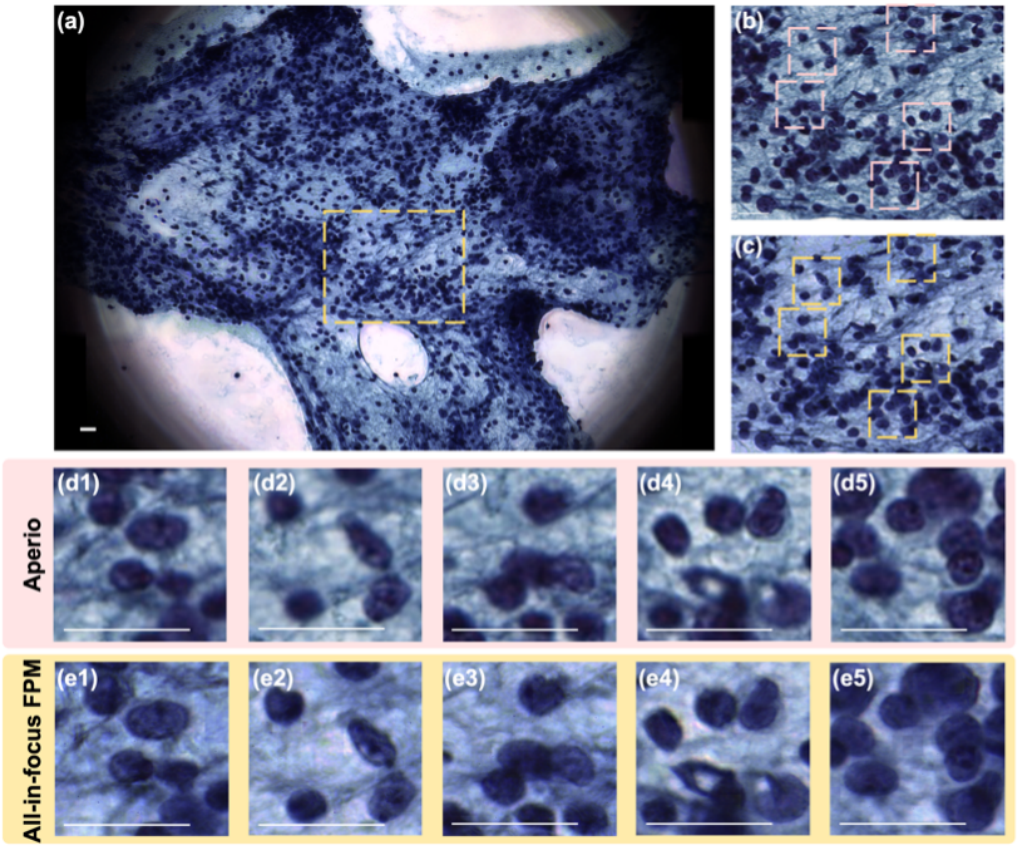


Figure 2.21: Additional Comparison between all in focus FPM and Aperio scanner under 40x (0.75NA) objective (I). (a) All in focus, whole FoV, color FPM image of a thyroid FNA biopsy sample. (b) Aperio scanner result of the boxed out region in (a). (c) FPM result of the boxed out region in (a). (d) Corresponding details boxed out from Aperio result (b). (e) Corresponding details boxed out from FPM result (c). Scale bar: 20 $\mu$m. Yellow annotated figures: all in focus FPM results. Pink annotated figures: Aperio scanner results.

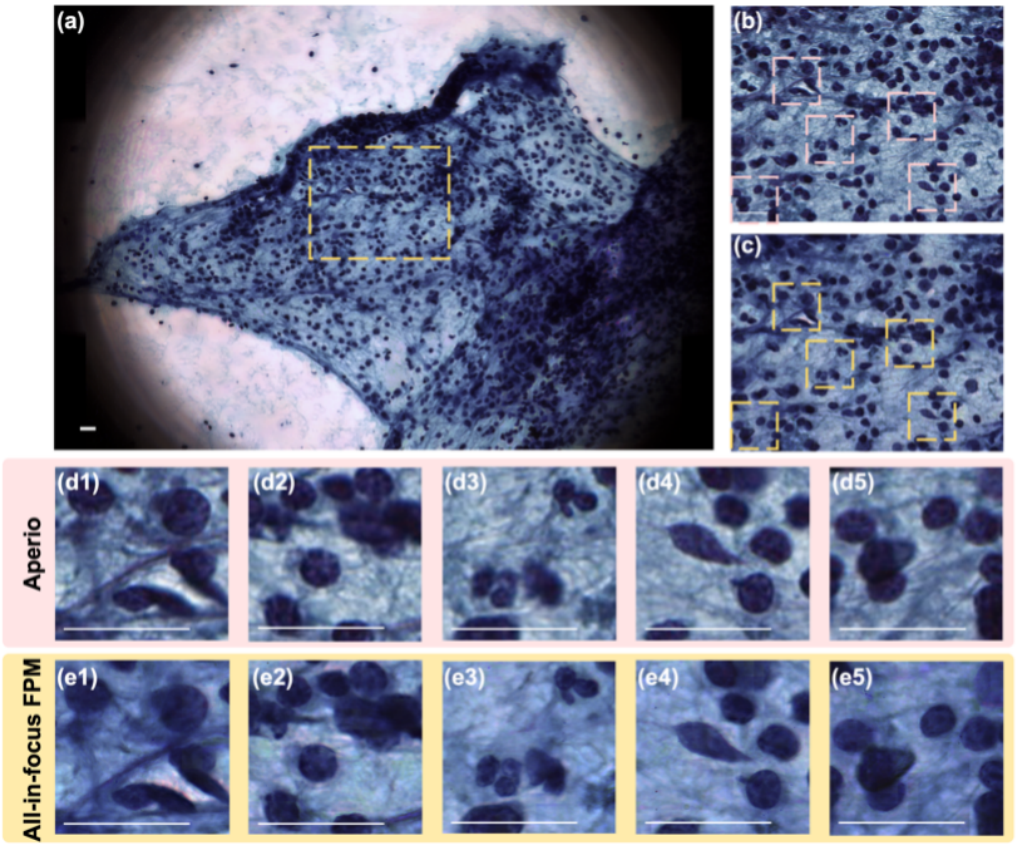


Figure 2.22: Additional Comparison between all in focus FPM and Aperio scanner under 40x (0.75NA) objective (II). (a) All in focus, whole FoV, color FPM image of a thyroid FNA biopsy sample. (b) Aperio scanner result of the boxed out region in (a). (c) FPM result of the boxed out region in (a). (d) Corresponding details boxed out from Aperio result (b). (e) Corresponding details boxed out from FPM result (c). Scale bar: 20 $\mu$m. Yellow annotated figures: all in focus FPM results. Pink annotated figures: Aperio scanner results.

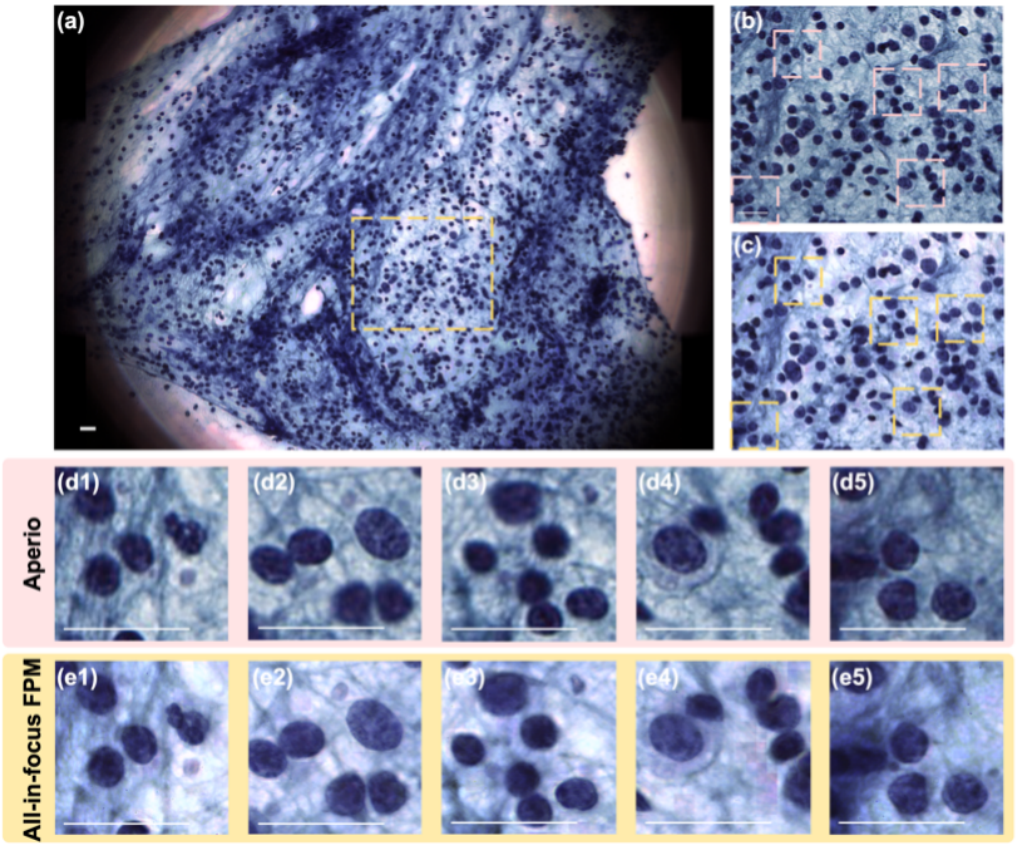


Figure 2.23: Additional Comparison between all in focus FPM and Aperio scanner under 40x (0.75NA) objective (III). (a) All in focus, whole FoV, color FPM image of a thyroid FNA biopsy sample. (b) Aperio scanner result of the boxed out region in (a). (c) FPM result of the boxed out region in (a). (d) Corresponding details boxed out from Aperio result (b). (e) Corresponding details boxed out from FPM result (c). Scale bar: 20 $\mu$m. Yellow annotated figures: all in focus FPM results. Pink annotated figures: Aperio scanner results.

## References


[1] Guoan Zheng, Roarke Horstmeyer, and Changhuei Yang. "Wide-field, high-resolution Fourier ptychographic microscopy." In: *Nature Photonics* 7.9 (2013), pp. 739–745. ISSN: 1749-4893. DOI: 10.1038/nphoton.2013.187. URL: https://doi.org/10.1038/nphoton.2013.187.

[2] Guoan Zheng et al. "Concept, implementations and applications of Fourier ptychography." In: *Nature Reviews Physics* 3.3 (2021), pp. 207–223. ISSN: 2522-5820. DOI: 10.1038/s42254-021-00280-y. URL: https://doi.org/10.1038/s42254-021-00280-y.

[3] James R. Fienup. "Phase retrieval algorithms: A comparison." In: *Applied Optics* 21.15 (1982), pp. 2758–2769.

[4] James R. Fienup. "Reconstruction of a complex-valued object from the modulus of its Fourier transform using a support constraint." In: *Journal of the Optical Society of America A* 4.1 (1987), pp. 118–123. DOI: 10.1364/JOSAA.4.000118. URL: http://opg.optica.org/josaa/abstract.cfm?URI=josaa-4-1-118.

[5] James R. Fienup. "Reconstruction of an object from the modulus of its Fourier transform." In: *Optics Letters* 3.1 (1978), pp. 27–29. DOI: 10.1364/OL.3.000027. URL: http://opg.optica.org/ol/abstract.cfm?URI=ol-3-1-27.

[6] James R. Fienup. "Lensless coherent imaging by phase retrieval with an illumination pattern constraint." In: *Optics Express* 14.2 (2006), pp. 498–508. DOI: 10.1364/OPEX.14.000498. URL: http://opg.optica.org/oe/abstract.cfm?URI=oe-14-2-498.

[7] Xiaoze Ou, Guoan Zheng, and Changhuei Yang. "Embedded pupil function recovery for Fourier ptychographic microscopy." In: *Optics Express* 22.5 (2014), pp. 4960–4972. DOI: 10.1364/OE.22.004960. URL: http://www.opticsexpress.org/abstract.cfm?URI=oe-22-5-4960.

[8] Antony C. S. Chan et al. "Parallel Fourier ptychographic microscopy for high-throughput screening with 96 cameras (96 Eyes)." In: *Scientific Reports* 9.1 (2019), p. 11114. ISSN: 2045-2322. DOI: 10.1038/s41598-019-47146-z. URL: https://doi.org/10.1038/s41598-019-47146-z.

[9] Regina Eckert, Zachary F. Phillips, and Laura Waller. "Efficient illumination angle self-calibration in Fourier ptychography." In: *Applied Optics* 57.19 (2018), pp. 5434–5442. DOI: 10.1364/AO.57.005434. URL: http://ao.osa.org/abstract.cfm?URI=ao-57-19-5434.

[10] Jiasong Sun et al. "Efficient positional misalignment correction method for Fourier ptychographic microscopy." In: *Biomedical Optics Express* 7.4 (2016), pp. 1336–1350. DOI: 10.1364/BOE.7.001336. URL: http://www.osapublishing.org/boe/abstract.cfm?URI=boe-7-4-1336.

[11] Jiasong Sun et al. “Resolution-enhanced Fourier ptychographic microscopy based on high-numerical-aperture illuminations.” In: *Scientific Reports* 7.1 (2017), p. 1187. ISSN: 2045-2322. DOI: 10.1038/s41598-017-01346-7. URL: https://doi.org/10.1038/s41598-017-01346-7.

[12] Florian Ströhl et al. “Object detection neural network improves Fourier ptychography reconstruction.” In: *Optics Express* 28.25 (2020), pp. 37199–37208. DOI: 10.1364/OE.409679. URL: http://www.opticsexpress.org/abstract.cfm?URI=oe-28-25-37199.

[13] Lei Tian et al. “Multiplexed coded illumination for Fourier Ptychography with an LED array microscope.” In: *Biomedical Optics Express* 5.7 (2014), pp. 2376–2389. DOI: 10.1364/BOE.5.002376. URL: http://www.osapublishing.org/boe/abstract.cfm?URI=boe-5-7-2376.

[14] Chao Zuo, Jiasong Sun, and Qian Chen. “Adaptive step-size strategy for noise-robust Fourier ptychographic microscopy.” In: *Optics Express* 24.18 (2016), pp. 20724–20744. DOI: 10.1364/OE.24.020724. URL: http://www.opticsexpress.org/abstract.cfm?URI=oe-24-18-20724.

[15] Jinho Kim et al. “Incubator embedded cell culture imaging system (EmSight) based on Fourier ptychographic microscopy.” In: *Biomedical Optics Express* 7.8 (2016), pp. 3097–3110. DOI: 10.1364/BOE.7.003097. URL: http://www.osapublishing.org/boe/abstract.cfm?URI=boe-7-8-3097.

[16] An Pan et al. “Subwavelength resolution Fourier ptychography with hemispherical digital condensers.” In: *Optics Express* 26.18 (2018), pp. 23119–23131. DOI: 10.1364/OE.26.023119. URL: http://www.opticsexpress.org/abstract.cfm?URI=oe-26-18-23119.

[17] Minglu Sun et al. “Neural network model combined with pupil recovery for Fourier ptychographic microscopy.” In: *Optics Express* 27.17 (2019), pp. 24161–24174. DOI: 10.1364/OE.27.024161. URL: http://www.opticsexpress.org/abstract.cfm?URI=oe-27-17-24161.

[18] Xiaoze Ou et al. “High numerical aperture Fourier ptychography: Principle, implementation and characterization.” In: *Optics Express* 23.3 (2015), pp. 3472–3491. DOI: 10.1364/OE.23.003472. URL: http://www.opticsexpress.org/abstract.cfm?URI=oe-23-3-3472.

[19] Zachary F. Phillips, Regina Eckert, and Laura Waller. “Quasi-dome: A self-calibrated high-NA LED illuminator for Fourier ptychography.” In: *Imaging and Applied Optics 2017 (3D, AIO, COSI, IS, MATH, pcAOP)*. OSA Technical Digest (online). San Francisco, California: Optical Society of America, 2017, IW4E.5. DOI: 10.1364/ISA.2017.IW4E.5. URL: http://www.osapublishing.org/abstract.cfm?URI=ISA-2017-IW4E.5.

[20] Zachary F. Phillips et al. “Design of a domed LED illuminator for high-angle computational illumination.” In: *Imaging and Applied Optics 2015*. OSA Technical Digest (online). Arlington, Virginia: Optical Society of America,

2015, ITh1A.2. DOI: 10.1364/ISA.2015.ITh1A.2. URL: http://www.osapublishing.org/abstract.cfm?URI=ISA-2015-ITh1A.2.

[21] Joseph W. Goodman. "Introduction to Fourier optics. 3rd." In: *Roberts and Company Publishers* (2005).

[22] Shalin B. Mehta and Rudolf Oldenbourg. "Image simulation for biological microscopy: Microlith." In: *Biomedical Optics Express* 5.6 (2014), pp. 1822–1838. DOI: 10.1364/BOE.5.001822. URL: http://opg.optica.org/boe/abstract.cfm?URI=boe-5-6-1822.

[23] Roarke Horstmeyer et al. "Standardizing the resolution claims for coherent microscopy." In: *Nature Photonics* 10.2 (2016), pp. 68–71. ISSN: 1749-4893. DOI: 10.1038/nphoton.2015.279. URL: https://doi.org/10.1038/nphoton.2015.279.

[24] Brian Abbey et al. "Keyhole coherent diffractive imaging." In: *Nature Physics* 4.5 (2008), pp. 394–398. ISSN: 1745-2481. DOI: 10.1038/nphys896. URL: https://doi.org/10.1038/nphys896.

[25] Lei Tian and Laura Waller. "3D intensity and phase imaging from light field measurements in an LED array microscope." In: *Optica* 2.2 (2015), pp. 104–111. DOI: 10.1364/OPTICA.2.000104. URL: http://www.osapublishing.org/optica/abstract.cfm?URI=optica-2-2-104.

[26] Frederick N. Fritsch and Judy Butland. "A method for constructing local monotone piecewise cubic interpolants." In: *SIAM Journal on Scientific and Statistical Computing* 5.2 (1984), pp. 300–304. ISSN: 0196-5204.

[27] Cleve Moler. "Numerical computating with Matlab." In: *Society for Industrial and Applied Mathematics* (2004).

[28] Tilde S. Kline, Lalita P. Joshi, and Hunter S. Neal. "Fine-needle aspiration of the breast: Diagnoses and pitfalls. A review of 3545 cases." In: *Cancer* 44.4 (1979), pp. 1458–1464. ISSN: 0008-543X. DOI: 10.1002/1097-0142(197910)44:4<1458::AID-CNCR2820440440>3.0.CO;2-T. URL: https://doi.org/10.1002/1097-0142(197910)44:4%3C1458::AID-CNCR2820440440%3E3.0.CO%20http://2-t.

[29] Hossein Gharib and John R. Goellner. "Fine-needle aspiration biopsy of the thyroid: An appraisal." In: *Annals of Internal Medicine* 118.4 (1993), pp. 282–289. ISSN: 0003-4819. DOI: 10.7326/0003-4819-118-4-199302150-00007. URL: https://doi.org/10.7326/0003-4819-118-4-199302150-00007.

[30] Maurits J. Wiersema et al. "Endosonography-guided fine-needle aspiration biopsy: Diagnostic accuracy and complication assessment." In: *Gastroenterology* 112.4 (1997), pp. 1087–1095. ISSN: 0016-5085. DOI: https://doi.org/10.1016/S0016-5085(97)70164-1. URL: http://www.sciencedirect.com/science/article/pii/S0016508597701641.

[31] Kenneth J. Chang et al. “The clinical utility of endoscopic ultrasound–guided fine-needle aspiration in the diagnosis and staging of pancreatic carcinoma.” In: *Gastrointestinal Endoscopy* 45.5 (1997), pp. 387–393. ISSN: 0016-5107. DOI: https://doi.org/10.1016/S0016-5107(97)70149-4. URL: http://www.sciencedirect.com/science/article/pii/S0016510797701494.

[32] Carlos G. Micames et al. “Endoscopic ultrasound-guided fine-needle aspiration for non-small cell lung cancer staging: A systematic review and metaanalysis.” In: *Chest* 131.2 (2007), pp. 539–548. ISSN: 0012-3692. DOI: https://doi.org/10.1378/chest.06-1437. URL: http://www.sciencedirect.com/science/article/pii/S0012369215483424.

[33] Manuel Guizar-Sicairos and James R. Fienup. “Phase retrieval with transverse translation diversity: a nonlinear optimization approach.” In: *Optics Express* 16.10 (2008), pp. 7264–7278. DOI: 10.1364/OE.16.007264. URL: http://www.opticsexpress.org/abstract.cfm?URI=oe-16-10-7264.

[34] Xiaoze Ou et al. “Quantitative phase imaging via Fourier ptychographic microscopy.” In: *Optics Letters* 38.22 (2013), pp. 4845–4848. DOI: 10.1364/OL.38.004845. URL: http://ol.osa.org/abstract.cfm?URI=ol-38-22-4845.

[35] Roarke Horstmeyer and Changhuei Yang. “A phase space model of Fourier ptychographic microscopy.” In: *Optics Express* 22.1 (2014), pp. 338–358. DOI: 10.1364/OE.22.000338. URL: http://www.opticsexpress.org/abstract.cfm?URI=oe-22-1-338.

[36] Frans C.A. Groen, Ian T. Young, and Guido Ligthart. “A comparison of different focus functions for use in autofocus algorithms.” In: *Cytometry* 6.2 (1985), pp. 81–91. ISSN: 10970320. DOI: 10.1002/cyto.990060202.

[37] Yu Sun, Stefan Duthaler, and Bradley J. Nelson. “Autofocusing in computer microscopy: Selecting the optimal focus algorithm.” In: *Microscopy Research and Technique* 65.3 (2004), pp. 139–149. ISSN: 1059-910X. DOI: 10.1002/jemt.20118. URL: https://doi.org/10.1002/jemt.20118.

[38] Roarke Horstmeyer et al. “Diffraction tomography with Fourier ptychography.” In: *Optica* 3.8 (2016), pp. 827–835. DOI: 10.1364/OPTICA.3.000827. URL: http://www.osapublishing.org/optica/abstract.cfm?URI=optica-3-8-827.

[39] Remy Claveau et al. “Digital refocusing and extended depth of field reconstruction in Fourier ptychographic microscopy.” In: *Biomedical Optics Express* 11.1 (2020), pp. 215–226. DOI: 10.1364/BOE.11.000215. URL: http://www.osapublishing.org/boe/abstract.cfm?URI=boe-11-1-215.

[40] Timo Kohlberger et al. “Whole-slide image focus quality: Automatic assessment and impact on AI cancer detection.” eng. In: *Journal of Pathology Informatics* 10 (2019), p. 39. ISSN: 2229-5089. DOI: 10.4103/jpi.jpi_11_19. URL: https://pubmed.ncbi.nlm.nih.gov/31921487%20https://www.ncbi.nlm.nih.gov/pmc/articles/PMC6939343/.

*Chapter 3*

# NON-DESTRUCTIVE ANALYSIS OF SUBVISIBLE PARTICLES WITH MIE SCATTERING-BASED LIGHT SHEET TECHNOLOGY: SYSTEM DEVELOPMENT

The characteristics of subvisible particles (SbVPs) are critical quality attributes of injectable and ophthalmic solutions in pharmaceutical manufacturing. However, current compendial SbVP testing methods, namely the light obstruction method and the microscopic particle count method, are destructive and wasteful of target samples. Here we present the development of a non-destructive SbVP analyzer aiming to analyze SbVPs directly in drug product (DP) containers while keeping the samples intact. Custom sample housings are developed and incorporated into the analyzer to reduce optical aberrations introduced by the curvature of typical pharmaceutical DP sample containers. The analyzer integrates a light-sheet microscope structure and models the side scattering event from a particle with Mie scattering theory with refractive indices as prior information. Equivalent spherical particle size under assigned refractive index values is estimated, and the particle concentration is determined based on the number of scattering events and the volume sampled by the light sheet. The resulting analyzer's capability and performance to non-invasively analyze SbVPs in DP containers were evaluated using a series of polystyrene bead suspensions in ISO 2R and 6R vials. Our results and analysis show the particle analyzer is capable of directly detecting SbVPs from intact DP containers, sorting SbVPs into commonly used size bins (e.g., $\geq$ 2 $\mu$m, $\geq$ 5 $\mu$m, $\geq$ 10 $\mu$m, and $\geq$ 25 $\mu$m), and reliably quantifying SbVPs in the concentration range of 4.6e2 to 5.0e5 particle/mL with a margin of ± 15% error based on a 90% confidence interval.

## 3.1 Background of SbVP testing and regulations

The characteristics of subvisible particles (SbVPs) in the 1 to100 $\mu$m range [1–4] are critical quality attributes in pharmaceutical industry. Common sources of SbVPs include process and primary container-sourced particles intrinsic to the manufacturing process (e.g., plastic, glass), contaminants that are extrinsic to manufacturing (e.g., metal, dust), protein aggregates and other inherent biological particles, surfactant degradation products, and silicone oil droplets [5–9]. It has been reported that certain types of proteinaceous SbVPs in parental DPs may potentially trigger

immunogenicity thus causing safety concerns [4, 10–12]. According to the standards set by United States Pharmacopeial Convention (USP) in chapters USP <787>, USP <788>, USP <1787> and USP <1788> [13–16], and corresponding EP and JP monographs, SbVP testing is required for all final therapeutic protein products.

The light obstruction (LO) method [4, 9, 17–20] is one of the compendial SbVP test methods. A typical LO system has a light source facing a detector. The fluid flows between the light source and the detector. When a particle in the fluid passes through the light path, it obstructs part of the light and causes a decrease in the detector signal. The particle size is then calculated from the magnitude of the detector signal change. The microscope particle count test is the other compendial method for SbVP test [17, 18, 20]. It requires collecting, rinsing, and drying particles $\geq 10$ $\mu$m on a micro-porous membrane filter. The particles on the prepared sample filter are typically sized and counted under 100x magnification. The recent USP <1788> [16] includes flow imaging [9, 17–25] as a complementary test to LO particle test. Instead of a photo detector that senses the light intensity, a flow imaging system employs a camera to capture images of the particles as they pass through the light path. Therefore, the flow imaging method can provide morphological information which can benefit particle classification.

These compendial and associated methods are destructive and wasteful of the target samples. They require the liquid testing sample to be withdrawn from original DP containers. The LO method and the flow imaging method involve flowing the target fluid through the testing systems and into waste receptacles. The microscope particle count requires the particles of interest to be filtered out from the liquid sample for observation. As a result, the DP unit(s) and the liquid testing sample itself are completely destroyed as part of the method sample preparation and testing procedure. This results in a significant amount of waste. Applications such as product stability trending are particularly challenging due to in-batch vial-to-vial variability and waste. Non-destructive SbVP testing would provide clear benefits including improved data quality and reduced resource burden. A non-destructive testing method would be of particular benefit during drug product development requiring stress evaluation and stability monitoring. Testing would become easier and more representative of clinical settings when able to test drug solution within a primary container after application of stresses including storage, transport, freeze/thaw cycles, etc.

In this chapter, we report the development of a non-destructive Mie-scattering-based

light sheet (MSLS) liquid particle analyzer that is capable of directly analyzing SbVPs in parenteral DPs. The development goal for the MSLS analyzer is that testing with the analyzer is non-invasive and non-destructive, and after the testing the DP units (e.g., vials or syringes) remain intact and can be reused for other applications. To achieve this, we utilized a light sheet to illuminate the sample in containers such as vials or syringes and collected side scattered light directly from the SbVPs in the sample for testing. To compensate for the aberration caused by the cylindrical geometry of the DP vials, we developed custom housings which are compatible with ISO 2R and 6R vials and can be put on and taken off with ease. The sizes of scattering objects in the samples are determined by a Mie theory-based particle sizing algorithm. The concentrations of the particles detected and sized are calculated based on the number of particles detected and the volume sampled by the light sheet. Our goal at this stage of the development is to engineer the MSLS analyzer and algorithm that can 1) directly detect the SbVPs in intact 2R/6R DP vials, 2) size and sort the detected SbVPs into size bins such as $\geq 2$ $\mu$m, $\geq 5$ $\mu$m, $\geq 10$ $\mu$m, and $\geq 25$ $\mu$m, and 3) calculate size-based differential or cumulative particle concentrations. We evaluated the MSLS analyzer's capability and performance by analyzing polystyrene particle standards of different sizes and concentrations sealed in 2R/6R DP vials and report our results here. The system's strengths, limitations, potential applications, and future development plans are also discussed.

## 3.2 Principle of the MSLS analyzer

### System setup and general workflow

Our MSLS analyzer system functions like a light sheet microscope (see Fig.3.1(a) for setup schematics). A cylindrical lens (Thorlabs LJ1558RM, f = 300.0 mm) was used to generate a light sheet from a Gaussian beam produced by a 532 nm laser (Spectra Physics). The beam travels along the z-axis and only in the x-axis is light focused, resulting in the light sheet along the y-z (vertical) plane. Samples in vials were placed on a three-axis scanning stage. The sample vials were contained in housing which was designed to compensate for astigmatism introduced by cylindrical container geometry. Forward-scattered light along the z-axis was stopped by a beam block and the side-scattered light along x-axis from the particles within the sample was collected through a long working distance objective lens (Olympus LMPLFLN10X) and finally detected by an sCMOS camera (PCO edge 5.5). By using a tube lens (Thorlabs LA1433-A), we achieved a system magnification of 8.3x and corresponding field of view of 2.0 mm x 1.7 mm. Exposure time was

set at 20 ms for image capturing.

During light sheet image acquisition, the sample was scanned in three dimensions using the programmable stage and light sheet images were produced showing fields-of-view at different positions within the liquid sample. The scanning path is described in more detail in the appendix section 3.6. Fig.3.1(b) is an example of a captured light sheet image. The sample imaged was a water suspension of 3 $\mu$m polystyrene beads. Particle detection was performed on the acquired images to identify all the particles that appeared during the capturing. For each detected particle, its side-scattered light intensity was extracted from the corresponding pixel values, and its size was then determined by referencing a pre-calculated size-scattering intensity curve. By combining the results of all detected particles and considering the total imaging volume, a final calculation of particle size-concentration statistics of the testing sample was generated.

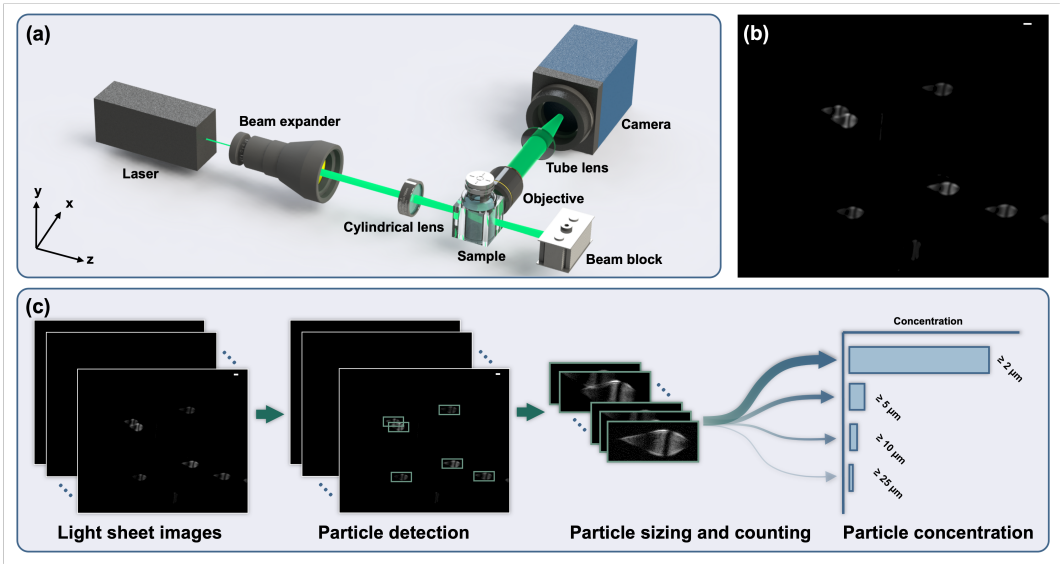


Figure 3.1: MSLS analyzer set up and workflow. (a) Simplified MSLS analyzer schematic. (b) A typical light sheet image captured by the MSLS analyzer. (c) Data processing workflow to extract SbVP size, concentration, and size distribution. Scale bar: 50 $\mu$m.

### Sample housing for astigmatism compensation

The cylindrical geometry of typical DP container (e.g., vials, syringes) produces severe astigmatism which presents a major obstacle to successful non-invasive imaging inspection. To reduce astigmatism a square sample housing was placed around the DP container. The sample housings were made of polydimethylsiloxane elastomer

(PDMS; SLYGARDTM 184) which has a refractive index (RI) of 1.43. The PDMS material was selected as it provides two significant benefits. First, PDMS is easy to mold and generates flat surfaces. Second, compared with air-liquid combination, PDMS-liquid combination has a smaller RI gap. This smaller gap results in lower astigmatism. Fig.3.2(a) shows the two types of sample housing created for ISO 6R vials (Fig.3.2(a2)) and ISO 2R vials (Fig.3.2(a4)). The detailed description of the sample housing production procedure was included in the supplementary document.

Fig.3.2 illustrates the effectiveness of the astigmatism-compensating sample housing by simulating the optical system and performing ray tracing with the RayLab software. The simulated system was simplified as follows: a point source was covered by a half cylinder, the light emitted from the light source was collected by a lens, and the light was detected by a screen. Fig.3.2(b to d) shows the patterns collected by the screen at several axial position near the focal plane (along the direction of the optical axis) with and without sample housing. It can be observed in the simulation results that the sample housing reduces the difference between the focal lengths of the tangential plane and the sagittal focal plane. By applying the sample housing, the astigmatism introduced by the cylindrical DP container is mitigated to an extent that enables subsequent particle detection to be performed.

It should be emphasized that the MSLS analyzer still images scattering objects with aberration when using the astigmatism-compensating sample housing. The side-scattered light from a particle formed a wide-spread, highly distorted "imprint" on the camera sensor whose shape was dominated by the system aberration instead of the morphology of the particle itself. As can be seen in Fig.3.1(b), a 3 $\mu$m particle's imprint had a size of ~150 $\mu$m, far exceeding the particle's actual size. However, the extent of the astigmatism of the MSLS analyzer was reduced enough to pose no obstruction to the particle sizing task. The MSLS analyzer extracted the side-scattering light intensity of the captured particles rather than relied on their imprint morphology information. In addition, while the morphology of a given particle was affected by the cylindrical aberration, the side-scattered intensity of a particle was not affected by the presence of an aberration as long as the side-scattered light was effectively collected by the objective lens. Furthermore, the astigmatism observed by the MSLS analyzer actually benefits the particle sizing and counting task. These benefits come in two ways. First, the astigmatism produces similar scattering imprints of particles having different sizes. This outcome enables a conventional template matching strategy to be used to robustly detect particles.

Second, the astigmatism helps in estimating a particle's axial position and aiding the determination of accurate incident light intensity for a given particle. Further details about particle detection, sizing and counting are elaborated in subsequent sections.

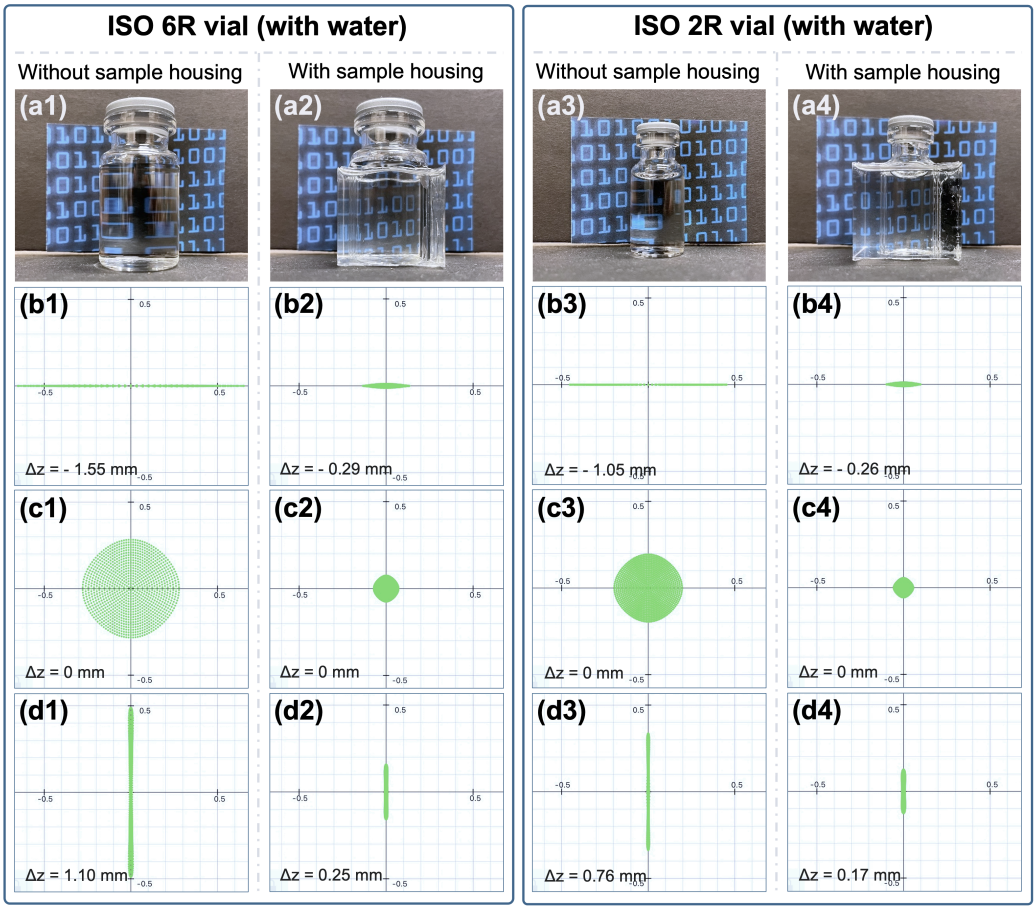


Figure 3.2: Demonstration of sample housing astigmatism compensation. (a) Vials with and without sample housings. The patterns behind the vials were less visually distorted after putting on sample housings. (b) Spot diagrams from RayLab software at the tangential focal planes of (b1) ISO 6R vial without sample housing, (b2) ISO 6R vial with sample housing, (b3) ISO 2R vial without sample housing and (b4) ISO 2R vial with sample housing. (c) Spot diagrams at positions where the image of the simulated point source was with aspect ratio of 1 for (c1) ISO 6R vial without sample housing, (c2) ISO 6R vial with sample housing, (c3) ISO 2R vial without sample housing and (c4) ISO 2R vial with sample housing. (d) Spot diagrams at the sagittal focal planes of (d1) ISO 6R vial without sample housing, (d2) ISO 6R vial with sample housing, (d3) ISO 2R vial without sample housing and (d4) ISO 2R vial with sample housing. Unit: mm.

**Particle detection by template matching method**

Template matching by means of cross correlation was used for the particle detection task [26]. The particle imprints in a captured image could be broadly regarded as a template imprint being translated and duplicated multiple times without size scaling or rotation. For the MSLS analyzer, the templates (for both ISO 2R vials and 6R vials) were manually cropped from the corresponding light sheet image sets of PS-bead standard solutions containing 3 $\mu$m polystyrene beads only.

Fig.3.3 illustrates how the MSLS analyzer image processing software performed particle detection. First, the image that particle detection was being applied to was labeled as the input image. Two steps of preprocessing (① in Fig.3.3) were performed before applying the normalized cross-correlation between the template and the input image. 1) Both the template and the input image were down-sized by a factor of 10 (for both width and height) for higher processing speed. 2) Both the down-sized template and input image were Gaussian blurred to eliminate multiple peaks for a single match. Normalized cross-correlation (② in Fig.3.3) was then performed between preprocessed template and input image. An example of a correlation map is shown in Fig.3.3 where a peak indicates that a particle imprint was detected. To localize the valid peaks in a 10x down-sized thumbnail source image (③ in Fig.3.3(a) and Fig.3.3(b)), we first applied a binary threshold (threshold = 0.3) to the correlation map, leaving only peaks with a high enough correlation score. The remaining blobs indicating the cross-correlation peaks were then extracted and the positions of the maximum values within each blob region were determined. To suppress the situation where multiple peaks corresponding to the same particle imprint were found, Matlab function pcsegdist was used to group close peaks such that its output peaks were with minimum distance of d from each other. The minimum distance d was determined by the template size:

$$d = 0.6 \times min(height_{template}, width_{template}). \tag{3.1}$$

The peak locations in the 10x down-sized thumbnail images could then be remapped to the original input image. Bounding boxes centered on the peak positions in the original input image, with the size of 1.4x that of the template, were placed to box out the found particle imprints in the original input image (④ and ⑤ in Fig.3.3). Based on the bounding boxes, individual particle imprints were then cropped out for subsequent particle sizing process.

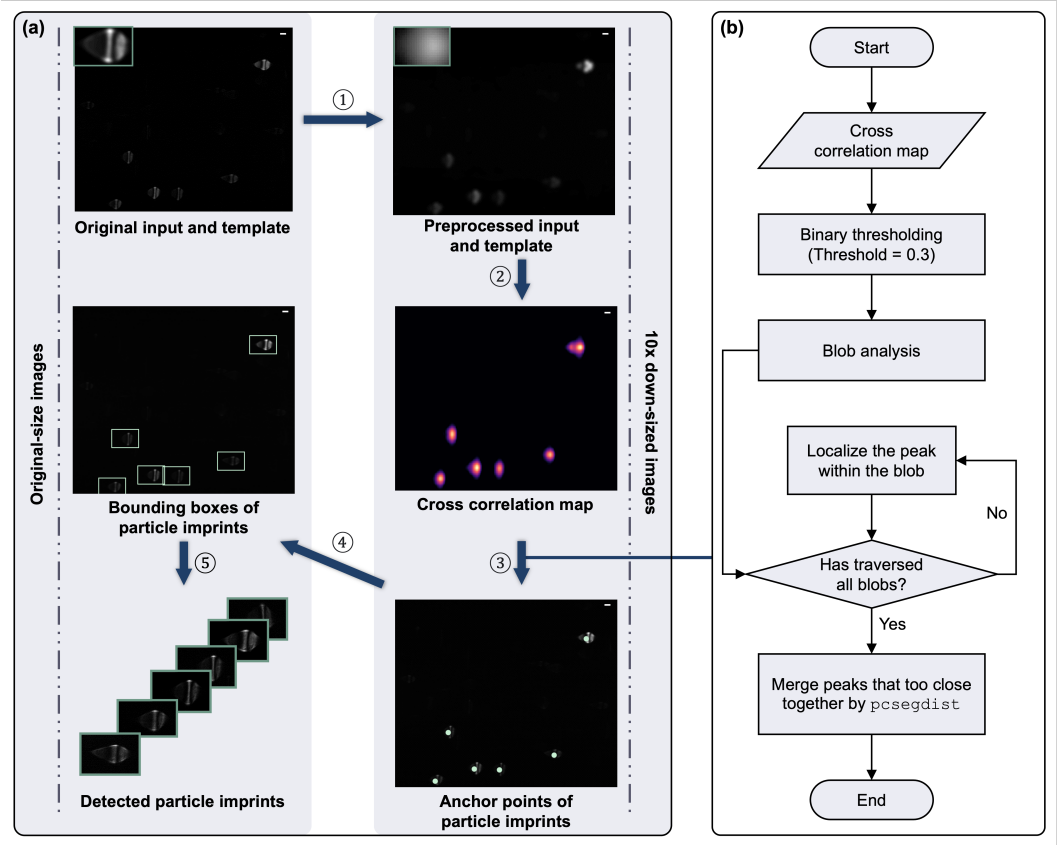


Figure 3.3: Particle detection process. (a) The overall particle detection process. Step 1: Down-sizing and Gaussian blurring both the template and the input image. Step 2: Normalized cross-correlation between the template and the input image (both are 10x down-sized thumbnails). Step 3: Peak localization. Step 4: Placing bounding boxes around detected particle imprints. Step 5: Cropping out each individual particle imprints. (b) Detailed flow chart of the peak localization algorithm (Step 3). Scale bar: 50 $\mu$m.

### Mie-scattering based particle sizing and counting

Fig.3.4(a) illustrates the process of particle sizing for a given particle imprint. The found particle imprints underwent astigmatism-based localization and Mie-scattering based size calculation. The results of all the particle imprints were aggregated together to generate the final particle statistics of the test sample.

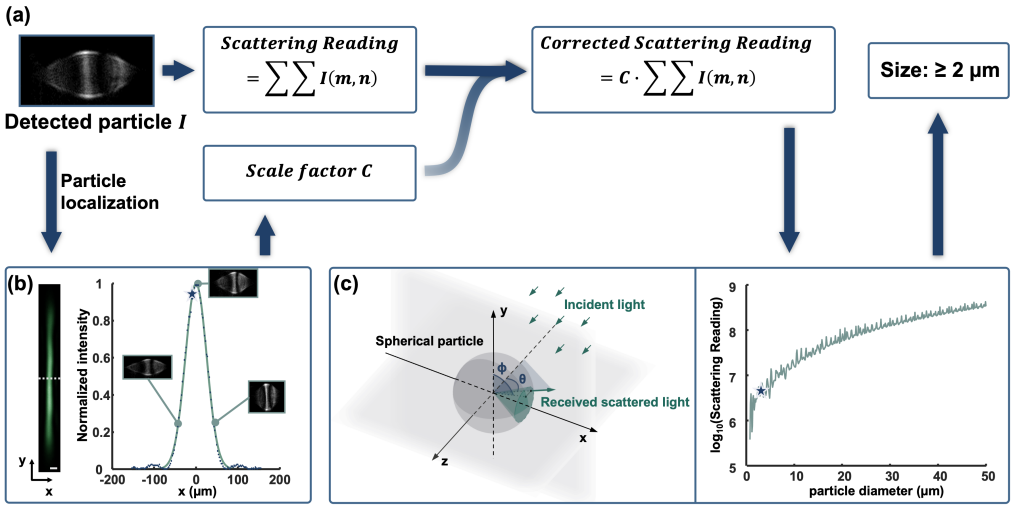


Figure 3.4: Particle sizing process. (a) Workflow for determining the particle size from the particle imprint. (b) The light sheet generated by the MSLS analyzer and the particle imprints at varied axis positions (-60, 0 and 60 $\mu$m). The intensity profile is along the dash line and its corresponding Gaussian fit are presented. The star mark indicates the axial location of the particle. Scale bar: 100 $\mu$m. (c) The Mie scattering model scheme and the derived scattering reading curve. The star mark indicates the scattering reading of the certain particle imprint in this figure.

### Mie-scattering model

Our particle sizing method is based on Mie scattering theory [27]. Mie scattering theory is a solution to Maxwell's equations. It applies to all SbVPs sized within our scope of interest. The intensity of the side - scattered light was an indicator of the particle size. To connect the side-scattering intensity with the pixel values of a particle imprint, a parameter referred to as scattering reading (SC) was introduced, which was defined as the sum of all the pixel values within its corresponding bounding box, as illustrated in Fig.3.4(a). The particle size - scattering reading curve was calculated based on a simplified Mie scattering model demonstrated in Fig.3.4(c). Scattering was approximated as a scenario in which a spherical particle scatters incident plane wave light. By considering a specific solid angle range within which the scattered light could be received by the objective lens, the scattering cross section of a particle was calculated. From the incident light intensity and the camera specifications, including exposure time, quantum efficiency and conversion factor, the scattering reading for a particle with certain size was calculated. The detailed derivation of the particle size-scattering reading curve is explained in the appendix

section 3.6.

### Illuminating light sheet cross section and sampling volume of the MSLS analyzer

From our scattering model, accurate particle size determination relied on accurate measurement of the incident light sheet itself. Therefore, the light sheet was examined directly using an observation camera (the imaging source DMK23UP031). The cross-section of the light sheet is shown in Fig.3.4(b). The full width at half maximum of the light sheet was measured to be 58.6 $\mu$m. The normalized Gaussian fitting of the light sheet profile was expressed as (unit: $\mu$m):

$$f = exp(-(\frac{x - 0.15}{0.0035})^2). \tag{3.2}$$

Combining the light sheet thickness, the pixel count and size of the camera and the magnification of the MSLS analyzer, the sampling volume of a single frame was determined to be 3.7e-4 mL. During one measurement, 700 frames from different positions imaged within the container were captured, resulting in a total sampling volume of 0.26 mL.

### Astigmatism-based particle localization and particle sizing

It was clear that particles at different axial locations did not share the same incident light intensity (as shown in Fig.3.4(b)). However, the particle size - scattering reading curve was calculated based on a consistent incident light intensity value. In our case, the peak intensity value of the light sheet was used, i.e., the particle size - scattering reading curve was based on a situation where the incident light has the intensity of our light sheet peak value. Particles that are imaged with location off center of the light sheet exhibit incident light intensity lower than the light sheet peak value. Therefore, directly referring to the size – scattering reading curve for off-center particles will result in underestimation of the particle size. There are two possible approaches for correcting such off-light-sheet-center error. The first way is to perform particle tracking across different frames and record the corresponding scattering readings. A particle will generate maximum scattering reading when it is at the light sheet center. Thus, querying the scattering reading curve with a particle's maximum scattering reading should result in a more accurate estimation of the particle size. The other way is to localize the particle axially and then apply a scale factor to correct for the particle off-light-sheet-center error. The particle

tracking method was intuitively straight-forward, but it would not be able to handle the situation when a particle never passes the center of the light sheet. Conversely, the particle localization method did not depend on the prerequisite that the particle must pass the light sheet center. Moreover, considering the residual astigmatism in our reported system, particle localization could be achieved without introducing any additional modulation into the imaging system. Therefore, the particle localization method was chosen as our approach, and procedural details are elaborated in the following paragraph.

Due to the cylindrical nature of the vials and the imperfect RI matching between the PDMS sample housings (RI: 1.43) and the contents of the DP containers (RI: 1.33 to $\sim$ 1.37), there was a residual amount of astigmatism in the imaging system. This was serendipitously helpful as it caused the imprint of a particle to elongate in different directions (either horizontally or vertically) to varying extents at different axial locations [28–33]. We used this distortion as an axial particle location estimator.

The aspect ratio of a particle imprint was designated as the indicator to be observed, and its variation with the axial position of the particle was recorded as a further reference for the localization process. The relation between aspect ratio of a particle imprint and the axial position of the particle was evaluated through experimentation. As mentioned previously, the particle imprints were aberration dominant and particle size insensitive. As such, the axial particle location estimator can be calibrated by using only 3 $\mu$m polystyrene beads (Polybead, 17134-15, coefficient of variance: 5%) without loss of generality. The focal plane of objective was scanned from -60 to 60 $\mu$m with step size of 10 $\mu$m, while the light sheet and the sample remained stationary. For each captured image, autocorrelation was performed, and the aspect ratio of the main autocorrelation peak was calculated. In the situation where the particles to be imaged are of comparable size, the captured image can be expected to contain the imprints of particles at different axial positions and the particles at the light sheet center should always produce the strongest signals on the camera sensor because they are illuminated by the most intense light. Thus, the main peak of the autocorrelation was dominated by the particles at the light sheet center. As such, one could obtain the aspect ratio of the in-center particle imprints by analyzing the aspect ratio of the main peak of the autocorrelation of the captured image. Linear fitting was performed between axial positions and the imprints of particles to determine the slope ($\beta$). With the fitted slope ($\beta$) and the templates representing the in-center particle imprints, the off-center distance ($\Delta$x) of a particle of interest

could be determined by comparing its aspect ratio ($AR_p$) with the template's aspect ratio ($AR_t$):

$$\Delta x = \beta \cdot (AR_p - AR_t). \tag{3.3}$$

Both $AR_p$ and $AR_t$ were calculated from the corresponding autocorrelations of the particle of interest and the template. According to our experiment the slope ($\beta$) for large vial was found to be –17 and the slope ($\beta$) for small vial was found to be –21, Details of this analysis and data are provided in the appendix section 3.6.

The scale factor C for correcting the off-center error was then determined by finding the intensity decrease at axial position Δd compared to the maximum value from the light sheet's cross-section profile $f$:

$$C = \frac{1}{f(\Delta x)}. \tag{3.4}$$

With the corrected scattering reading, the particle size was able to be determined from the particle size – scattering reading curve and then binned into the following categories: $\geq 2$ $\mu$m, $\geq 5$ $\mu$m, $\geq 10$ $\mu$m, and $\geq 25$ $\mu$m, consistent with USP <787> and USP <788> [13, 14] approaches and common practices.

## 3.3 Results on polystyrene bead standards

**Verification of Mie-scattering based particle sizing model**

We compared measured scattering readings of four sizes of standard polystyrene beads (3 $\mu$m, 8 $\mu$m, 15 $\mu$m and 30 $\mu$m, corresponding to our size bins: $\geq 2$ $\mu$m, $\geq 5$ $\mu$m, $\geq 10$ $\mu$m, and $\geq 25$ $\mu$m) with their corresponding theoretical calculations. Samples were made by diluting polystyrene bead standards with deionized water and filling them in both 6R and 2R vials. Each sample contained beads of a single size. 100 frames were taken for each sample. To isolate the influence of the particle location mentioned in the section 3.2 and possible errors from our computer vision algorithms, we manually selected the brightest particle imprint for each frame and obtained its scattering reading. The brightest imprint indicates that the particle was at the center of the light sheet. Consequently, for each sample (corresponding to one particle size and one type of container), 100 imprints were selected, and their scattering readings were presented as a box plot.

Theoretically calculated scattering readings were also plotted. For each particle size, the box encompassed the scattering reading values of particles within a certain size range with its minimum being the designated particle size minus its coefficient of variance and its maximum being the designated particle size plus its coefficient

of variance. The scattering reading calculation followed the procedure elaborated in section 3.2.

The comparison is shown in Fig.3.5. The results verified our Mie-scattering based particle sizing model by demonstrating: 1) particles with larger size generated higher scattering readings, and 2) measured scattering readings matched well with corresponding theoretical calculations.

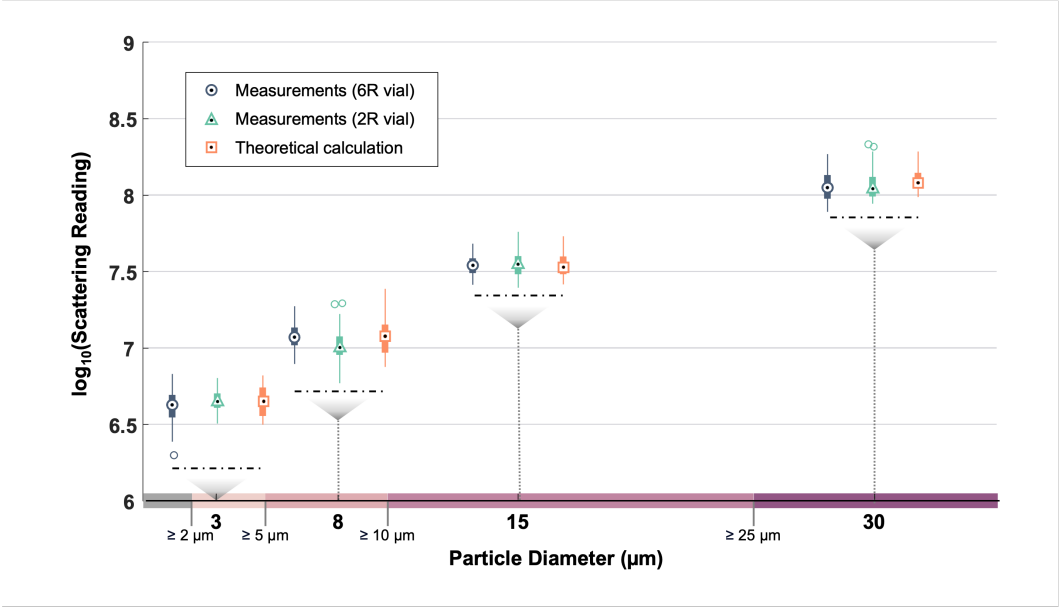


Figure 3.5: Scattering reading comparison between measurements and theoretical calculation for 3 $\mu$m, 8 $\mu$m, 15 $\mu$m and 30 $\mu$m bead standards. Box plots of the scattering reading values for given standard bead sizes were provided. The scattering reading value ranges originated from the size distribution of each bead standard (designated size ± coefficient of variance).

**Experiments on mixed polystyrene particle standard samples**

A series of samples was prepared using PS bead standard solutions to demonstrate the functionality of the MSLS particle counter. For each type of sample solution, the particle size statistics based on vendor provided specifications are listed in Table.3.1. Samples were prepared in both ISO 2R vials and 6R vials. Particle size statistics of the prepared samples were verified using a hemocytometer. The reference particle statistical data are listed in Table 1. The MSLS measurements were repeated three times for each sample. The total acquisition time including the exposure time and stage scanning time for each measurement added up to 7 min. The analysis time, including particle detection and sizing after the data acquisition, was 4 min.

| | ≥ 2 $\mu$m | ≥ 5 $\mu$m | ≥ 10 $\mu$m | ≥ 25 $\mu$m |
|---|---|---|---|---|
| Di Water | / | / | / | / |
| 3 $\mu$m polystyrene bead | 0.99e4 | 0 | 0 | 0 |
| 3 $\mu$m + 8 $\mu$m polystyrene bead | 0.99e4 | 1.1e2 | 0 | 0 |

Table 3.1: Particle statistics of prepared samples

Results from analyzing the samples prepared are shown in Fig.3.6(a)-(b). Negative control samples (distilled water, without polystyrene beads) produced near-zero results for all size ranges when analyzed by the MSLS instrument. For samples with addition of the bead standard solution, the MSLS particle analyzer produced concentration values comparable to the reference values acquired by hemocytometer, with different error bar widths at different orders of magnitude of particle concentrations.

The importance of the relationship between the results observed and the sampling volume scanned should be emphasized based on the learnings of this study. The minimum concentration value that the MSLS analyzer could provide was 3.8 particles/mL – effectively equal to one particle over the total sampling volume of 0.26 mL. One can also analyze the relationship between the total imaging volume and the target particle concentration from a perspective of statistical inference. The number of particles captured in a single frame should follow a Poisson distribution with a mean equal to the actual concentration multiplied by the imaging volume. One measurement containing N frames could be regarded as sampling N times from the Poisson distribution, and the final reported particle concentration is the mean value among all N samples. According to the Central Limit Theorem, the reported particle concentrations will follow a Gaussian distribution, and the standard deviation of the reported particle concentrations depends on both the frame number N and the actual concentration of the target particles. A larger frame number and a higher target particle concentration will result in a smaller percentage error. This trend could be observed in our results. For 3 $\mu$m particles with a concentration of approximately 1e4 particles/mL among all 4 samples, the standard deviations of all groups of 3 measurements were less than 5%. However, for 8 $\mu$m particles with a concentration of approximately 1e2 particles/mL in two of the 3 + 8 $\mu$m samples, the standard deviations of the two groups of 3 measurements were around 17%. Based on this observation and further derivation, it was determined that given a current frame number of the MSLS analyzer, at a concentration of 463 particles/mL or higher, the results can be expected to be within a margin of ± 15% error with a 90% confidence interval, or better. A detailed derivation is provided in the appendix section 3.6.

Fig.3.6(c) shows a typical error that the MSLS analyzer encountered during the measurements when two particle imprints became close to or even overlapped with each other. In such cases, particle size was overestimated because of the contribution of extra scattered light from other particles. When particle concentration of a sample becomes high enough that the particle imprints overlap frequently, the MSLS analyzer would fail to provide accurate particle statistics (size and concentration). A simulation described in the appendix section 3.6 was developed to determine an upper concentration bound of the MSLS analyzer. When the breakdown proportion of overlapped imprints was set to be 10%, the corresponding upper concentration limit was found to be 5.00e5 particle/mL.

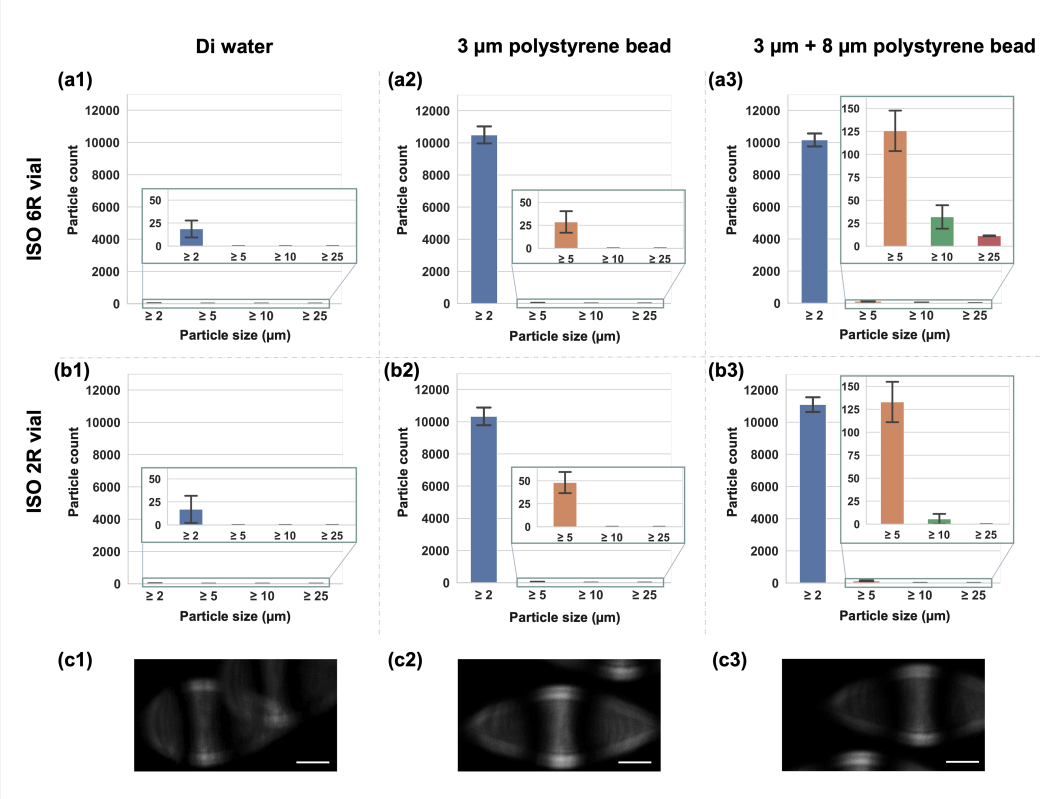


Figure 3.6: Functionality of the MSLS analyzer. (a) Results of the ISO 6R vial samples. (b) Results of the ISO 2R vial samples. (c) Typical error (close or overlapping imprints) encountered in the MSLS analyzer. Scale bar: 50 $\mu$m.

## 3.4 Results on actual protein samples

To further demonstrate the functionality of the MSLS analyzer, in addition to experiments on polystyrene beads, we conducted two experiments on monoclonal antibody (mAb) drug samples. In this section, first we analyze the unique challenges presented

by antibody molecules, then we present the experimental results.

**Background scattering by protein molecules**

From a scattering analysis perspective, mAb products differ from polystyrene bead suspensions. In a polystyrene bead suspension, there's one type of particle (the polystyrene bead) in water. These beads fall within the submicron-to-visible particle (SbVP) range and are the focus of MSLS analysis. In contrast, mAb products contain two main types of particles: mAb molecules and mAb aggregates, typically in a buffer solution like acetate buffer. The mAb molecules, about 10 nm in size, are the intended product content. However, mAb aggregates—clusters formed by these molecules—fall within the SbVP range and become the target of the MSLS analyzer.

The complex composition of mAb products introduces additional challenges to particle analysis. The mAb molecules themselves scatter light, creating a background in MSLS images. This increased background signal could potentially reduce the detectability of submicron-to-visible particles (SbVPs). To assess the detectability of SbVPs in the presence of mAb molecules, we developed a simplified particle model for mAb products, as illustrated in Fig.3.7.

Two factors primarily impact the detectability of SbVPs. First, the presence of mAb molecules generates noticeable background signals (Fig.3.7(a)—(c)). Second, when mAb aggregates become too dense, they overlap, posing difficulties for particle detection algorithms (Fig.3.7(a) and (d)). The detailed analysis of how SbVP overlap impacts detectability has been elaborated in Chapter 3. Therefore, we focus here on how background scattering affects SbVP detectability.

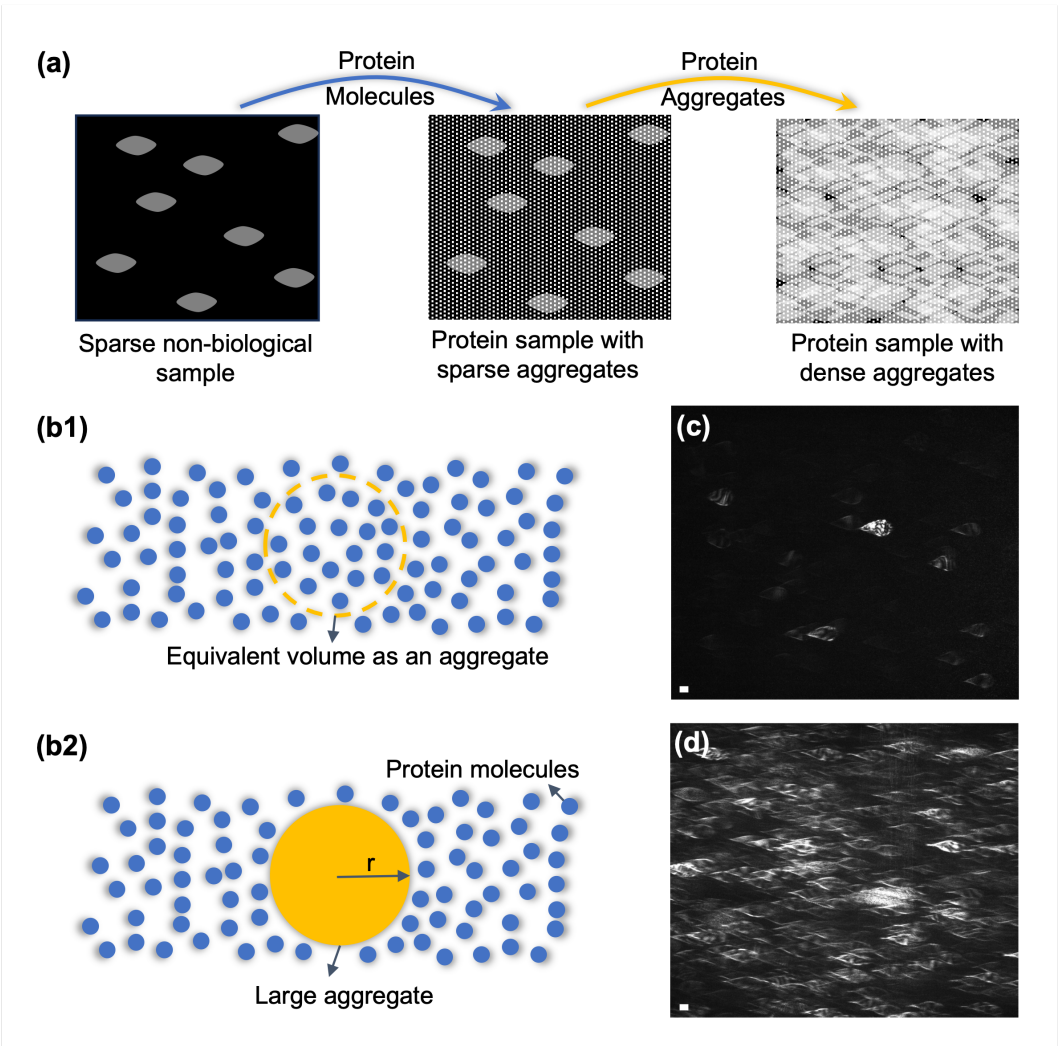


Figure 3.7: Particle Detectability Analysis. a) Two factors that may reduce particle detectability. b) Simplified particle models, both without and with mAb aggregates. c) Light sheet image of an mAb product showing sparse aggregates. d) Light sheet image of an mAb product showing dense aggregates.

Examining the scenarios with and without mAb aggregates in Fig.3.7(b), we can establish a condition for an mAb aggregate to be distinguishable from the background. This condition is met when the scattering intensity (reading) of the aggregate ($SC_{aggregate}$) is stronger than that of the mAb molecules ($SC_{molecule}$) within the same volume, which can be expressed as:

$$SC_{aggregate} > N_{molecules} \cdot SC_{molecule} \tag{3.5}$$

with $N_{molecules}$ represents the number of mAb molecules contained within a volume equivalent to that of the mAb aggregate.

For simplicity, we assume that all particles, both mAb molecules and mAb aggregates, are spherical and share an identical refractive index (RI), resulting in a relative RI with the medium of $m$. The radius of the mAb aggregate ($r_{aggregate}$) ranges from 1 to 50 $\mu$m, while the radius of a single mAb molecule ($r_{molecule}$) is 5 nm. The scattering readings for an mAb aggregate ($SC_{aggregate}$) and for a single mAb molecule ($SC_{molecule}$) are derived using the same method detailed in Section 3.6.

The particle concentration ($c_{mAb}$) of mAb molecules in a product can be calculated using the mAb's mass concentration ($\rho_{mAb}$) and its molecular mass ($m_{mAb}$):

$$c_{mAb} = \frac{\rho_{mAb}}{m_{mAb}} \cdot N_A \tag{3.6}$$

where $N_A$ is the Avogadro number.

Using the particle concentration of mAb, the number of mAb molecules within the volume of an aggregate can be calculated, allowing us to assess whether the aggregate stands out from the background:

$$N_{molecules} = c_{mAb} \cdot \frac{4}{3} \cdot \pi r^3_{aggregate}. \tag{3.7}$$

Using the aforementioned method, we analyzed an extreme case where the aggregate has the minimum SbVP size ($r_{aggregate} = 1, \mu m$) and the mAb has a mass concentration typical in the drug industry ($\rho_{mAb} = 140$mg/ml). We varied the relative refractive index (RI) between the mAb and the buffer from 1.0001 to 1.1, and the corresponding scattering values, as well as whether the aggregate could be detected, are presented in Table3.2. The results show that, except for the $m = 1.0001$ case, the aggregate could be detected in all other scenarios, even with background scattering. Given that a relative RI as low as 1.0001 is uncommon in typical drug products, we conclude that the MSLS analyzer is still effective in detecting SbVPs in mAb drug samples. Particle sizing can be performed after an additional background subtraction step, with the background frame obtained by averaging multiple MSLS images.

| $m$ | $\frac{SC_{aggregate}}{N_{molecules} \cdot SC_{molecule}}$ | Aggregate detectability |
|---|---|---|
| 1.0001 | 0.15 | × |
| 1.001 | 15 | √ |
| 1.01 | 1.7e3 | √ |
| 1.1 | 1.8e6 | √ |

Table 3.2: Aggregate detectability across various relative refractive indices (RI)

**Dilution experiment on aggregated mAb products**

We began with a dilution experiment to quantitatively demonstrate the MSLS analyzer's capability in analyzing actual mAb samples. First, we prepared an aggregate sample with 10 mg/mL mAb agitated for 24 hours. We then performed a series of dilutions to create samples ranging from 0.0 vol% to 1.2 vol% of the original aggregate concentration. Each dilution was analyzed three times using the MSLS analyzer. To maintain the mAb molecular concentration, the final formulated bulk mAb product at 10 mg/mL was used for dilution. The experiment involved both ISO 6R and ISO 2R vials. All dilutions were performed in a single 6R vial, followed by pipetting the diluted samples into separate 2R vials at each target concentration, as illustrated in Fig.3.7(a).

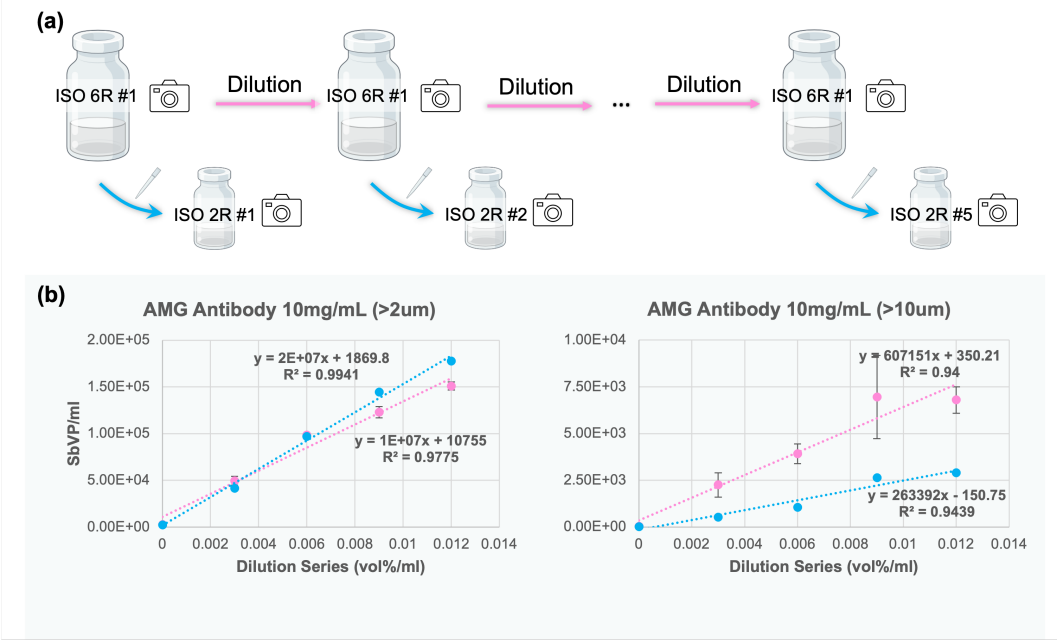


Figure 3.8: MSLS performance on an mAb dilution series. a) Sample dilution workflow. b) SbVP analysis results for ISO 6R and 2R vials, focusing on particle size classes of $\geq 2\mu m$ and $\geq 10\mu m$.

The analysis results of the dilution series in both ISO 6R and ISO 2R vials are presented in Fig.3.8(b). For particles $\geq 2\mu m$, both ISO 6R and ISO 2R results exhibit strong linearity between the dilution series and SbVP concentrations, with the values closely aligned, demonstrating the quantitative accuracy of the MSLS analyzer. However, for particles $\geq 10\mu m$, while linearity was also observed, discrepancies were noted between the results from the ISO 6R and ISO 2R vials. These differences may be attributed to potential pipetting bias or other procedural inconsistencies introduced during the dilution process. Overall, the MSLS analyzer has demonstrated good quantitative performance with actual mAb samples, reinforcing its reliability for assessing particle concentrations across different size ranges. These findings suggest that the analyzer is capable of providing robust and consistent measurements in practical applications, particularly for smaller particle sizes.

### 37° mAb products

To showcase the MSLS analyzer's advantage of enabling experiments on a single drug sample, we conducted a 37°C incubation experiment. As demonstrated in Fig.3.9, nine 70 mg/mL mAb samples in three types of buffer were incubated at

37°C for 18 days. The buffers used were acetate (pH 5.2), phosphate (pH 6.7), and histidine (pH 7.6). Measurements using the MSLS analyzer were performed daily, with each measurement repeated three times, to observe how samples changed under high temperature and how different buffer pH levels affected sample stability.

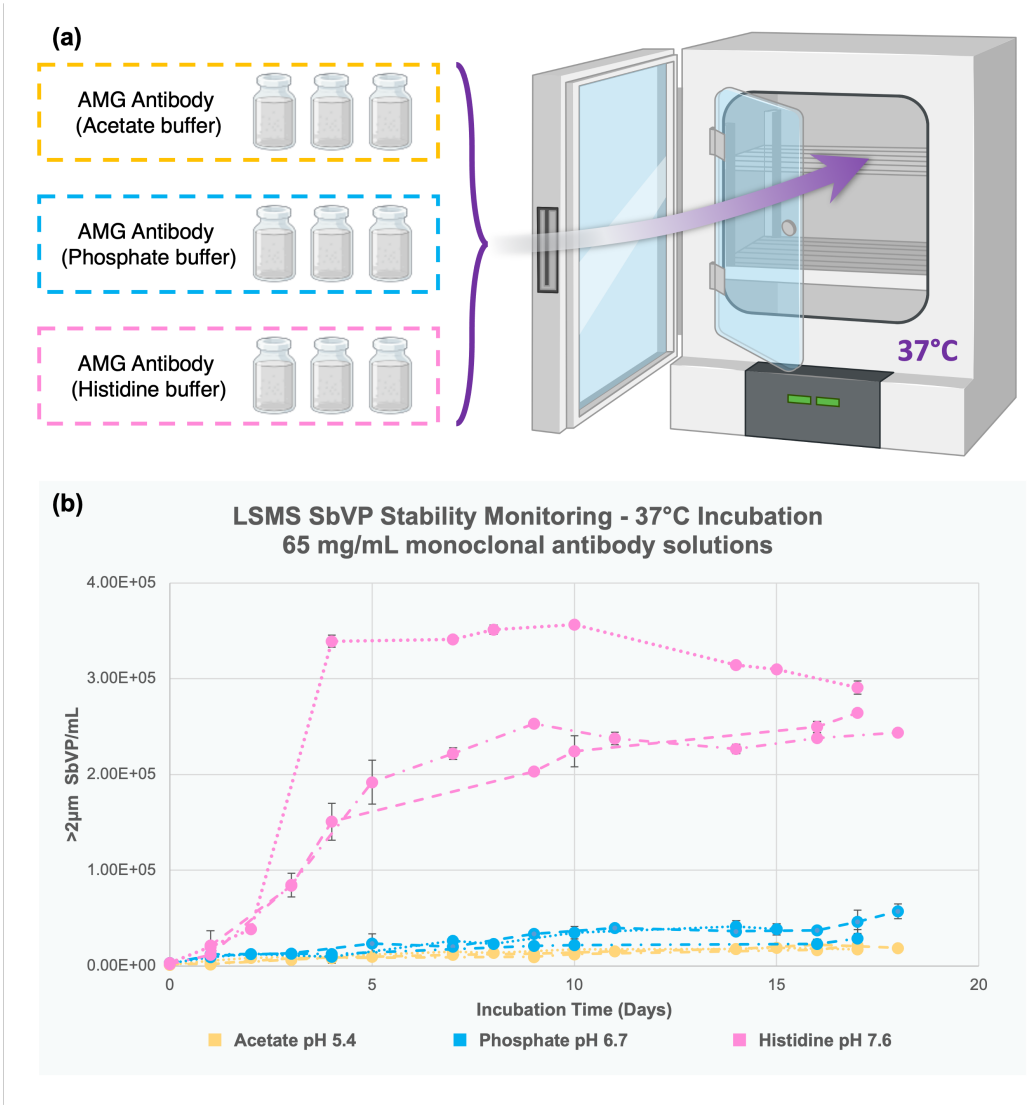


Figure 3.9: MSLS Performance in a 37° Incubation Experiment. a) Experimental process. b) SbVP tracking of the experimental samples over 18 days. Particles $\geq 2\mu m$ are presented to illustrate the general trend.

The SbVP tracking results are presented in Fig.3.9(b). All samples showed growth in SbVP particles, but to varying degrees. Histidine-buffered samples (pH 7.6) exhibited a rapid increase in SbVP counts during the first 5 days, after which they began to saturate the MSLS analyzer. Phosphate-buffered samples (pH 6.7) showed

a modest increase in SbVPs throughout the incubation period. Acetate-buffered samples (pH 5.2) demonstrated the highest stability, with the least SbVP growth. These observations align with previous studies indicating that higher sample pH correlates with increased SbVP growth rates [34]. Variability among samples was also observed, which could be attributed to random impurities introduced during sample preparation. In summary, this incubation experiment demonstrates the MSLS analyzer's capability to track SbVP changes over time, emphasizing its advantage over invasive methods.

### 3.5 Discussion of advantages and limitations

The MSLS analyzer was developed to characterize subvisible particles in pharmaceutical DP containers non-destructively. The system uses light sheet microscopy and an algorithm that models Mie scattering to directly perform particle sizing and counting while keeping the sample solution intact inside primary containers. Representative DP containers (ISO 2R vials and ISO 6R vials) were chosen as primary containers to test in this study. Square sample housings made of PDMS were designed to partially compensate for the strong astigmatism inherent to cylindrical containers. As the particle imprint of the system was still aberration dominated, particle detection was achieved by template matching. For every detected particle imprint, astigmatism-based particle localization was performed to determine the corresponding incident light intensity. This information was then used to scale the particle's scattering reading accordingly such that the pre-calculated particle size – scattering reading curve could be used for querying the size of the particle. By combining the results of all the particles within the imaging volume, a calculation of the particle concentration statistics for a sample was generated.

As an optics based SbVP analyzer, it is inevitable that the MSLS analyzer will miss particles with the exact same refractive index as the medium because there will be no side scattered light for the MSLS analyzer to capture. However, existing research [35] has shown that in most cases, the refractive indices of SbVPs and the suspension medium, although close, are not precisely identical. Under such circumstances, side-scattered light would still be present, and the reported MSLS analyzer could potentially detect this light by employing appropriate exposure time settings. Limitations of the MSLS analyzer also include the dependency on the refractive index values of the medium and the particles. Furthermore, we would like to clarify that the MSLS analyzer could estimate the particle size range but could not measure the exact particle size. Two factors contributed to this. 1)

The scattering model described here makes two simplifications during the particle sizing process. The first simplification was to assign consistent particle refractive index to all particles even though the particles may have different compositions and therefore refractive indices. The second simplification was to assume all particles as spheres. In other words, our system outputs the equivalent spherical particle size that would generate the same scattering reading as our measurement under assigned refractive index values. 2) The scattering reading values exhibited fluctuations as the particle size increased, as observed in Fig.3.4(c). This property resulted in situations where a single scattering reading would indicate a range of acceptable particle size. Therefore, even though algorithmically the MSLS analyzer could bin the particle statistics in a finer way than the $\geq$ 2, 5, 10, and 25 $\mu$m convention, it would not contribute to higher sizing precision.

The main advantage of the reported MSLS analyzer was its non-invasiveness. The only required operation involving the sample was to place it inside the sample housing. Furthermore, the sample housings were reusable and easy to produce. The control of astigmatism was the main contributor in enabling the non-invasiveness. Sample housings were used to mitigate strong astigmatism enough such that image processing could be performed to deliver a clean scattering signal to the Mie scattering algorithm. Additionally, residual astigmatism played a crucial role in particle axial localization and accurate size estimation. The MSLS analyzer is expected to be non-destructive to modern protein biologics. The analyzer light wavelength is 532 nm, the optical intensity is 3.66 mW/cm$^2$ (2.0e7 lux), and sample exposure time is about 7 minutes (Table.3.3). For well-formulated protein therapeutic products, exposure to light at this wavelength and intensity is not expected to degrade the product [36].

The MSLS analyzer could be extended to analyzing syringe DPs by creating corresponding sample housings. Furthermore, the sample housing could potentially be improved by investigating materials with refractive index values closer to those of the drug product content. Moreover, the MSLS analyzer could be utilized for measuring bulk solution properties, such as color and turbidity. Color measurement can be achieved by embedding a spectrometer module into the current system set up. Sample turbidity could be acquired by quantitatively calibrating measured light sheet image pixel values with turbidity standards. Further improvements to the MSLS analyzer could include replacing mechanical sample scanning with light sheet scanning for higher measuring speed, as well as exploring light features that

could serve as indicators for particle characteristics such as size, shape, or chemical composition. In its present state, the MSLS system and its processing software assume and assign a single refractive index value to all particles in a test sample; articles with refractive indices different from the assigned value will result in a size different from their true value. Therefore, the MSLS analyzer is well-suited for monitoring the SbVP change over time (i.e., stability) in a single sample (DP unit). If the particles are of unknown origin or multiple types [37], the MSLS analyzer will still be able to see a change notwithstanding with compromised sizing and counting accuracy.

## 3.6 Appendix

### Scanning scheme of the MSLS counter

One measurement of the MSLS counter for both ISO 6R vial samples and ISO 2R vial samples consisted of 700 frames. Fig.3.10(a) showed the scanning scheme of an ISO 6R vial sample. The MSLS counter scanned 5 layers of an ISO 6R vial. Each layer contained 140 frames. Similarly, for ISO 2R vial samples, the MSLS counter scanned 10 layers and each layer contained 70 frames.

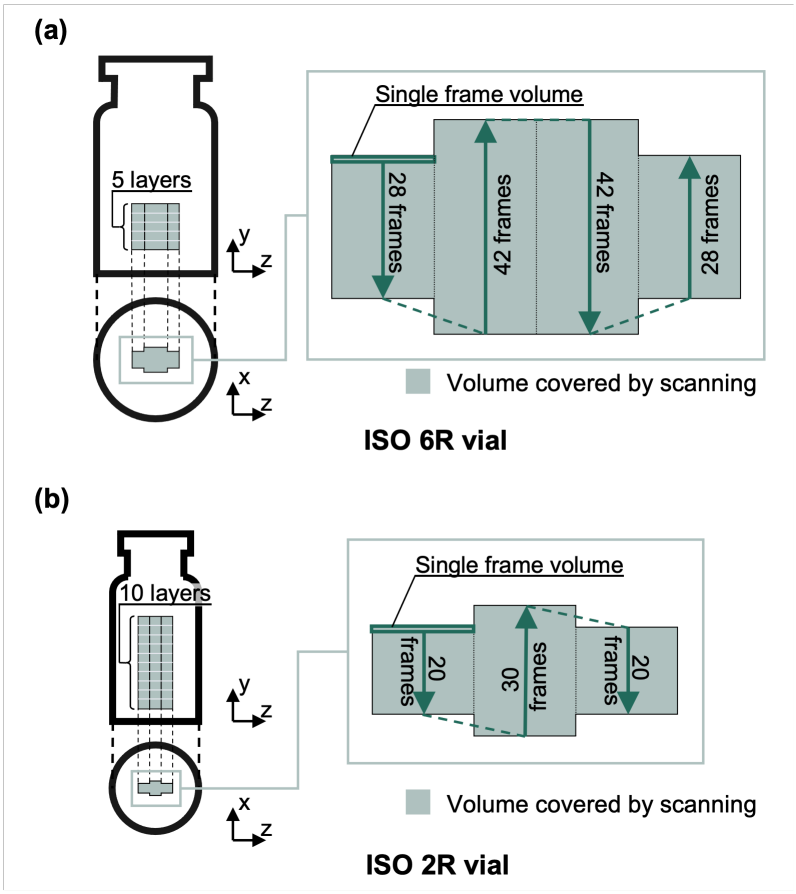


Figure 3.10: Scanning scheme of the MSLS counter. (a) Scanning scheme for ISO 6R vials. (b) Scanning scheme for ISO 2R vials.

### Fabrication of the sample housing

The sample housings used in the reported system for cylindrical aberration compensation were made of polydimethylsiloxane (PDMS) elastomer (SLYGARDTM 184). To shape the sample housing, a mold including an Amac plastic box, a target drug container, and a 3D printed container stand was developed, as shown in Fig.3.11(a1-2). The container stand was necessary during the fabrication for 1) keeping the drug container at the center of the Amac box, and 2) producing a neat surface by simply peeling off the cured PDMS instead of physically cutting the cured PDMS. The thoroughly mixed PDMS elastomer components (10:1) were poured into the corresponding molds, de-aired, cured at 65C for 24h and then demolded from the molds. The demolded end products for ISO 6R vials and ISO 2R vials were demonstrated in Fig.3.11(c1-2).

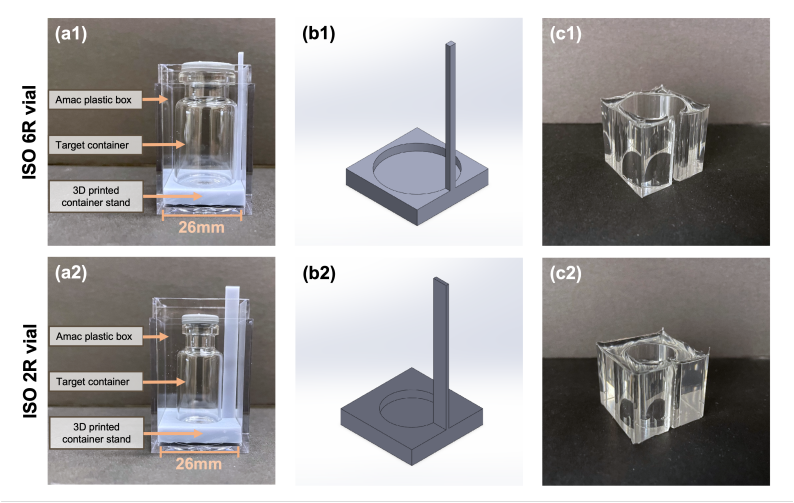


Figure 3.11: Molds for sample housing fabrication. (a) Sample holder molds for (a1) ISO 6R vials and (a2) ISO 2R vials. (b) 3D drawings of container stand for (b1) ISO 6R vials and (b2) ISO 2R vials. (c) Demolded sample housings for (c1) ISO 6R vials and (c2) ISO 2R vials.

### Optical system diagram for ray tracing

We used RayLab to simulate the light propagation from a point source buried at the center of a vial to the image plane. We simplified our microscope as an imaging system with both the objective lens and the tube lens being the same, resulting in a 1x magnification. The NA of the entire system was set to be 0.25, matching the objective lens in our MSLS system. The vial was assumed to be filled with water (refractive index: 1.33). The ISO 6R vial and ISO 2R vial situations are demonstrated in Fig.3.12.

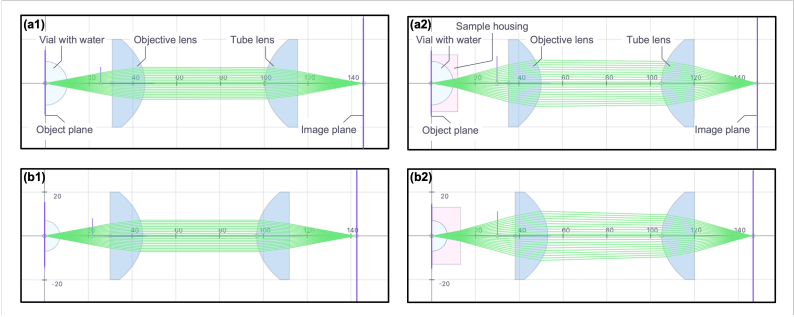


Figure 3.12: Optical path diagram used for simulation. (a) Diagram of ISO 6R vial situations, including (a1) situation without sample housing, and (a2) situation with sample housing. (b) Diagram of ISO 2R vial situations, including (b1) situation without sample housing, and (b2) situation with sample housing. Unit: mm.

**Calculation of the size – scattering reading curve**

The scenario of our particle scattering problem is demonstrated in Fig.3.4(c) (Section 3.2). We approximate the incident light as linear polarized monochromatic plane wave with wavelength of $\lambda$. The direction of the incident light is along $z$ axis, forward direction. The scattering particle is a sphere with radius of a and refractive index (RI) of $n_p$, surrounded by medium with refractive index of $n_m$. The detector is on $x$ axis facing the particle.

We use Mie theory for our calculations [27]. For clarity, we first present the functions and polynomials used in the calculation, including Bessel functions of the first and second kind $J_\nu$ and $Y_\nu$, spherical Bessel functions:

$$j_n(\rho) = \sqrt{\frac{\pi}{2\rho}} J_{n+\frac{1}{2}}(\rho) \tag{3.8}$$

$$y_n(\rho) = \sqrt{\frac{\pi}{2\rho}} Y_{n+\frac{1}{2}}(\rho), \tag{3.9}$$

spherical Hankel functions:

$$h_n^{(1)}(\rho) = j_n(\rho) + i y_n(\rho) \tag{3.10}$$

$$h_n^{(2)}(\rho) = j_n(\rho) - i y_n(\rho), \tag{3.11}$$

Riccati-Bessel functions:

$$\psi_n(\rho) = \rho j_n(\rho) \tag{3.12}$$

$$\xi_n(\rho) = \rho h_n^{(1)}(\rho), \tag{3.13}$$

and associated Legendre Functions $P_n^m$.

The particle size parameter $x$ and the particle relative refractive index $m$ are defined as follows for later use:

$$x = \frac{2\pi n_m a}{\lambda} \tag{3.14}$$

$$m = \frac{n_p}{n_m}. \tag{3.15}$$

For convenience the angle-dependent functions are defined as follows:

$$\pi_n = \frac{P_n^1}{\sin\theta} \tag{3.16}$$

$$\tau_n = \frac{dP_n^1}{d\theta}. \tag{3.17}$$

The relation between incident and scattered field is described as:

$$\begin{pmatrix} E_{\parallel s} \\ E_{\perp s} \end{pmatrix} = \frac{e^{ik(r-z)}}{-ikr} \begin{pmatrix} S_2 & 0 \\ 0 & S_1 \end{pmatrix} \begin{pmatrix} E_{\parallel i} \\ E_{\perp i} \end{pmatrix} \tag{3.18}$$

where $\begin{pmatrix} E_{\parallel s} \\ E_{\perp s} \end{pmatrix}$ is the scattered field, $\begin{pmatrix} E_{\parallel i} \\ E_{\perp i} \end{pmatrix}$ is the incident field and $S_j (j = 1, 2)$ are elements of amplitude scattering matrix depending on the scattering angle $\theta$ and the azimuthal angle $\varphi$. Here we clarify specifically that $\begin{pmatrix} E_{\parallel s} \\ E_{\perp s} \end{pmatrix}$ and $\begin{pmatrix} E_{\parallel i} \\ E_{\perp i} \end{pmatrix}$ are based on different sets of basis vectors $\begin{pmatrix} \vec{e}_{\parallel s} \\ \vec{e}_{\perp s} \end{pmatrix}$ and $\begin{pmatrix} \vec{e}_{\parallel i} \\ \vec{e}_{\perp i} \end{pmatrix}$ , which are clarified in [27].

The amplitude scattering matrix elements are given by:

$$S_1 = \sum_n \frac{2n_+1}{n(n+1)} (a_n \pi_n + b_n \tau_n) \tag{3.19}$$

$$S_2 = \sum_n \frac{2n_+1}{n(n+1)} (a_n \tau_n + b_n \pi_n). \tag{3.20}$$

Here $a_n$ and $b_n$ are scattering coefficients:

$$a_n = \frac{m\psi_n(mx)\psi_n'(x) - \psi_n(x)\psi_n'(mx)}{m\psi_n(mx)\xi_n'(x) - \xi_n(x)\psi_n'(mx)} \tag{3.21}$$

$$b_n = \frac{\psi_n(mx)\psi_n'(x) - m\psi_n(x)\psi_n'(mx)}{\psi_n(mx)\xi_n'(x) - m\xi_n(x)\psi_n'(mx)} \tag{3.22}$$

where $x$, $m$, $\psi_n$ and $\xi_n$ are size parameter, relative refractive index and Riccati-Bessel functions clarified previously. In actual computation, the algorithm terminates after $N_{stop}$ terms. The criterion for $N_{stop}$ is as follows, considering both computational efficiency and sufficient convergence [27]:

$$N_{stop} = \lceil x + 4x^{1/3} + 2 \rceil. \tag{3.23}$$

In our case only scattered energy that could reach the detector is considered when calculating the particle scattering cross section. The receiving range of the detection, determined by objective NA in our system, is expressed as solid angle $S$ in Fig.3.4(c) (section 3.2). The particle scattering cross section is then calculated as follows:

$$C_{sca} = \int_S \frac{(S_2 \cos\varphi)^2 + (S_1 \sin\varphi)^2}{(2\pi/\lambda)^2} d\Omega. \tag{3.24}$$

The energy scattering rate $W_sca$ by the particle can be determined from the scattering cross section:

$$W_{sca} = C_{sca} I_i \tag{3.25}$$

where $I_i$ is the incident intensity.

The scattering reading ($SC$) of the particle can then be determined from energy scattering rate $W_sca$ and the system parameters including the camera exposure time $t$, the camera sensor quantum efficiency $QE$ ,and the camera sensor conversion factor $CF$:

$$SC = \frac{W_{sca}t}{hc/\lambda} \times QE \times CF \tag{3.26}$$

where $h$ is the Planck constant and $c$ is the speed of light in air.

The $SC$-particle size curve in Fig.3.4(c) (section 3.2) was generated by calculating the $SC$ values of particles with diameter ranging from 0.8 $\mu$m to 50 $\mu$m. All parameters used in actual computation were summarized in Table.3.3.

| Parameter | Particle RI ($n_p$) | Medium RI ($n_m$) | Objective NA | Wavelength ($\lambda$) |
|---|---|---|---|---|
| Value | 1.59 | 1.33 | 0.25 | 532nm |
| Parameter | Incident intensity ($I_i$) | Exposure time ($t$) | Quantum Efficiency ($QE$) | Conversion factor ($CF$) |
| Value | 3.66 $W/cm^2$ | 20 ms | 0.6 | 0.46 |

Table 3.3: Parameters used in size – $SC$ curve calculation.

**Particle imprint aspect ratio determination**

As presented in Fig.3.13, we performed normalized autocorrelation to the captured light sheet image and the aspect ratio of the main peak of the autocorrelation map was used to represent the aspect ratio of the particle imprints. We determined the aspect ratio of the main autocorrelation peak as follows: 1) Binary thresholding the normalized autocorrelation map (threshold = 0.7) and 2) Dividing the height of the remaining blob with the width of the blob.

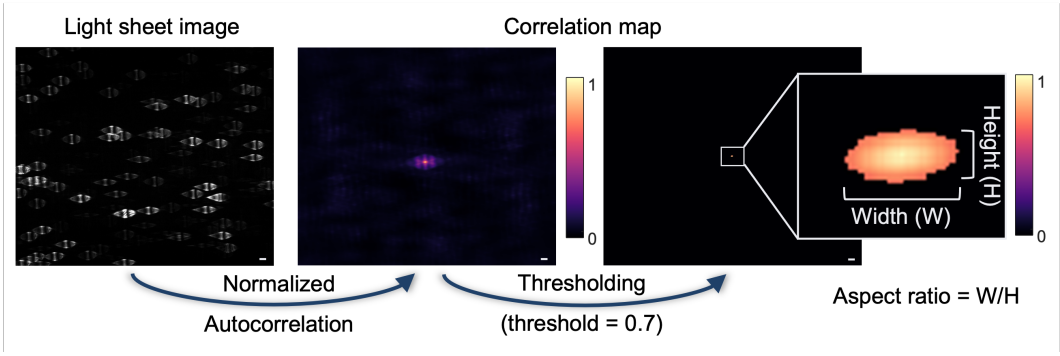


Figure 3.13: Particle imprint aspect ratio determination process. Scale bar: 50 $\mu$m.

**Particle imprint aspect ratio – axial position curve**

We measured the particle imprint aspect ratios under varied axial positions for both ISO 6R vial and ISO 2R vial. The axial positions covered range from -60 $\mu$m to 60 $\mu$m with step of 10 $\mu$m (along x-axis in our setup). At each axial position, 10 measurements were taken and averaged as a final data point. Both experimental measurements and linear fitting were showed in Fig.3.14.

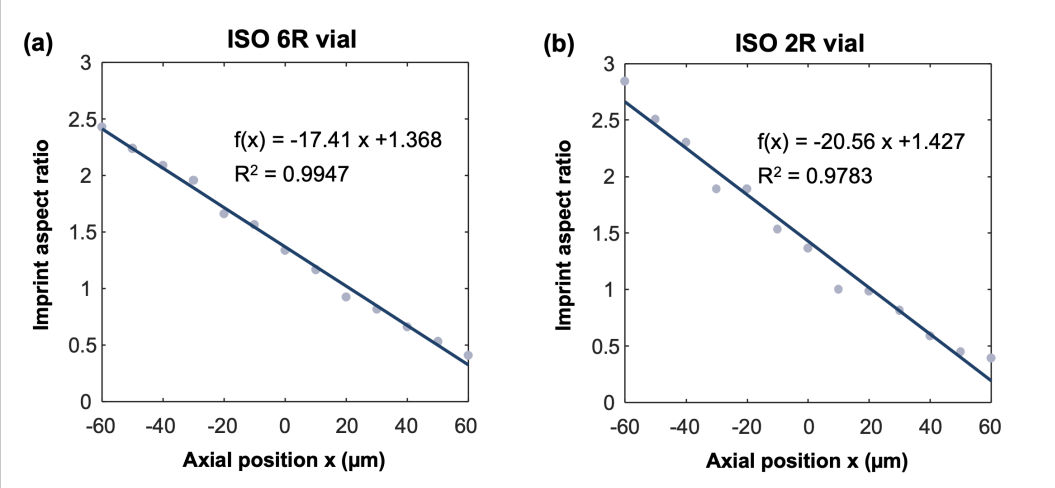


Figure 3.14: Particle imprint aspect ratio – axial position curve. (a) ISO 6R vial measurements and corresponding linear fitting. (b) ISO 2R vial measurements and corresponding linear fitting.

**Sampling volume and sampling confidence level**

The goal of this section is to determine the number of shots $N$ given the concentration to be estimated $c$, target margin error $e$ and target confidence interval $CI$. Before delving into this problem, we define more parameters here for convenience. Specifically, the total volume of the suspension to be tested is $v_total$, the sampled volume during a single shot is $v_ss$ and the number of particles captured in a single shot is $n_ss$.

Two assumptions are made in our calculation: 1) The probability of a particle showing up at a certain position is uniform within the suspension to be tested. 2) The particles are independent in the suspension to be tested.

The total number of particles within the suspension, denoted as $n_total$, is:

$$n_{total} = c \cdot v_{total}. \tag{3.27}$$

The process of a particle being recorded by a single shot is a Bernoulli event and its

probability, denoted as $p_ss$, can be expressed as follows:

$$p_{ss} = \frac{v_{ss}}{v_{total}}. \tag{3.28}$$

Considering the above process for all particles within the suspension, when $n_total$ is large enough and $p_ss$ is small enough, the number of particles captured in a single shot, denoted as $n_ss$, will follow Poisson distribution:

$$n_{ss} \sim Poisson(\lambda = n_{total} \cdot p_{ss}) \tag{3.29}$$

and the $\lambda$ of this Poisson distribution can be further written as:

$$\lambda = n_{total} \cdot \frac{v_{ss}}{v_{total}} = c \cdot v_{ss}. \tag{3.30}$$

A light-sheet microscope capturing process with $N$ shots can be modeled as sampling the $n_ss$ for $N$ times. According to Central Limit Theorem, the distribution of the mean of the $n_ss$ is approximately a normal distribution:

$$\overline{n_{ss}} \sim \mathcal{N}(c \cdot v_{ss}, \frac{\sqrt{c \cdot v_{ss}}}{\sqrt{N}}). \tag{3.31}$$

To ensure that the $CI$ confidence interval (corresponding z score denoted as $Z$) have certain margin of error $e$, the required shot number $N$ can be calculated as follows:

$$\frac{Z \cdot \sqrt{c \cdot v_{ss}}}{\sqrt{N}} = e \tag{3.32}$$

$$N = \frac{Z^2}{e^2} c \cdot v_{ss}. \tag{3.33}$$

In our particle counting application, it is reasonable to choose the confidence interval to be 90% and the margin of error to be ±15% ($c \cdot v_{ss}$). And the volume of the single shot can be determined based on our illumination light sheet cross section profile, which is demonstrated in section 3.2. The required shot numbers $N$s of our reported system for target concentrations that typically encountered in pharmaceutical production are listed in Table.3.4.

| Target concentration $c$ (particle/ml) | Required shot number $N$ |
|---|---|
| 1e2 | 3231 |
| 5e2 | 646 |
| 1e3 | 323 |
| 5e3 | 65 |
| 1e4 | 32 |
| 5e4 | 6 |
| 1e5 | 3 |
| 5e5 | 1 |

Table 3.4: Numbers of shots required by varied target concentration.

**Particle imprint overlapping simulation**

The simulation was modeled as follows: each simulated image had a certain number of particles imprints. The number of the particle imprints was determined by multiplying the simulated particle concentration with the sampling volume of a single frame. The shape of the particle imprints was simplified as circles with diameter of 70 $\mu$m. The positions of the particle imprints were independent between each other and followed uniform distribution. The overlap coefficient ($\gamma$) was defined as:

$$\gamma = \frac{Pixel\#(coveredbymorethanoneparticleimprints)}{Pixel\#(coveredbyparticleimprints)}. \tag{3.34}$$

The simulation covered concentration from 5e4 particle/ml to 5e5 particle/ml with step of 5e4 particle/ml. For each concentration, 100 trials were performed and averaged $\gamma$ was taken. The $\gamma$ – concentration plot was showed in Fig.3.15.

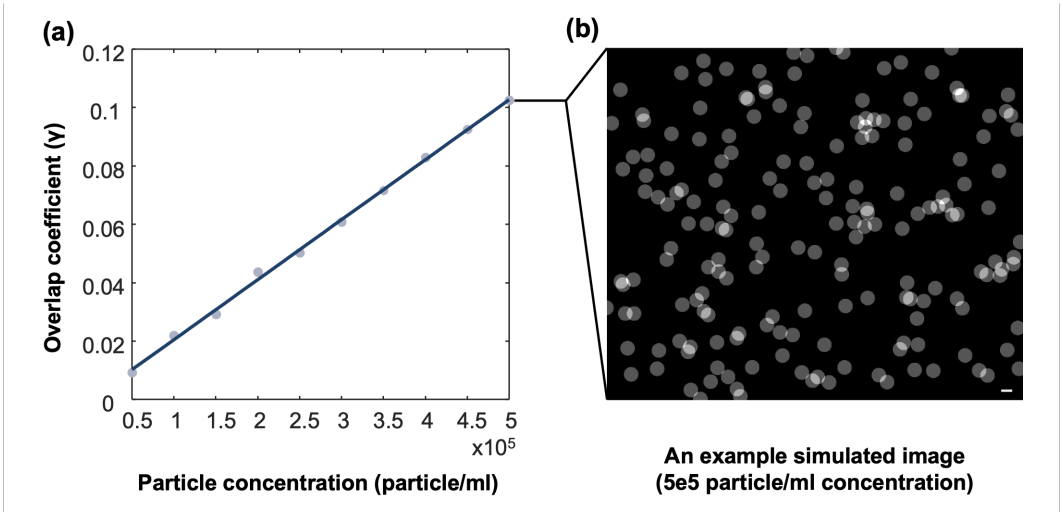


Figure 3.15: Particle imprints overlapping simulation. (a) Particle concentration - $\gamma$ plot. (b) An example image at concentration of 5e5 particle/ml. Scale bar: 50 $\mu$m.

## References


[1] John F. Carpenter et al. "Overlooking subvisible particles in therapeutic protein products: Gaps that may compromise product quality." In: *Journal of Pharmaceutical Sciences* 98.4 (2009), pp. 1201–1205. ISSN: 0022-3549. DOI: https://doi.org/10.1002/jps.21530. URL: https://www.sciencedirect.com/science/article/pii/S0022354916329367.

[2] Linda O. Narhi et al. "Subvisible (2-100$\mu$m) particle analysis during biotherapeutic drug product development: Part 1, considerations and strategy." In: *Journal of Pharmaceutical Sciences* 104.6 (2015), pp. 1899–1908. ISSN: 0022-3549. DOI: https://doi.org/10.1002/jps.24437. URL: https://www.sciencedirect.com/science/article/pii/S0022354915300885.

[3] Vincent Corvari et al. "Subvisible (2–100·$\mu$m) particle analysis during biotherapeutic drug product development: Part 2, experience with the application of subvisible particle analysis." In: *Biologicals* 43.6 (2015), pp. 457–473. ISSN: 1045-1056. DOI: https://doi.org/10.1016/j.biologicals.2015.07.011. URL: https://www.sciencedirect.com/science/article/pii/S1045105615000913.

[4] Satish K. Singh et al. "An industry perspective on the monitoring of subvisible particles as a quality attribute for protein therapeutics." In: *Journal of Pharmaceutical Sciences* 99.8 (2010), pp. 3302–3321. ISSN: 0022-3549. DOI: https://doi.org/10.1002/jps.22097. URL: https://www.sciencedirect.com/science/article/pii/S0022354915325193.

[5] Renuka Thirumangalathu et al. "Silicone oil- and agitation-induced aggregation of a monoclonal antibody in aqueous solution." In: *Journal of Pharmaceutical Sciences* 98.9 (2009), pp. 3167–3181. ISSN: 0022-3549. DOI: https://doi.org/10.1002/jps.21719. URL: https://www.sciencedirect.com/science/article/pii/S0022354916330878.

[6] René Strehl et al. "Discrimination between silicone oil droplets and protein aggregates in biopharmaceuticals: A novel multiparametric image filter for sub-visible particles in microflow imaging analysis." In: *Pharmaceutical Research* 29.2 (2012), pp. 594–602. ISSN: 1573-904X. DOI: 10.1007/s11095-011-0590-7. URL: https://doi.org/10.1007/s11095-011-0590-7.

[7] Dean C. Ripple and Mariana N. Dimitrova. "Protein particles: What we know and what we do not know." In: *Journal of Pharmaceutical Sciences* 101.10 (2012), pp. 3568–3579. ISSN: 0022-3549. DOI: https://doi.org/10.1002/jps.23242. URL: https://www.sciencedirect.com/science/article/pii/S0022354915313770.

[8] Hanns-Christian Mahler et al. "Protein aggregation: Pathways, induction factors and analysis." In: *Journal of Pharmaceutical Sciences* 98.9 (2009), pp. 2909–2934. ISSN: 0022-3549. DOI: https://doi.org/10.1002/jps.

21566. URL: https://www.sciencedirect.com/science/article/pii/S0022354916330775.

[9] Marisa K. Joubert et al. "Classification and cCharacterization of therapeutic antibody aggregates." In: *Journal of Biological Chemistry* 286.28 (2011), pp. 25118–25133. ISSN: 0021-9258. DOI: https://doi.org/10.1074/jbc.M110.160457. URL: https://www.sciencedirect.com/science/article/pii/S0021925819486730.

[10] Joseph Kotarek et al. "Subvisible particle content, formulation, and dose of an erythropoietin peptide mimetic product are associated with severe adverse postmarketing events." In: *Journal of Pharmaceutical Sciences* 105.3 (2016), pp. 1023–1027. ISSN: 0022-3549. DOI: https://doi.org/10.1016/S0022-3549(15)00180-X. URL: https://www.sciencedirect.com/science/article/pii/S002235491500180X.

[11] Marisa K. Joubert et al. "Highly aggregated antibody therapeutics can enhance the in vitro innate and late-stage T-cell immune responses." In: *Journal of Biological Chemistry* 287.30 (2012), pp. 25266–25279. ISSN: 0021-9258. DOI: 10.1074/jbc.M111.330902. URL: https://doi.org/10.1074/jbc.M111.330902.

[12] Amber Haynes Fradkin, John F. Carpenter, and Theodore W. Randolph. "Immunogenicity of aggregates of recombinant human growth hormone in mouse models." In: *Journal of Pharmaceutical Sciences* 98.9 (2009), pp. 3247–3264. ISSN: 0022-3549. DOI: https://doi.org/10.1002/jps.21834. URL: https://www.sciencedirect.com/science/article/pii/S0022354916330891.

[13] "United States Pharmacopeia. General Chapter <787> Subvisible particulate matter in therapeutic protein injections." In: Rockville, MD: U.S. Pharmacopeial Convention, 2021.

[14] "United States Pharmacopeia. General Chapter <788> Particulate matter in injections." In: Rockville, MD: U.S. Pharmacopeial Convention, 2021. Chap. USP-NF, DOI: 10.31003/uspnf_m99586_02_01.

[15] "United States Pharmacopeia. General Chapter <1787> Measurement of subvisible particulate matter in therapeutic protein injections." In: Rockville, MD: U.S. Pharmacopeial Convention, 2023. DOI: 10.31003/uspnf_m7866_03_01. URL: http://dx.doi.org/10.31003/uspnf_m7866_03_01.

[16] "United States Pharmacopeia. General Chapter <1788> Methods for the determination of subvisible particulate matter." In: Rockville, MD: U.S. Pharmacopeial Convention, 2023. Chap. USP-NF, DOI: 10.31003/uspnf_m3023_02_01. URL: http://dx.doi.org/10.31003/uspnf_m3023_02_01.

[17] Sarah Zölls et al. "Particles in therapeutic protein formulations, part 1: Overview of analytical methods." In: *Journal of Pharmaceutical Sciences* 101.3 (2012), pp. 914–935. ISSN: 0022-3549. DOI: https://doi.org/10.

1002/jps.23001. URL: https://www.sciencedirect.com/science/article/pii/S0022354915316865.

[18] Satish K. Singh and Maria R. Toler. "Monitoring of subvisible particles in therapeutic proteins BT - therapeutic proteins: Methods and protocols." In: ed. by Vladimir Voynov and Justin A Caravella. Totowa, NJ: Humana Press, 2012, pp. 379–401. ISBN: 978-1-61779-921-1. DOI: 10.1007/978-1-61779-921-1_24. URL: https://doi.org/10.1007/978-1-61779-921-1_24.

[19] Linda O. Narhi et al. "A critical review of analytical methods for subvisible and visible particles." eng. In: *Current pharmaceutical biotechnology* 10.4 (2009), pp. 373–381. ISSN: 1873-4316 (Electronic). DOI: 10.2174/138920109788488905.

[20] John den Engelsman et al. "Strategies for the assessment of protein aggregates in pharmaceutical biotech product development." In: *Pharmaceutical Research* 28.4 (2011), pp. 920–933. ISSN: 1573-904X. DOI: 10.1007/s11095-010-0297-1. URL: https://doi.org/10.1007/s11095-010-0297-1.

[21] Glenn A. Wilson and Mark Cornell Manning. "Flow imaging: Moving toward best practices for subvisible particle quantitation in protein products." In: *Journal of Pharmaceutical Sciences* 102.3 (2013), pp. 1133–1134. ISSN: 0022-3549. DOI: https://doi.org/10.1002/jps.23445. URL: https://www.sciencedirect.com/science/article/pii/S0022354915311898.

[22] Deepak K. Sharma et al. "Micro-flow imaging: Flow microscopy applied to sub-visible particulate analysis in protein formulations." In: *The AAPS Journal* 12.3 (2010), pp. 455–464. ISSN: 1550-7416. DOI: 10.1208/s12248-010-9205-1. URL: https://doi.org/10.1208/s12248-010-9205-1.

[23] Christine Probst et al. "Advanced characterization of silicone oil droplets in protein therapeutics using artificial intelligence analysis of imaging flow cytometry data." In: *Journal of Pharmaceutical Sciences* 109.10 (2020), pp. 2996–3005. ISSN: 0022-3549. DOI: https://doi.org/10.1016/j.xphs.2020.07.008. URL: https://www.sciencedirect.com/science/article/pii/S0022354920303713.

[24] Henryk Mach et al. "The use of flow cytometry for the detection of subvisible particles in therapeutic protein formulations." In: *Journal of Pharmaceutical Sciences* 100.5 (2011), pp. 1671–1678. ISSN: 0022-3549. DOI: https://doi.org/10.1002/jps.22414. URL: https://www.sciencedirect.com/science/article/pii/S0022354915321651.

[25] D. Brett Ludwig et al. "Flow cytometry: A promising technique for the study of silicone oil-induced particulate formation in protein formulations." In: *Analytical Biochemistry* 410.2 (2011), pp. 191–199. ISSN: 0003-2697. DOI: https://doi.org/10.1016/j.ab.2010.12.008. URL: https://www.sciencedirect.com/science/article/pii/S0003269710007797.

[26] Roberto Brunelli. *Template matching techniques in computer vision: theory and practice.* Wiley Publishing, 2009. ISBN: 0470517069.

[27] Craig F. Bohren and Donald R. Huffman. *Absorption and scattering of light by small particles.* John Wiley & Sons, 2008.

[28] Marijn Siemons et al. "Comparing strategies for deep astigmatism-based single-molecule localization microscopy." In: *Biomedical Optics Express* 11.2 (2020), pp. 735–751. DOI: 10.1364/BOE.382023. URL: https://opg.optica.org/boe/abstract.cfm?URI=boe-11-2-735.

[29] Laura Oudjedi et al. "Astigmatic multifocus microscopy enables deep 3D super-resolved imaging." In: *Biomedical Optics Express* 7.6 (2016), pp. 2163–2173. DOI: 10.1364/BOE.7.002163. URL: https://opg.optica.org/boe/abstract.cfm?URI=boe-7-6-2163.

[30] Ignacio Izeddin et al. "PSF shaping using adaptive optics for three-dimensional single-molecule super-resolution imaging and tracking." In: *Optics Express* 20.5 (2012), pp. 4957–4967. DOI: 10.1364/OE.20.004957. URL: https://opg.optica.org/oe/abstract.cfm?URI=oe-20-5-4957.

[31] Fang Huang et al. "Ultra-high resolution 3D imaging of whole cells." In: *Cell* 166.4 (2016), pp. 1028–1040. ISSN: 0092-8674. DOI: https://doi.org/10.1016/j.cell.2016.06.016. URL: https://www.sciencedirect.com/science/article/pii/S0092867416307450.

[32] Bo Huang et al. "Three-dimensional super-resolution imaging by stochastic optical reconstruction microscopy." In: *Science* 319.5864 (2008), pp. 810–813. DOI: 10.1126/science.1153529. URL: https://doi.org/10.1126/science.1153529.

[33] Bassam Hajj, Mohamed El Beheiry, and Maxime Dahan. "PSF engineering in multifocus microscopy for increased depth volumetric imaging." In: *Biomedical Optics Express* 7.3 (2016), pp. 726–731. DOI: 10.1364/BOE.7.000726. URL: https://opg.optica.org/boe/abstract.cfm?URI=boe-7-3-726.

[34] Jack Y. Zheng and Linda J. Janis. "Influence of pH, buffer species, and storage temperature on physicochemical stability of a humanized monoclonal antibody LA298." In: *International Journal of Pharmaceutics* 308.1-2 (2006), pp. 46–51.

[35] Sarah Zölls et al. "How subvisible particles become invisible—relevance of the refractive index for protein particle analysis." In: *Journal of Pharmaceutical Sciences* 102.5 (2013), pp. 1434–1446. ISSN: 0022-3549. DOI: https://doi.org/10.1002/jps.23479. URL: https://www.sciencedirect.com/science/article/pii/S0022354915311059.

[36] Cheng Du et al. “Protection of therapeutic antibodies from visible light induced degradation: Use safe light in manufacturing and storage.” In: *European Journal of Pharmaceutics and Biopharmaceutics* 127 (2018), pp. 37–43. ISSN: 0939-6411. DOI: https://doi.org/10.1016/j.ejpb.2018.02.007. URL: https://www.sciencedirect.com/science/article/pii/S0939641117312985.

[37] Angela Lopez-del Rio et al. “Sub-visible particle classification and label consistency analysis for flow-imaging microscopy via machine learning methods.” In: *Journal of Pharmaceutical Sciences* 113.4 (2024), pp. 880–890. ISSN: 0022-3549. DOI: https://doi.org/10.1016/j.xphs.2023.10.041. URL: https://www.sciencedirect.com/science/article/pii/S0022354923004719.

*Chapter 4*

# NON-DESTRUCTIVE ANALYSIS OF SUBVISIBLE PARTICLES WITH MIE SCATTERING-BASED LIGHT SHEET TECHNOLOGY: NUMBER OF FRINGES AS AN ALTERNATIVE NOVEL SIZE INDICATOR

The nondestructive Mie scattering-based Light Sheet Technology discussed in Chapter 3 has proven effective in analyzing subvisible particles directly within drug product (DP) containers while preserving sample integrity. In the reported system, side scattering intensity (SSI) was employed as an indicator of particle size, and its effectiveness was validated using both artificial and biological samples. However, this side scattering intensity-based sizing method has several limitations, including its dependence on incident light intensity and refractive indices. In this chapter, we introduce a novel particle size indicator, the number of fringes (NoF), which can be extracted from the same images captured by the MSLS setup. The properties of NoF are characterized through simulation, and its effectiveness is demonstrated in an object detection task. Both simulation and experimental results indicate that NoF is a more robust size indicator, independent of both incident light intensity and refractive indices.

## 4.1 Feasible particle size indicators from side scattering images

The Mie scattering-based Light Sheet (MSLS) technology, as a nondestructive method for subvisible particle analysis, utilizes a light sheet microscopy structure. By compensating the astigmatism introduced by drug containers, such as syringes and vials, the system can capture light sheet images of sufficient quality for subsequent particle detection and sizing. As detailed in Chapter 3, the scattering reading, defined as the pixel-wise summation of a particle's imprint, is used to estimate particle size. The workflow is illustrated in Fig.4.1.

The workflow described above uses particle side scattering intensity as an indicator of particle size, as the scattering reading is proportional to the particle's side scattering intensity. This proportionality is determined by the camera's quantum efficiency, conversion factor, and exposure time. Using side scattering intensity as a size indicator is advantageous due to its ease of calculation and its proven effectiveness, as demonstrated in Chapter 3 Fig.3. However, this approach has several

limitations: 1) Dependency on Incident Light Intensity: Accurate particle sizing based on side scattering intensity depends on precise measurement of the incident light intensity. 2) Dependency on Particle Axial Localization: The Gaussian profile of the incident light sheet causes non-uniform illumination for particles located at different positions within the light sheet. Therefore, determining the particle's axial position is essential for accurately measuring incident light intensity. 3) Dependency on Refractive Indices: Accurate particle sizing through side scattering intensity requires precise knowledge of the refractive indices of both the particles and the surrounding medium. Furthermore, the workflow described in Chapter 3 assumes a consistent refractive index for all particles, even though they may have different compositions and, consequently, different refractive indices. This assumption can lead to inaccuracies in particle sizing. 4) Inability to Handle Overlapping Particle Imprints: When particle imprints overlap, pixel-wise summation becomes inaccurate, resulting in errors in particle sizing.

In this chapter, we introduce a novel feature extracted from particle imprints that serves as an alternative particle size indicator, termed the number of fringes (NoF) (Fig.4.1). The properties of NoF are characterized through simulations, and a deep learning-based particle detection experiment is conducted to validate its effectiveness. Both simulations and experimental results demonstrate that NoF is a robust particle size indicator that overcomes the limitations associated with the side scattering intensity-based method.

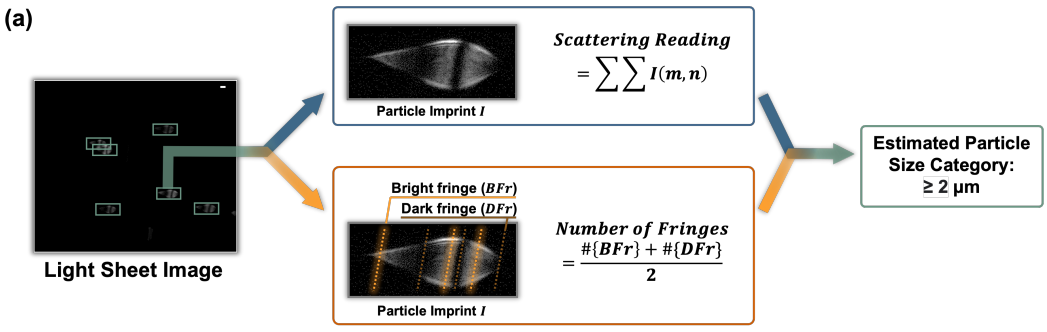


Figure 4.1: Two types of particle size indicators extracted from particle imprints. The top path describes scatter intensity-based particle sizing, while the bottom path describes NoF-based particle sizing.

## 4.2 Principle and properties of number of fringes

It has been observed that spheres have scattering light intensity that oscillates angularly [1, 2]. In our MSLS situation, such oscillation is manifested as alternating bright and dark fringes in the captured particle imprints, as demonstrated in Fig.4.1. Based on this phenomenon, we define the feature number of fringes (NoF) as the average of the number of bright fringes (#$\{BFr\}$) and the number of dark fringes (#$\{DFr\}$):

$$NoF = \frac{\#\{BFr\} + \#\{DFr\}}{2}. \tag{4.1}$$

To characterize NoF's properties as a particle size indicator, we conducted a simulation based on the scattering model described in Chapter 3. In this scenario, we approximated the incident light as a linearly polarized monochromatic plane wave and the scattering particle as a sphere. We used an illumination wavelength of 532 nm. The particle size parameter $x$ was used to describe the simulated particle size, which is defined in Equation 3.14. In this case, the particle size parameter $x$ is within the range of 15 to 390, corresponding to an actual particle size of 2 to 50 $\mu$m.

Unlike Chapter 3, which calculated the scattering light intensity collected by the objective lens, here we derived the scattering coefficient oscillation near 90 degrees and calculated the number of fringes from this oscillation (Fig.4.2). To explore NoF's sensitivity to the relative RI ($m$) determined by the particle RI ($n_p$) and surrounding medium RI ($n_m$), we simulated m values from 1.02 to 1.2 with a step size of 0.02. We grouped NoF values for each particle size under different relative refractive index conditions into a box plot. Finally, we combined box plots for different particle sizes to create Fig.4.2.

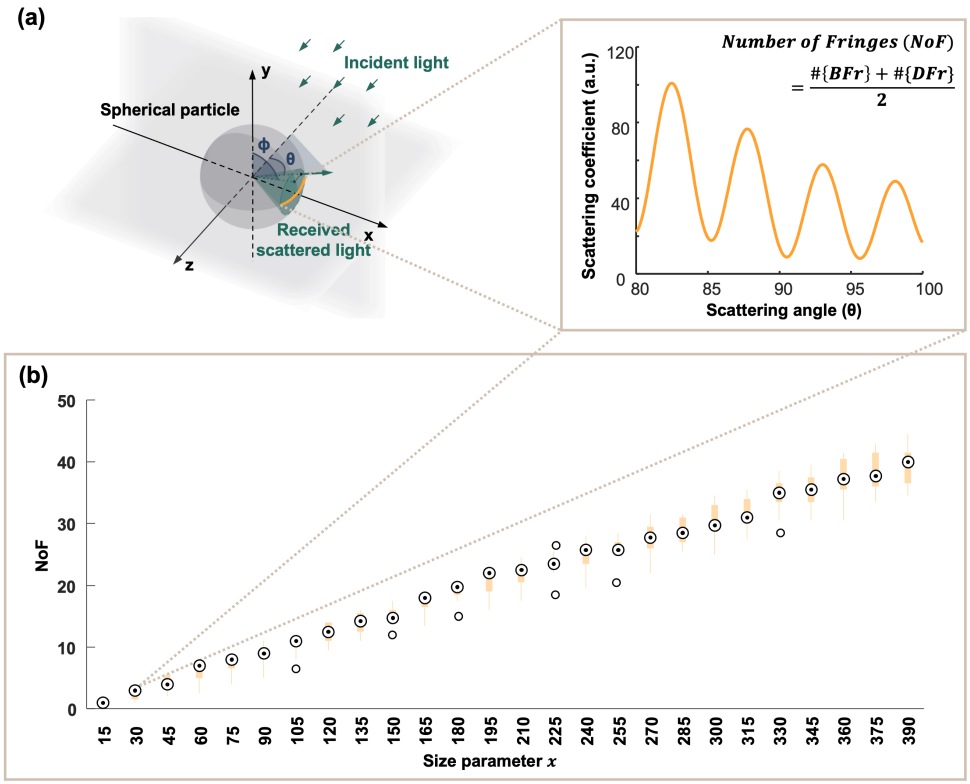


Figure 4.2: NoF characterization through simulation. (a) The simplified scattering model and NoF definition. A monochromatic plane wave scattered by a homogeneous sphere was used, and the intensity oscillation near 90° was simulated. (b) Simulation results for varied particle sizes and relative refractive indices (RI).

The simulation results have demonstrated that NoF increased monotonically with particle size growth. The relatively narrow boxes in each box plot showed that NoF is relatively robust to changes in relative refractive index. In other words, unlike scattering intensity, the NoF value does not change drastically with relative refractive index, relaxing the strong requirement for relative refractive index information in scattering intensity-based sizing situations. Both properties indicate that NoF could be a feasible particle size indicator.

An experiment was then conducted to further demonstrate NoF's properties. Four types of water suspensions with polystyrene beads of different sizes were prepared and imaged by the MSLS system. The diameters of these polystyrene beads were 3 $\mu$m, 8 $\mu$m, 15 $\mu$m, and 30 $\mu$m, each falling into one category of the UPS particle size bin: $\geq$ 2 $\mu$m, $\geq$ 5 $\mu$m, $\geq$ 10 $\mu$m, $\geq$ 25 $\mu$m. To characterize the defocus properties

of NoF, each sample was imaged at three axial locations: -100 $\mu$m, 0 $\mu$m, and 100 $\mu$m.

The imaging results are illustrated in Fig.4.3. As expected, the NoF values increased as particle size increased. The corresponding NoF values for 3 $\mu$m, 8 $\mu$m, and 15 $\mu$m polystyrene beads were 2.5, 6.5, and 12, respectively. For 30 $\mu$m polystyrene particles, the particle imprint pattern became more complicated than simple fringes, which could be explained by more modes beginning to play a part in forming the pattern. Under such situations, NoF is no longer valid.

The experiment also demonstrated another advantage of NoF: its robustness to defocusing. For all situations where particle imprints still showed fringe patterns (3 $\mu$m, 8 $\mu$m, 15 $\mu$m beads), the fringe distribution remained unchanged across varying axial locations. This means that with NoF as a particle size indicator, axial localization is no longer necessary.

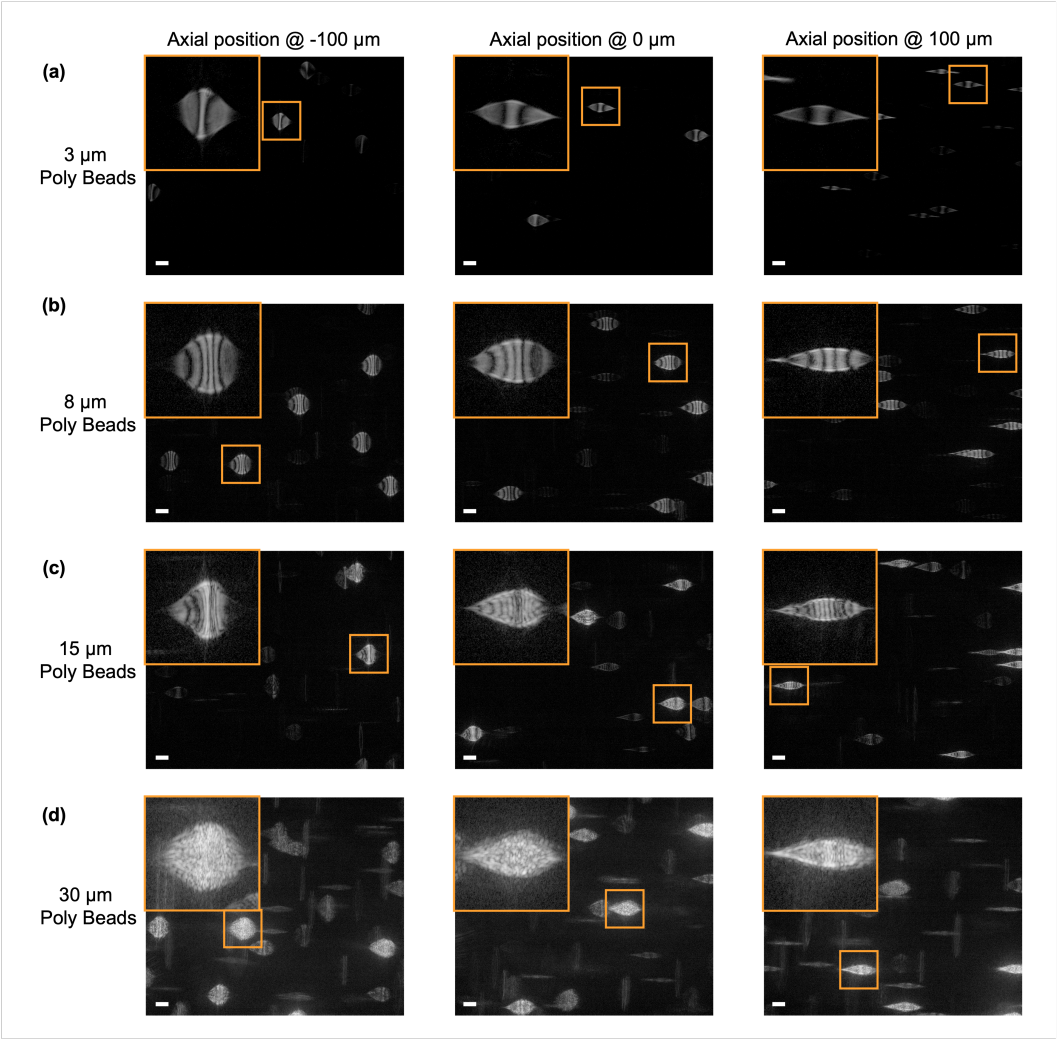


Figure 4.3: NoF characterization through experiments on (a) 3 $\mu$m polystyrene beads, (b) 8 $\mu$m polystyrene beads, (c) 15 $\mu$m polystyrene beads, and (d) 30 $\mu$m polystyrene beads.

## 4.3 Verifying the functionality of NoF through deep learning

Given the properties that NoF of particle side scattering imprints differ from size to size, and such difference is straightforward and observable directly from the light sheet images captured by the MSLS system, we believe object detection by deep learning could be an alternative easier solution to perform particle analyzing tasks, including particle detection and particle sizing, from light sheet images with better robustness. In this section, we built a dataset and trained a DNN model to perform the particle analysis task as a proof of concept.

Unlike the method in Chapter 3 that treated the two subtasks—particle detection

and particle sizing—separately, the deep learning object detection embedded both particle detection and particle sizing into one neural network and both subtasks are trained all at once. Once trained, the deep learning neural network (DNN) takes light sheet images from the MSLS system as input, boxes out all the particle imprints and assigns one of the four size classes: $\geq 2\,\mu m$, $\geq 5\,\mu m$, $\geq 10\,\mu m$, $\geq 25\,\mu m$, to each detected particle.

To acquire the light sheet images for the dataset, four vials of polystyrene bead suspensions, each representing one size class mentioned above, were prepared. The content of each suspension is illustrated in Fig.4.4(a), and the detailed particle concentrations, calculated from the labeled product concentrations and the dilution factors, are listed in Table.4.1. The sample vials were imaged by the MSLS system at different axial locations from -100 $\mu m$ to 100 $\mu m$. A log operator was applied to the captured images to reduce their dynamic range, ensuring that particles with both strong and weak side scattering could be visible to the DNN model.

| Sample Class | Particle | Concentration (particle/ml) |
|---|---|---|
| $\geq 2\mu m$ | 3 $\mu m$ | 0.99e4 |
| $\geq 5\mu m$ | 5 $\mu m$ | 0.99e4 |
| | 8 $\mu m$ | 1.04e4 |
| | 10 $\mu m$ | 1.01e4 |
| $\geq 10\mu m$ | 12 $\mu m$ | 3.00e3 |
| | 15 $\mu m$ | 2.99e3 |
| | 18 $\mu m$ | 2.99e3 |
| | 20 $\mu m$ | 3.01e3 |
| | 24 $\mu m$ | 2.99e3 |
| $\geq 25\mu m$ | 30 $\mu m$ | 1.00e3 |
| | 50 $\mu m$ | 1.00e3 |
| | 70 $\mu m$ | 1.00e3 |
| | 90 $\mu m$ | 1.00e3 |
| | 100 $\mu m$ | 1.00e3 |

Table 4.1: Table of samples representing various particle size classes.

After image acquisition, human annotations, including both marking the bounding boxes and assigning the particle size classes, were performed (Fig.4.4(a)). The final dataset, illustrated in Fig.4.4(b), consists of a training dataset with 4469 particles and a test dataset with 1259 particles. Both training and testing datasets have particles distributed relatively uniformly across all four size classes.

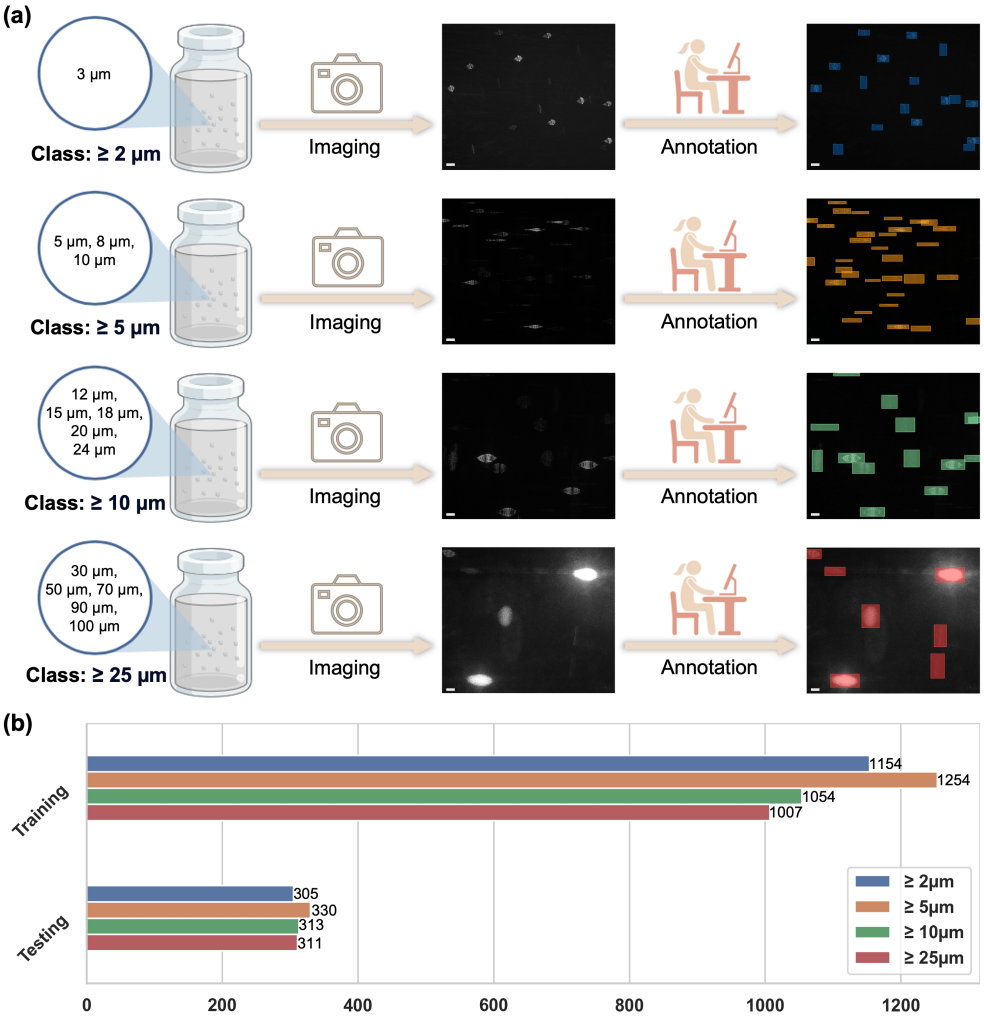


Figure 4.4: Sample preparation and dataset construction. (a) The pipeline for building the dataset, including sample preparation, data collection, and annotation. (b) Statistical analysis of the dataset, showing the relatively balanced distribution across all four size classes.

Region-based convolutional neural networks (R-CNN) have become popular for object detection tasks since their invention [3–10]. An R-CNN network performs region proposal, feature extraction, and classification and localization. As one of the improved versions of R-CNN, Faster R-CNN [7] incorporates a region proposal network (RPN) and classification into a single network by sharing the convolutional features. In this way, nearly cost-free and high-quality region proposals are enabled, and the runtime is reduced.

Here, we performed transfer learning in our particle analysis task by fine-tuning an

aforementioned Faster R-CNN model with our custom particle dataset mentioned above. The specific model has the backbone of ResNeXt-101 [11] pre-trained on ImageNet [12]. The hyperparameter settings for training this network are listed in Table.4.2.

| | |
|---|---|
| Images per batch | 4 |
| Base learning rate | 0.0005 |
| Max iteration | 2000 |
| Test score threshold | 0.4 |
| Test NMS threshold | 0.2 |

Table 4.2: Hyperparameter settings for training the DNN model.

The prediction results on the test dataset in Fig.4.5 showed the model's capability on the particle analysis task. Four examples of the model's predictions are shown in Fig.4.5. The predictions indicated that the model could provide reasonable particle detections and relatively accurate particle classifications for all 4 size classes. Furthermore, the model could handle even complicated situations such as particles located at multiple focal planes (Fig.4.5(b)), particle imprints overlapping (Fig.4.5(b)), and extra image background generated by either unexpected stray light or extremely out-of-focus particle scattering (Fig.4.5(d)).

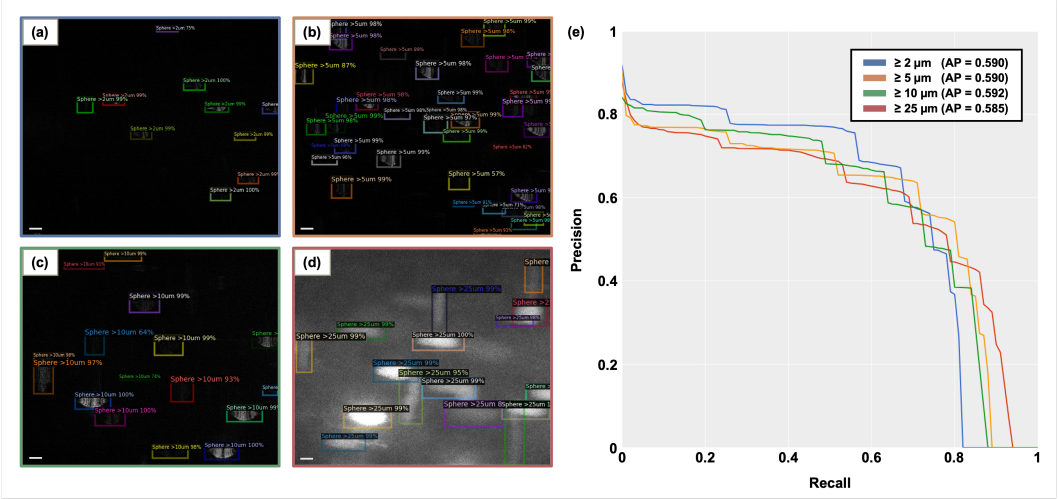


Figure 4.5: Experimental set up and general process. (a) Schematic of experimental set up. (b) Experiment procedures: One group of raw data was used for illumination correction first. Calibrated illumination angles were then used for FPM rendering.

COCO evaluation metrics [13] were used to quantitatively assess the particle analysis

model's performance. The precision-recall curve is illustrated in Fig.4.5. The average precision (AP) for the 4 size classes ($\geq 2\mu m$, $\geq 5\mu m$, $\geq 10\mu m$, $\geq 25\mu m$) are correspondingly 0.590, 0.590, 0.592, and 0.585, showing the particle analysis model to be a good detector from an empirical perspective.

## 4.4 Discussion of advantages and limitations

In this study, we discovered an alternative particle size indicator apart from side scattering intensity, named number of fringes (NoF). Both simulations and experiments were performed to characterize NoF's properties of monotonic increasing with particle size, robustness over relative refractive index, and robustness over defocusing. A particle analysis deep learning experiment was conducted as a proof of concept. The particle analysis model achieved ~0.59 average precision for all 4 size classes, proving the effectiveness of NoF as a particle size indicator.

As an alternative particle size indicator to side scattering intensity (SSI), NoF inherits the same non-destructive advantage. Moreover, NoF as a particle size indicator possesses several advantages that could overcome the limitations inherent to the SSI particle size indicator. Firstly, although SSI generally increases with particle size, it exhibits fluctuations, as shown in Fig.3.4. These fluctuations mean that a single particle reading could correspond to multiple particle sizes, reducing particle sizing accuracy. In contrast, NoF values increase monotonically with particle size, as demonstrated in Fig.4.2, making particle size determination more precise from the particle imprints.

NoF is also independent of incident light intensity. This independence eliminates the need for incident light intensity measurement, reducing potential sizing errors caused by illumination fluctuations and decreasing transmission of frequently used sample housings. Additionally, since accurate incident light intensity is no longer required, particle localization—an essential step for obtaining accurate incident light intensity for particles at different locations within the light sheet—becomes unnecessary, thereby simplifying the data processing workflow.

Furthermore, independence from side scattering intensity makes particle sizing more resilient to extreme cases such as overlapping particle imprints and those contaminated with background stray light, both of which pose challenges to the SSI size indicator. In contrast, NoF, which relies on imprint patterns rather than exact pixel values, remains unaffected by these issues.

Another advantage of NoF is its robustness to relative refractive index. Compared to

SSI, whose value can change by orders of magnitude with varying relative refractive index, the NoF of a particle of a certain size changes by only several fringes across the range of common particle-medium combinations encountered in the pharmaceutical industry. Consequently, particle sizing errors due to inaccurate refractive index estimation can be reduced.

Furthermore, NoF-based particle sizing eliminates the need for the strong assumption used in SSI-based sizing that all particles have a single refractive index. Thus, NoF allows the system to better handle situations where particles are composed of multiple materials and, therefore, have multiple refractive indices.

It's important to note that NoF remains a coarse size indicator with a resolution of approximately 0.5 $\mu$m. This limitation stems from two factors: the inherent discreteness of NoF itself and its residual dependency on the relative refractive index. Both factors constrain NoF's ability to provide higher accuracy particle size estimation.

Another current limitation of the NoF and DNN-based particle sizing approach is its reliance on supervised learning. This methodology requires a large amount of well-annotated data, which in turn demands significant human input for preparation and labeling.

To further enhance NoF's capabilities as a particle sizing indicator, future work could focus on verifying performance using real protein samples, incorporating self-supervised and unsupervised learning techniques into particle analysis, and inferring particle morphology from scattering imprint patterns using machine learning methods. These advancements could address current limitations and expand NoF's utility in particle sizing applications across various fields, potentially leading to more accurate and efficient particle analysis methods.

## References


[1] Raffaele Ragucci, Antonio Cavaliere, and Patrizio Massoli. "Drop sizing by laser light scattring exploiting intensity angular oscillation in the mie regime." In: *Particle & Particle Systems Characterization* 7.1-4 (1990), pp. 221–225.

[2] JV Dave. "Scattering of visible light by large water spheres." In: *Applied Optics* 8.1 (1969), pp. 155–164.

[3] Matloob Khushi et al. "A comparative performance analysis of data resampling methods on imbalance medical data." In: *IEEE Access* 9 (2021), pp. 109960–109975.

[4] Ross Girshick et al. "Rich feature hierarchies for accurate object detection and semantic segmentation." In: *2014 IEEE Conference on Computer Vision and Pattern Recognition*. 2014, pp. 580–587. DOI: 10.1109/CVPR.2014.81.

[5] Ross Girshick. *Fast R-CNN*. 2015. arXiv: 1504.08083 [cs.CV]. URL: https://arxiv.org/abs/1504.08083.

[6] Kaiming He et al. "Mask R-CNN." In: *Proceedings of the IEEE International Conference on Computer Vision (ICCV)*. 2017.

[7] Shaoqing Ren et al. *Faster R-CNN: Towards real-time object detection with region proposal networks*. 2016. arXiv: 1506.01497 [cs.CV]. URL: https://arxiv.org/abs/1506.01497.

[8] Rajaram Anantharaman, Matthew Velazquez, and Yugyung Lee. "Utilizing mask R-CNN for detection and segmentation of oral diseases." In: *2018 IEEE International Conference on Bioinformatics and Biomedicine (BIBM)*. 2018, pp. 2197–2204. DOI: 10.1109/BIBM.2018.8621112.

[9] Georgia Gkioxari, Ross Girshick, and Jitendra Malik. "Contextual action recognition with R*CNN." In: *Proceedings of the IEEE International Conference on Computer Vision (ICCV)*. 2015.

[10] Xudong Sun, Pengcheng Wu, and Steven C.H. Hoi. "Face detection using deep learning: An improved faster RCNN approach." In: *Neurocomputing* 299 (2018), pp. 42–50.

[11] Saining Xie et al. *Aggregated residual transformations for deep neural networks*. 2017. arXiv: 1611.05431 [cs.CV]. URL: https://arxiv.org/abs/1611.05431.

[12] Jia Deng et al. "Imagenet: A large-scale hierarchical image database." In: *2009 IEEE Conference on Computer Vision and Pattern Recognition*. IEEE. 2009, pp. 248–255.

[13] Tsung-Yi Lin et al. *Microsoft COCO: Common objects in context*. 2015. arXiv: 1405.0312 [cs.CV]. URL: https://arxiv.org/abs/1405.0312.

*Chapter 5*

# USING DEEP LEARNING TO PREDICT SEX OF HUMAN EMBRYOS

The existence of sex differences in human pre-implantation development remains an open question, and previous attempts to address this issue using human observations have not reached a consensus. In this chapter, we utilize both manual annotation and deep learning on a database of over 500 time-lapse movies, to investigate whether birth sex influences early development. Whilst manual analysis was not able to discern any parameters associated with developmental timing that can differentiate male and female embryos, training and testing a deep learning model on these videos was able to result in a statistically significant sex prediction accuracy of 61%. Importantly, we found that the period after the 8-cell stage is critical for this prediction, indicating that minor sex differences may occur from day 3 during human embryogenesis. The study of sex differences during pre-implantation can help provide additional information to understand why embryos fail and sex ratios are skewed during in vitro fertilization. Furthermore, our research paves the way for an early, non-invasive detection tool that can be used to help address and mitigate sex-related embryogenesis defects.

## 5.1 Introduction of human pre-implantation development

Human pre-implantation development comprises the period from fertilization (at day 0) to implantation of the blastocyst into the maternal uterine wall at day 7 [1]. This process is known to involve cell fate changes and morphogenetic processes that transform the zygote into an embryo with a central cavity and three lineages: the trophectoderm, which will form the placenta; the epiblast, which will form the foetus; and the hypoblast, which will give rise to the yolk sac (Fig.5.1a). Despite our growing knowledge of mechanisms involved in early human embryogenesis, an outstanding question remains as to whether there are any sex differences during human pre-implantation development.

Sex differences have been widely observed in developmental biology, although there are many different sex-related mechanisms and the system is not evolutionarily conserved between species [2]. In the current model of sex determination during mammalian development, the presence of the SRY gene on the Y chromosome

activates a cascade of steps during gonadal development that promotes male gonad and sexual characteristic specification, whilst the lack of a Y chromosome results in female characteristics [3]. Gonadal development and SRY gene products are generally detected after pre-implantation development, but the SRY model nevertheless remains a simplification and many other sex-related mechanisms have been proposed [2, 3]. In fact, many studies have suggested that sex differences do exist in mammalian pre-implantation development, with evidence from several different species [4–6]. However, the nature and cause of these differences remains largely unclear. In humans, it has been proposed that: male embryos develop faster than female embryos [7]; female embryos are suspected to undergo earlier cavitation, although this observation has not been demonstrated in a statistically significant fashion [8]; the male embryo takes longer to develop to the blastocyst stage [9]; and there are differences in blastocyst morphology and metabolism [10, 11]. Despite these studies, no consensus has been reached as to whether and how pre-implantation embryos differ based on their sex [12].

This issue of sex differences has implications for human in vitro fertilization (IVF). Firstly, it is well known that many embryos fail during embryo transfer and less than 30% of embryos develop to live birth [13]; sex differences have been a largely ignored factor in understanding why many embryos do not succeed. Knowledge of these differences during pre-implantation can shed more light on the problem, e.g., whether implantation transfer times are not optimized for a particular sex. Moreover, in cases of known sex-related issues with embryonic development [14], early and non-invasive sex detection can allow embryologists to address or mitigate potential issues. Finally, it is also known that IVF clinics have a skewed sex ratio for live births, biased towards male embryos, for reasons that are not fully clear despite various studies [15–17]. Studying sex differences can help us understand why this is the case and whether any developmental differences need to be considered during handling to avoid a skew.

The question of whether there are sex differences in pre-implantation human development is one that is well poised to address through artificial intelligence processing. Artificial intelligence has previously been used on mammalian pre-implantation development, because of its ability to detect salient features easy for humans to miss, and because of its processing power, speed, standardisation, and non-invasiveness [18–23]. For example, several studies have been able to grade blastocyst health and predict which blastocysts will be able to implant successfully into the uterine wall,

outcompeting comparative humans [18, 19, 22]. Nevertheless, artificial intelligence has not been utilised to help understand whether there are observable differences between male and female embryos during the earliest stages of human development.

For this study, we have acquired a database of over 500 embryoscope time-lapse movies of human pre-implantation development from a collaborating clinic, each labelled with birth sex (as male or female). We first attempted to investigate whether there are any differences between male and female embryos manually by using annotations of developmental timing. In this study, we were unable to identify any timing-based parameters that can distinguish embryos based on sex. We next applied deep neural network (DNN) to the same dataset, and observed a statistically significant DNN sex prediction accuracy of 61% (statistical significance of $p < 0.05$) when the videos starting from the 8-cell stage onwards were analysed. When given the same videos, humans were unable to make meaningful predictions.

This chapter indicates that weak sex differences exist in early human embryo development, which are possible to detect from the 8-cell stage onwards by a deep neural network.

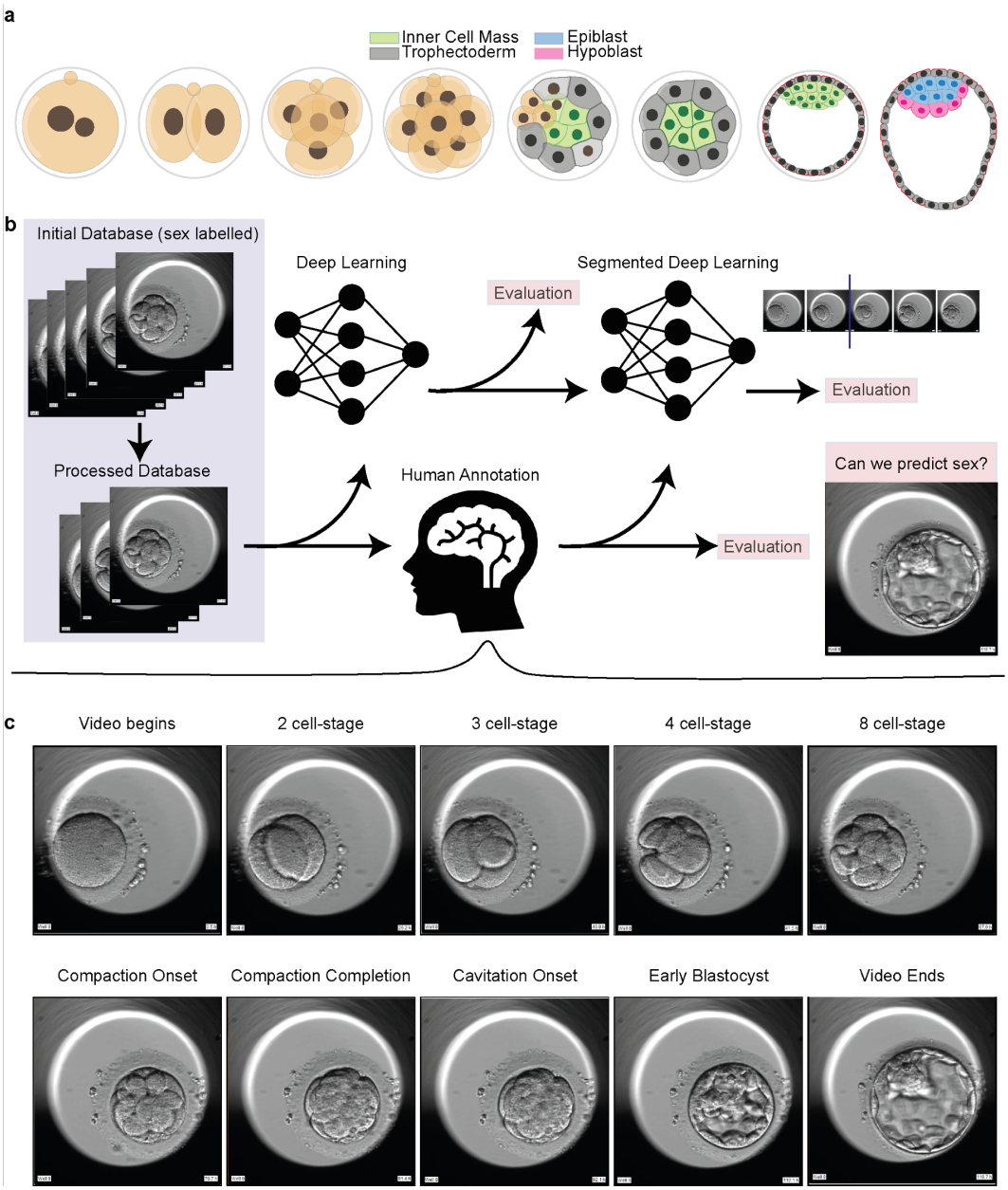


Figure 5.1: Overview of study to detect sex differences from embryoscope movies. a) Summary schematic of human pre-implantation development, from fertilisation at day 0 to implantation of the blastocyst at day 7. b) Graphical depiction of the study. A processed database of embryoscope videos is used for manual annotation and artificial intelligence processing to distinguish sex differences. Both methods are combined in deep learning that is segmented by annotated time periods, and the final deep learning models are evaluated on the ability to predict sex from unlabelled recordings. c) Depiction of the different time points used during manual annotation, with corresponding embryoscope snapshot. Alt text: Graphic depiction of study plan, including human embryo development phases.

## 5.2 Developing a database of human embryoscope movies for sex prediction

### Data collection and screening

To investigate potential sex differences in human pre-implantation development, a large database of human pre-implantation movies annotated with birth sex is needed. Embryo videos were collected from the Clinical Embryology Laboratory at IVIRMA Valencia, whose work is approved by National Commission of Human Reproduction (CNRHA) and complies with Spanish law on assisted reproductive technologies (14/2006). No human embryos were manipulated specifically for this study. We obtained more than 854 embryoscope movies from a collaborating clinic. These movies were of fresh zygotes donated for IVF, which were eventually transferred and resulted in a live birth with known sex. The pre-implantation period was recorded on video for IVF selection, with bright-field vision of a single focal plane visible using the standard embryoscope settings (Fig.5.1b) with a snapshot of the embryo every 20 minutes. Using these videos, it is possible to conduct both manual and artificial intelligence-based analyses to investigate sex differences, and ultimately test these approaches using prediction on unknown videos (Fig.5.1b). The dataset of movies was filtered for format, processing, and embryo health issues. The entier data screening process is illustrated in Fig.5.2. From the initial set of 854 videos capturing fresh oocytes that led to live births, 580 videos were retained after excluding those with issues related to format, processing errors, or embryo quality. Of these, 515 videos were subsequently utilized for deep learning model training and testing.

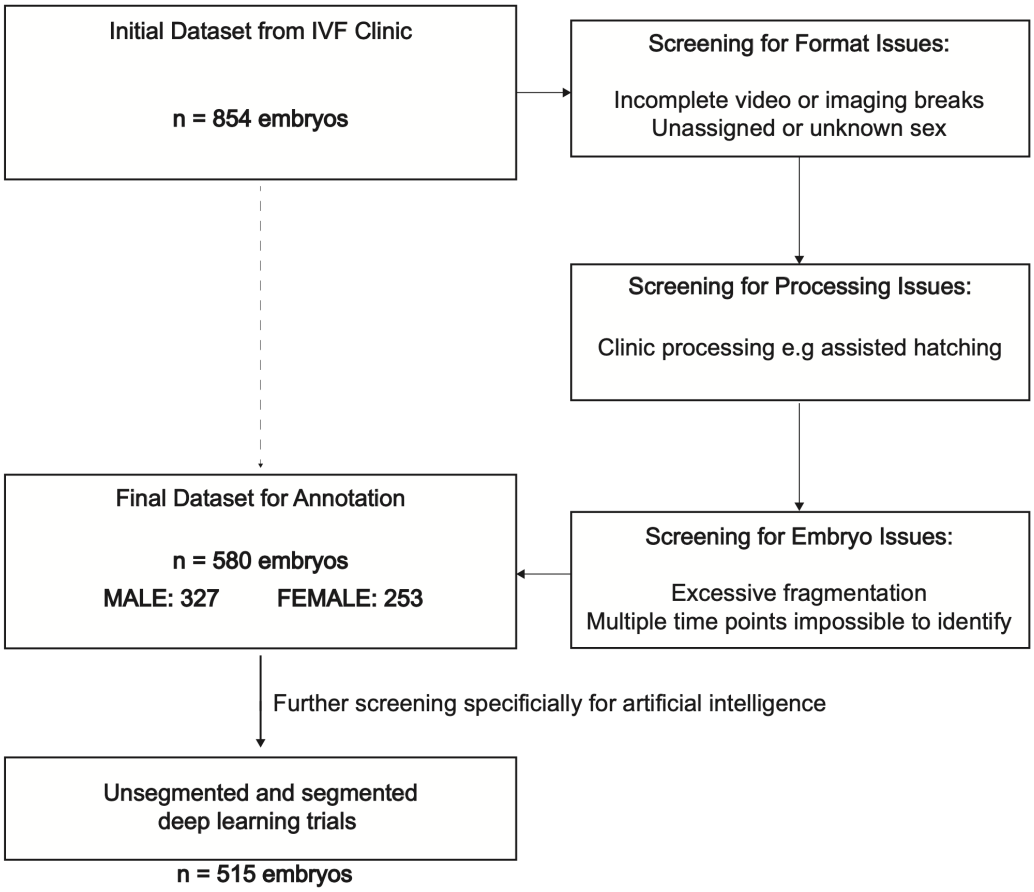


Figure 5.2: Data screening of embryoscope video database. The initial dataset from the collaborating clinic was processed before finally being used for annotation and deep learning. Out of 854 videos initially which were from fresh oocytes transferred and resulting in live births, 580 were left after videos with format, processing and embryo issues were excluded. Out of these, 515 were used for deep learning training and testing.

Data imbalance between classes, commonly seen in real-world datasets [24–27], was also observed in our dataset (Fig.5.2), with more males than females. Oversampling the minority class, a method established for decades, has been shown to be effective in addressing the class imbalance issue [28–30]. Compared with its alternative strategy, undersampling, oversampling has the advantage of avoiding data loss and making full use of the entire dataset. In our artificial intelligence-based analyses, we applied the same oversampling technique by randomly duplicating female videos so that the training set included equal numbers of males and females, as elaborated in the later sections.

**Manual annotation**

The following parameters were evaluated from the embryoscope videos (please also see corresponding images in Fig.5.1): Time reaching 2-cell: First moment where there are two distinct cells.

Time reaching 3-cell: First moment where there are three distinct cells.

Time reaching 4-cell: First moment where there are four distinct cells.

Time reaching 5-cell: First moment where there are five distinct cells.

Time reaching 8-cell: First moment where there are eight distinct cells.

Compaction onset: First moment where a visible inter-blastomere angle begins to increase.

Compaction completion: First moment where all the inter-blastomere angles stop increasing.

Cavitation onset: First moment where a cavitation nucleation site (initial spot) is visible, and later results in a formed cavity.

Early blastocyst: First moment when the blastocoel cavity takes up half of the total embryo volume.

## 5.3 Manual analysis of developmental timing cannot separate male and female embryos

The first part of this study involved manual analysis of the embryoscope recordings, aiming to find parameters that can distinguish male and female embryos. After filtering, 580 embryos were used for manual analysis annotation. Given the nature of the embryoscope recordings, we were able to assess parameters associated with developmental timing such as development to the 2-cell stage or the onset of cavitation, using the criteria outlined in 5.2 (Fig.5.1c). The videos were annotated sex-blind for all parameters. Then, after sorting the annotations into male and female groups, various time periods were calculated from the annotations and were compared for sex differences for the difference between means. The data was analysed as follows: the fit of the data to a normal distribution was analysed with D'Agostino's K-squared test. If data fit a normal distribution, then for comparison of two or multiple samples, an unpaired or paired two-tailed student's t test (two experimental groups) or a one-way ANOVA test (more than two experimental groups) was used to analyse statistical significance, depending on the fit of the data to the test

assumptions. Differences in variances were accounted for by performing a Welch's correction where appropriate. For data that did not display a normal distribution, a Mann–Whitney U-test (for two experimental groups) or a Kruskal–Wallis test with a Dunn's multiple comparison test (for more than two experimental groups) was used to test statistical significance. To determine the influence of different groups in multiple variants, a two-way ANOVA was performed. Statistical analyses were performed using the Graphpad Prism software (http://www.graphpad.com).

Selected examples are graphically displayed in Fig.5.3. And the p-values for all individual comparisons are listed in Table.5.1). We found that no period during pre-implantation showed any strong difference in timing between male and female embryos compared to the variability found within each group, and this was reflected in the p-value of all comparisons being statistically insignificant. Thus, we concluded that manual annotation of timing parameters is not a sensitive enough technique to elucidate sex differences between male and female embryos that may exist.

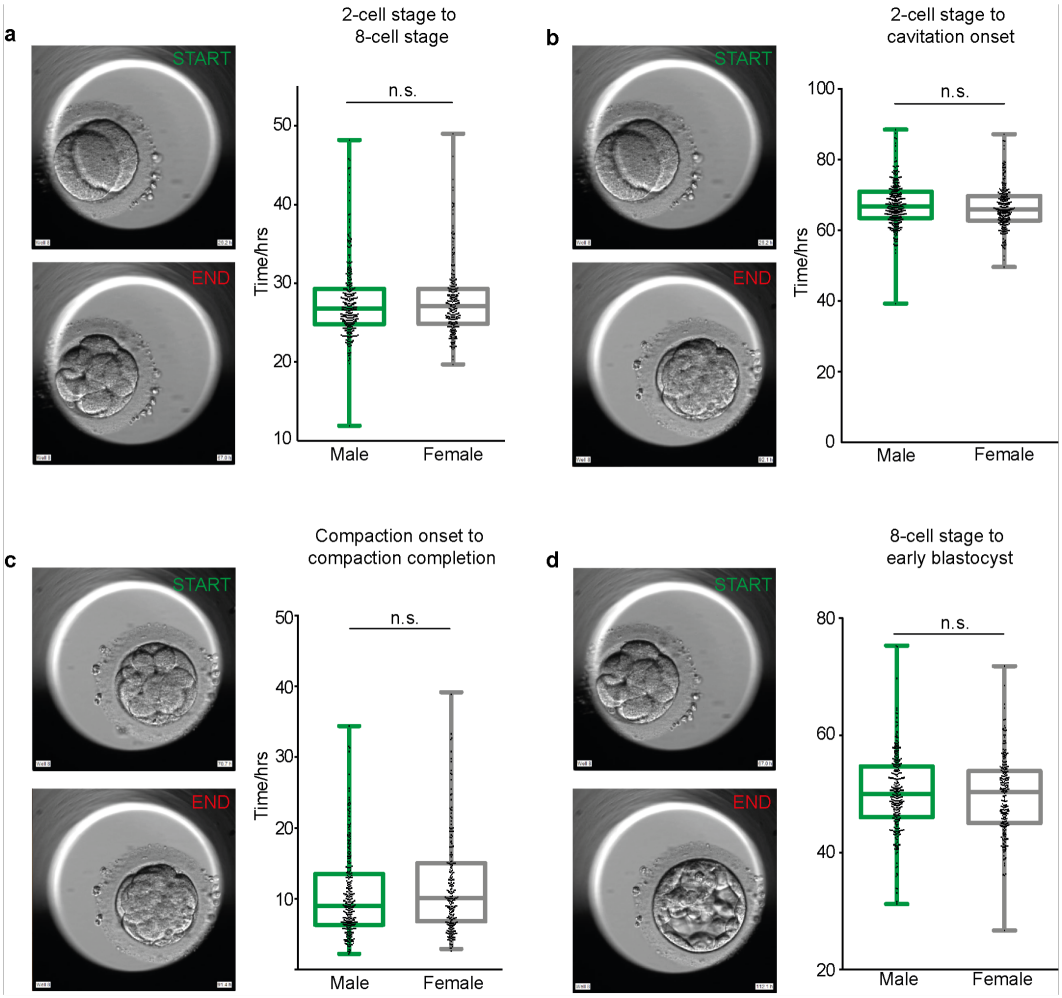


Figure 5.3: Manual annotation does not reveal sex differences in developmental timing. Comparison of different annotated time periods during pre-implantation development, between male and female embryos. Box-and-whisker plot of annotated periods presented with statistical test and corresponding snapshots of start and end of period, from embryoscope movies. a) No significant difference between male and female embryos from the 2-cell stage to 8-cell stage during pre-implantation development, two-tailed t-test, $p>0.05$. b) No significant difference between male and female embryos from the 2-cell stage to cavitation onset, two-tailed t-test, $p>0.05$. c) No significant difference between male and female embryos from compaction onset to compaction completion during pre-implantation development, two-tailed t-test, $p>0.05$. d) No significant difference between male and female embryos from the 8-cell stage to early blastocyst, two-tailed t-test, $p>0.05$. Alt text: Statistical comparison between male and female embryos for manually annotated timepoints.

| Starting Time Point (Annotated) | Ending Time Point (Annotated) | Unadjusted P-Value (Sex Comparison) *N* |
|---|---|---|
| 2-cell stage | 4-cell stage | 0.47 |
| 2-cell stage | 8-cell stage | 0.79 |
| 2-cell stage | cavitation onset | 0.09 |
| 2-cell stage | early blastocyst | 0.49 |
| 8-cell stage | compaction completion | 0.77 |
| 8-cell stage | cavitation onset | 0.70 |
| 8-cell stage | early blastocyst | 0.15 |
| compaction onset | compaction completion | 0.49 |

Table 5.1: Table of p-value comparisons for manually annotated time periods.

## 5.4 Predicting embryo sex from human embryo videos using deep learning

Data preprocessing (Fig.5.4a) including cropping and time tag extraction, was first applied before sending the data to the deep neural network. Each video underwent frame cropping and extraction. The frames were first cropped to remove the empty top border and then resized to 224x224 RGB images to align with the requirements of the deep learning model. All input videos were processed such that they started from the 1h time point, and frames 2h apart were used, with the model ultimately using up to 60 frames as its input. Zero vectors were added for sequences shorter than 60 frames. In our deep learning experiments, one instance corresponded to a human embryo video, including the video frames in chronological order, the corresponding time tags, and the sex of the embryo in the video.

To leverage both morphology and temporal information during embryo development, a hybrid architecture combining a Convolutional Neural Network (CNN) and a Recurrent Neural Network (RNN) was adopted (see Method). The CNN functioned as a feature extractor, transforming a time lapse video from an image sequence to a vector sequence. The EfficientNet-B3 [31] pretrained on the ImageNet dataset [32] was used as the CNN backbone for extracting morphology information from the input frames. It output the feature vectors with dimensions of 1x1536. For fine-tuning the EfficientNet-B3 backbone, an auxiliary classifier was built with the EfficientNet-B3 backbone followed by three fully connected (FC) layers. The auxiliary classifier was trained for embryo development stage classification with 19 separate embryo videos that were not included in the subsequent sex classification experiments. After fine-tuning, the EfficientNet-B3 backbone was fixed during the RNN training process.

The Recurrent Neural Network (RNN) received the sequence of feature vectors

extracted by the CNN backbone and was designed to capture temporal patterns within the sequence. The RNN consisted of two gated recurrent unit (GRU) layers [33]. The output from the RNN was fed to FC layers afterwards to generate the probabilities indicating the likelihood of the input instance belonging to either the male or female class. And the predicted sex of the input instance was determined to be the class with higher probability. Gaussian noise layers were placed between GRU layers and FC layers to mitigate overfitting.

During the prediction step, given a test embryo video, a prediction vector generated by the model was output, which provides the probabilities of an embryo belonging to the male or female class. The class with the larger probability value is used as the prediction (Fig.5.4b).

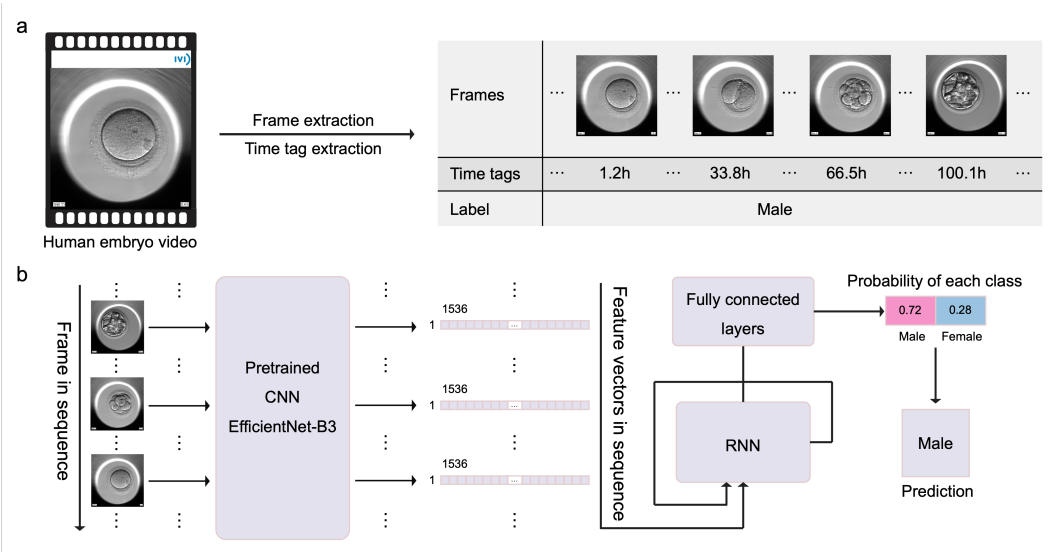


Figure 5.4: Data pre-processing and sex classification process by the deep learning model. a) Embryoscope movies undergo extraction via space and time cropping for input into the deep learning model, as outlined in Method. b) A hybrid architecture combining a Convolutional Neural Network (CNN) and a Recurrent Neural Network (RNN) were adopted for the sex classification task, with further details in Method. An embryo video (an image sequence) was converted to a feature vector sequence by the CNN and then fed to the RNN. Ultimately, using the extracted feature vector sequence, a probability vector is output for each class (male or female): the higher probability class is given as the final prediction (in the example diagram, the male class has the higher probability).

For deep learning, further screening of the evaluated dataset took place to exclude videos with quality issues such as blurriness, blackouts and embryos out of the field

of view (Fig.5.2). This process resulted in 515 human embryo time lapse videos, comprising 290 male embryos and 225 female embryos (Fig.5.5a). With this dataset, we conducted three experiments, each having varied developmental stages and labels as input (Fig.5.5b), which are elaborated later in the text. These experiments were conducted in a three-trial (or three-fold) manner for reliability. Specifically, in each trial, 75 male videos and 75 female videos were randomly selected from the dataset to comprise the testing set, whilst the remaining 215 male videos and 150 female videos comprised the training set. To address the mild imbalance between male class (58%) and female class (42%), we randomly duplicated 65 female videos from the total pool of 150 female videos for each trial (Fig.5.5a). This approach ensured a more balanced representation during model training.

We define accuracy as the number of correct predictions divided by the total number of predictions. Our null hypothesis ($H_0$) is that the focal predictive model has no predictive ability, or that the accuracy is 50%. The corresponding alternative hypothesis ($H_1$) was defined as the focal model having an accuracy higher than 50%. A binominal test was performed to test whether the null hypothesis could be rejected. We set p = 0.05 as our threshold for rejecting $H_0$ and accepting $H_1$.

Our deep learning study consists of three separate experiments. In the first, we used the whole video (from zygote to video end, denoted as Z-End) as the input (Fig.5.5b). Next, to determine whether particular stages could be critical in successful sex prediction, we additionally partitioned the time-lapse videos into two segments based on prior manual annotation (Fig.5.5b Experiment 2 and 3): 1) the period from beginning (1h) to reaching the 8-cell stage (abbreviated as Z-8) (Fig.5.5b) and 2) the period from reaching the 8-cell stage to the end (abbreviated as 8-End). We chose the 8-cell stage as the partition point, because the 8-cell stage is a critical period in development, involving the start of morphogenetic processes such as compaction [1], and important cellular processes such as apical-basal polarisation and the first cell fate decision [34, 35], as well as being clear and easy to spot.

The models trained on whole videos achieved an averaged accuracy of 57%. In two out of the three trials, the model outperformed random predictions ($p < 0.05$). However, as the model failed to reject H0 for one of the trials, we assessed this model as failing to provide statistically significant prediction.

The models that took Z-8 videos as inputs achieved an average accuracy of 47%, with all three p-values close to 1, indicating unsuccessful sex prediction in Z-8 video segments (Fig.5.5c and d). Conversely, the models that took 8-End videos as

inputs reached an average accuracy of 61%, surpassing all other scenarios (Fig.5.5c). Furthermore, all three trials showed p-values smaller than 0.05 (Fig.5.5c), indicating for all three trials, the model outperformed random prediction. These results, which demonstrated that the 8-End model performed better than the Z-8 model, indicate that the developmental difference between male embryos and female embryos likely happens only after the 8-cell stage, which might relate to zygotic genome activation at that stage [36] and therefore the first manifestation of male gene expression.

For our final experiment, we compared the performance between deep neural networks and humans. To match the three-trial experiments for deep learning models, three human subjects were recruited. Similar to the deep neural network experiments, the subjects were first provided with the same videos from the 8-cell stage to the end that were fed to the 8-End models, and then were required to perform sex prediction on embryo videos that they haven't met before. The average accuracy of the three subjects were 46% (Fig.5.5c) and none of them showed statistically better performance over random prediction (Fig.5.5d). The results further implied that the difference between male embryos and female embryos were too subtle for humans to distinguish, while the 8-End models could detect such a difference.

Overall, we found that both manual analysis of the timing parameters and direct human classification were not sensitive enough to find sex differences in embryoscope videos based on developmental timing; however, deep learning models were able to weakly, but significantly, distinguish between sexes using these same videos, with the period from the 8-cell stage onwards appearing to be critical for the identification.

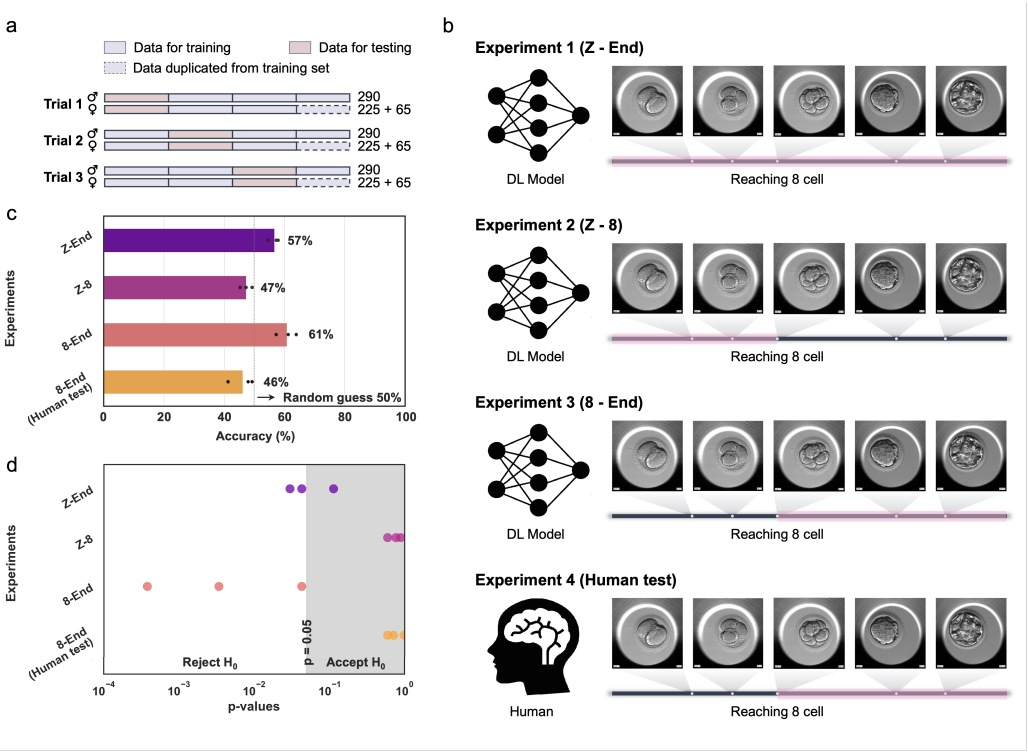


Figure 5.5: Predicting sex from embryoscope videos using deep learning. a) Experimental format shown: three trials were conducted for each experiment, and each trial involved a random set of 75 males and 75 females for testing, with the remaining embryo videos for training. In the training set, 65 female videos were randomly duplicated to ensure equal representation of male and female sets. b) Five experiments were conducted – 1) training the model on whole videos from zygote stage to the end (Z-End); 2) training the model on videos from zygote stage to the 8-cell stage (Z-8); 3) training the model on videos from the 8-cell stage to the end (8-End); 4) recruiting human subjects to distinguish sex differences, provided with videos from the 8-cell stage to the end (Human test); c) Average prediction accuracies on the testing dataset: Using whole videos and videos from the 8-cell stage to the end gave accuracies above 50%, while the remaining experiments produced accuracies of 46% and 47%; d) p-values of the hypothesis tests evaluating whether a certain model outperformed random prediction: only the 8-End models had all three trials surpass random prediction.

## 5.5 Discussion of current accuracy and limitations

In this study, we aimed to answer an important question regarding human embryogenesis: are there sex differences in the pre-implantation period of development [15–17]? Previous attempts to answer this question have used crude and laborious manual analysis, resulting in a lack of consensus as to whether such early sex differences exist [12]. Here, we also find that manual analysis of the timing parameters

is not able to tease apart sex differences in this early stage of development. Instead, deep learning offers a solution: our sex prediction model, specifically when trained from the 8-cell stage onwards, can predict sex with an accuracy that is statistically better than random prediction. However, the reported model has an accuracy of 61%, which does not qualify it as a system that can robustly classify embryo sex based on embryoscope videos.

The accuracy of our sex prediction model could reflect that sex differences are extremely subtle in the pre-implantation stage of human development. Any differences are not visible or detectable by human analysis, but artificial intelligence has been shown to improve on human performance in several areas associated with embryo grading and inspection, especially in relation to morphological parameters [20, 23, 37]. To further investigate these differences, and pinpoint exactly which features are involved in sex differences and prediction, videos with quality and developmental markers beyond what can be achieved by the embryoscope itself would be required. Such videos may help open the 'black box' of our sex prediction model. A thorough understanding of sex differences and a working AI-based detection system can help provide more information on the relationship between embryo failure and sex, as well as the issue of skewed sex ratios. It may also be used as a tool to provide embryologists with early information to address sex-related developmental issues during processing and transfer.

An interesting feature associated with our sex prediction model is that when trained with the whole embryo video, the model performs worse (57%) than when trained with videos from the 8-cell stage to the end (61%). We attributed this discrepancy to the fact that sex differences only occur in the later part of development and including more information (the first part of embryoscope videos) which does not aid sex prediction instead introduces noisy data that prevents important features from being extracted. These issues may also be solved with increased data quality and quantity. This late sex prediction might stem from the fact that the human embryo genome becomes activated only at the 8-cell stage [36] and therefore the presence of Y chromosome only can start to manifest itself at that point. Nevertheless, our sex prediction model provides objective and novel insight into the long-standing question of sex differences in pre-implantation human development.

## 5.6 Appendix

### Human test information

Three volunteers (2 males, 1 female), pursuing postgraduate degrees in STEM fields, but lacking prior exposure to mouse embryo development studies, were recruited from the Caltech community. Prior to participation, all volunteers provided their consent for their involvement and data utilization in the final analysis. Volunteers received detailed instructions in person and accessed the training and testing data on a designated lab computer. They were instructed to first familiarize themselves with the training data, then apply their acquired knowledge to predict the sex of the testing embryo videos and record their predicted labels in an Excel sheet. Following completion, the volunteers' Excel sheets were collected to compute their accuracies and the corresponding p-values on the hypothesis test determining whether a certain volunteer outperformed random prediction.

## References


[1] Kathy K. Niakan et al. “Human pre-implantation embryo development.” In: *Development* 139.5 (2012), pp. 829–841.

[2] Arthur P. Arnold. “A general theory of sexual differentiation.” In: *Journal of Neuroscience Research* 95.1-2 (2017), pp. 291–300.

[3] Patricia Y. Fechner. “The role of SRY in mammalian sex determination.” In: *Pediatrics International* 38.4 (1996), pp. 380–389.

[4] Mari-Lourdes Bernardi et al. “Transcription of Y-and X-linked genes in preimplantation ovine embryos.” In: *Molecular Reproduction and Development: Incorporating Gamete Research* 45.2 (1996), pp. 132–138.

[5] Paul S. Burgoyne. “A Y-chromosomal effect on blastocyst cell number in mice.” In: *Development* 117.1 (1993), pp. 341–345.

[6] Jaana Peippo and Peter Bredbacka. “Sex-related growth rate differences in mouse preimplantation embryos in vivo and in vitro.” In: *Molecular Reproduction and Development* 40.1 (1995), pp. 56–61.

[7] Bo Huang et al. “Is differences in embryo morphokinetic development significantly associated with human embryo sex?” In: *Biology of Reproduction* 100.3 (2019), pp. 618–623.

[8] Munevver Serdarogullari et al. “Comparison of gender-specific human embryo development characteristics by time-lapse technology.” In: *Reproductive BioMedicine Online* 29.2 (2014), pp. 193–199.

[9] Juan J. Fraire-Zamora et al. “P–137 Male embryos take longer to develop to the blastocysts stage.” In: *Human Reproduction* 36.Supplement_1 (2021), deab130–136.

[10] Samer Alfarawati et al. “The relationship between blastocyst morphology, chromosomal abnormality, and embryo gender.” In: *Fertility and sterility* 95.2 (2011), pp. 520–524.

[11] P.F. Ray et al. “Increased number of cells and metabolic activity in male human preimplantation embryos following in vitro fertilization.” In: *Reproduction* 104.1 (1995), pp. 165–171.

[12] Juan J. Fraire-Zamora et al. “No difference in morphokinetics between male and female preimplantation embryos from ART.” In: *Reproductive BioMedicine Online* 46.6 (2023), pp. 911–916.

[13] Norbert Gleicher, Vitaly A. Kushnir, and David H. Barad. “Worldwide decline of IVF birth rates and its probable causes.” In: *Human Reproduction Open* 2019.3 (2019), hoz017.

[14] Tereza Cristina Pinheiro Diogenes et al. “Gender differences in the prevalence of congenital heart disease in Down’s syndrome: a brief meta-analysis.” In: *BMC medical genetics* 18 (2017), pp. 1–5.

[15] John M. Csokmay et al. “Live birth sex ratios are not influenced by blastocyst-stage embryo transfer.” In: *Fertility and sterility* 92.3 (2009), pp. 913–917.

[16] Juan J. Tarin, Miguel A. García-Pérez, and Antonio Cano. “Assisted reproductive technology results: Why are live-birth percentages so low?” In: *Molecular Reproduction and Development* 81.7 (2014), pp. 568–583.

[17] Juan J. Tarín et al. “Changes in sex ratio from fertilization to birth in assisted-reproductive-treatment cycles.” In: *Reproductive Biology and Endocrinology* 12 (2014), pp. 1–8.

[18] Jørgen Berntsen et al. “Robust and generalizable embryo selection based on artificial intelligence and time-lapse image sequences.” In: *Plos One* 17.2 (2022), e0262661.

[19] Charles L. Bormann et al. “Performance of a deep learning based neural network in the selection of human blastocysts for implantation.” In: *Elife* 9 (2020), e55301.

[20] Danilo Cimadomo et al. “Towards automation in IVF: Pre-clinical validation of a deep learning-based embryo grading system during PGT-A cycles.” In: *Journal of Clinical Medicine* 12.5 (2023), p. 1806.

[21] Cheng Shen et al. “Stain-free detection of embryo polarization using deep learning.” In: *Scientific Reports* 12.1 (2022), p. 2404.

[22] Dimitry Tran et al. “Deep learning as a predictive tool for fetal heart pregnancy following time-lapse incubation and blastocyst transfer.” In: *Human Reproduction* 34.6 (2019), pp. 1011–1018.

[23] Nikica Zaninovic and Zev Rosenwaks. “Artificial intelligence in human in vitro fertilization and embryology.” In: *Fertility and Sterility* 114.5 (2020), pp. 914–920.

[24] Lisette Lockhart et al. “Multi-label classification for automatic human blastocyst grading with severely imbalanced data.” In: *2019 IEEE 21st International Workshop on Multimedia Signal Processing (MMSP)*. 2019, pp. 1–6. DOI: 10.1109/MMSP.2019.8901697.

[25] Tianyu Liu, Wenhui Fan, and Cheng Wu. “A hybrid machine learning approach to cerebral stroke prediction based on imbalanced medical dataset.” In: *Artificial Intelligence in Medicine* 101 (2019), p. 101723.

[26] Talha Mahboob Alam et al. “A machine learning approach for identification of malignant mesothelioma etiological factors in an imbalanced dataset.” In: *The Computer Journal* 65.7 (2022), pp. 1740–1751.

[27] Haowen Zhou et al. “AI-guided histopathology predicts brain metastasis in lung cancer patients.” In: *The Journal of Pathology* 263.1 (2024), pp. 89–98.

[28] M. Mostafizur Rahman and Darryl N. Davis. "Addressing the class imbalance problem in medical datasets." In: *International Journal of Machine Learning and Computing* 3.2 (2013), p. 224.

[29] Evgeny Burnaev, Pavel Erofeev, and Artem Papanov. "Influence of resampling on accuracy of imbalanced classification." In: *Eighth International Conference on Machine Vision (ICMV 2015)*. Vol. 9875. SPIE. 2015, pp. 423–427.

[30] Matloob Khushi et al. "A comparative performance analysis of data resampling methods on imbalance medical data." In: *IEEE Access* 9 (2021), pp. 109960–109975.

[31] Mingxing Tan. "Efficientnet: Rethinking model scaling for convolutional neural networks." In: *arXiv preprint arXiv:1905.11946* (2019).

[32] Jia Deng et al. "Imagenet: A large-scale hierarchical image database." In: *2009 IEEE Conference on Computer Vision and Pattern Recognition*. IEEE. 2009, pp. 248–255.

[33] Kyunghyun Cho. "Learning phrase representations using RNN encoder-decoder for statistical machine translation." In: *arXiv preprint arXiv:1406.1078* (2014).

[34] Claudia Gerri et al. "Initiation of a conserved trophectoderm program in human, cow and mouse embryos." In: *Nature* 587.7834 (2020), pp. 443–447.

[35] Meng Zhu et al. "Human embryo polarization requires PLC signaling to mediate trophectoderm specification." In: *Elife* 10 (2021), e65068.

[36] Peter Braude, Virginia Bolton, and Stephen Moore. "Human gene expression first occurs between the four-and eight-cell stages of preimplantation development." In: *Nature* 332.6163 (1988), pp. 459–461.

[37] Brian D. Leahy et al. "Automated measurements of key morphological features of human embryos for IVF." In: *Medical Image Computing and Computer Assisted Intervention–MICCAI 2020: 23rd International Conference, Lima, Peru, October 4–8, 2020, Proceedings, Part V 23*. Springer. 2020, pp. 25–35.

# INDEX